

Copyright
by
Jai Ganesh Kameswaran
2011

The Dissertation Committee for Jai Ganesh Kameswaran
certifies that this is the approved version of the following dissertation:

**Effect of Downscaling Copper Interconnects on the
Microstructure Revealed by High Resolution TEM
Orientation Mapping**

Committee:

Paulo J. Ferreira, Supervisor

Paul S. Ho

Llewellyn K. Rabenberg

Srikanth Krishnan

Seung-Hyun Rhee

Martin Gall

**Effect of Downscaling Copper Interconnects on the
Microstructure Revealed by High Resolution TEM
Orientation Mapping**

by

Jai Ganesh Kameswaran, B.Tech., M.S.E.

DISSERTATION

Presented to the Faculty of the Graduate School of
The University of Texas at Austin
in Partial Fulfillment
of the Requirements
for the Degree of

DOCTOR OF PHILOSOPHY

THE UNIVERSITY OF TEXAS AT AUSTIN

December 2011

Dedicated to my Parents, Friends and Krishna.

Acknowledgments

I would like to thank my advisor Professor Paulo Ferreira for his guidance and constant encouragement throughout this work. I express my gratitude to him for all the trust he placed in my abilities, and for giving me so many opportunities to grow as a researcher. Special thanks to him for being so approachable. Working with him has truly been a tremendous learning experience.

I also thank all my committee members for their time and effort in providing me valuable guidance and suggestions throughout my PhD. I am greatly indebted to Prof. Lew Rabenberg for teaching two of the best graduate level courses that I have taken. They have been instrumental in shaping my understanding of the subject. I would also like to thank him for patiently answering my numerous questions pertaining to course-work and research. I express my deepest gratitude to Prof. Paul Ho, for guiding me on the right research track with his wealth of experience and knowledge in the area of microelectronics, and also for being such a good teacher. The long hours of discussion with him have been invaluable. I am also very thankful to Dr. Srikanth Krishnan, Dr. Seung-Hyun Rhee and Dr. Martin Gall for patiently answering my numerous queries in person and over the phone despite their busy schedules. Their profound knowledge and wealth of experience in the industry has been immensely helpful in my research. I also thank Prof. Rod Ruoff for

giving me the opportunity to collaborate with his research group and use the D-STEM technique to characterize various nanostructures. I would like to thank the Semiconductor Research Corporation for the generous financial support of this research and also for providing numerous opportunities to interact with industry representatives.

I express my deepest gratitude to NanoMEGAS and AppFive for the enormous amount of help and guidance with the precession system. Special thanks to Mr. Daniel Bultreys and Dr. Edgar Rauch to training me from the basics on the system and for patiently answering all my questions. I am also very thankful to Dr. J. K. Weiss and Mr. Bruno Janssens from AppFive, and Dr. Stavros Nicolopolous from NanoMEGAS for all their invaluable guidance, both on technical and career related issues. I thank Prof. Gregory Rohrer from Carnegie Mellon University (CMU) and Prof. Katayun Barmak from Columbia University (earlier at CMU) for very valuable discussions regarding grain boundaries. A big thank you to Dr. Amith Darbal from AppFive (earlier at CMU) for helping with the quantitative analysis of texture and grain boundaries.

I sincerely thank Dr. J. P. Zhou from UT Austin for teaching me how to use the TEM and for all the long hours of discussion regarding electron microscopy. I am extremely thankful to Dr. Shreyas Rajasekhara from Sandia National Labs (earlier at UT Austin) for help with FEM analysis and for invaluable discussions pertaining to microstructure evolution. I would like to thank Ms. Maria Hall from SVTC for the huge help with TEM sample preparation and Dr. Karalee Jarvis from UT Austin from valuable discussions

on electron microscopy. I also thank Linjun Cao from UT Austin for very valuable discussions pertaining to electromigration and stress induced voiding.

This dissertation would not have been completed without the support of my friends and family. A very special thank you to my friends Apurva and Aruna for being with me at every little step. Your support has been crucial in getting me through the difficult phases. At the same time, the happy moments with you have given me four of the finest years of my life. A big thank you also to Abhinav and Shravan for helping me all the way through my PhD. I cannot thank you enough mom and dad, for your love, patience, unflinching faith and unwavering support. I dedicate this work to you all.

Effect of Downscaling Copper Interconnects on the Microstructure Revealed by High Resolution TEM Orientation Mapping

Publication No. _____

Jai Ganesh Kameswaran, Ph.D.
The University of Texas at Austin, 2011

Supervisor: Paulo J. Ferreira

The scaling required to accommodate faster chip performance in microelectronic devices has necessitated a reduction in the dimensions of copper interconnects at the back end of the line. The constant downscaling of copper interconnects has resulted in changes to the microstructure, and these variations are known to impact electrical resistivity and reliability issues in interconnects. In this work, a novel electron diffraction technique called Diffraction Scanning Transmission Electron Microscopy (D-STEM) has been developed and coupled with precession electron microscopy to obtain quantitative local texture information in damascene copper lines (1.8 μm to 70 nm in width) with a spatial resolution of less than 5 nm. Misorientation and trace analysis has been performed to investigate the grain boundary distribution in these lines.

The results reveal strong variations in texture and grain boundary distribution of the copper lines upon downscaling. 1.8 μm wide lines exhibit strong $\langle 111 \rangle$ normal texture and comprise large bamboo-type grains. Upon downscaling to 180 nm, a $\{111\} \langle 110 \rangle$ biaxial texture has been observed. In contrast, narrower lines of widths 120 nm and 70 nm reveal sidewall growth of $\{111\}$ grains and a dominant $\langle 110 \rangle$ normal texture. The fraction of coherent twin boundaries also reduces with decreasing line width. The microstructure changes from bamboo-type in wider lines to one comprising clusters of small grains separated by high angle boundaries in the vicinity of large grains. The evolution of such a microstructure has been discussed in terms of overall energy minimization and dimensional constraints. Finite element analysis has been performed to correlate misorientations between grains and local thermal stresses associated with stress migration. Effect of variations in the copper interconnect microstructure on electromigration flux divergence has also been discussed.

Table of Contents

Acknowledgments	v
Abstract	viii
List of Tables	xiii
List of Figures	xiv
Chapter 1. Introduction	1
1.1 Motivation: The Broad Perspective	1
1.2 The Approach	7
1.3 Dissertation Objectives and Main Contributions	8
1.3.1 Objectives	8
1.3.2 Main Contributions	9
1.3.3 Organization of the Dissertation	11
Chapter 2. Review of Microstructure Studies for Copper Interconnects	13
2.1 Hierarchical Scaling	13
2.2 Damascene Process	14
2.3 Interconnect Reliability	20
2.3.1 Electromigration	20
2.3.1.1 <i>Effect of Microstructure on EM</i>	21
2.3.2 Stress Induced Voiding	26
2.3.2.1 <i>Stress State in Films and Lines</i>	27
2.3.2.2 <i>Factors Affecting SIV</i>	29
2.4 Texture and Grain Boundaries	36
2.4.1 Grain Orientations and Texture	36
2.4.2 Grain Boundaries	40

2.4.2.1	<i>Grain Boundary Misorientation</i>	43
2.4.2.2	<i>Grain Boundary Plane and Types</i>	46
2.5	Techniques to Determine Local Orientation and Grain Boundary Texture	50
2.5.1	X-ray Diffraction	50
2.5.2	Electron Backscatter Diffraction	51
2.5.3	Electron Diffraction in TEM/STEM	56
2.5.3.1	<i>Selected Area Diffraction</i>	56
2.5.3.2	<i>Nanobeam Diffraction</i>	60
2.5.3.3	<i>Convergent Beam Diffraction</i>	62
2.5.3.4	<i>Other nano-area diffraction techniques</i>	63
2.5.4	Microstructure Changes in Downscaling Cu Interconnects	64
Chapter 3.	Experimental Procedure	74
3.1	Materials	74
3.2	Methods	81
3.2.1	D-STEM	81
3.2.2	Precession Electron Diffraction	86
3.2.3	D-STEM with ASTAR: The Instrumentation	91
3.2.3.1	<i>Alignment Procedure for Precession Using Digistar</i>	93
3.2.3.2	<i>Automated Indexing Using ACOMTM</i>	98
3.2.4	π - Inversion Calibration of a Consistent Frame of Reference	103
3.2.5	Relation between TSL TM and ASTAR TM Frames of Reference	110
3.2.6	Finite Element Analysis for Local Stresses in Cu Interconnects using OOF2	112
Chapter 4.	Results and Discussions	118
4.1	Orientation Determination by D-STEM	118
4.2	Automated Orientation Determination in Cu Interconnects using D-STEM and STEM Diffraction Imaging	121
4.3	High Resolution Orientation Mapping in Copper Interconnects (1.8 μm - 70 nm in width) using D-STEM and Precession Electron Diffraction	124

4.3.1	Texture and Grain Boundary Analysis: $1.8\mu m$ wide Cu lines	127
4.3.2	Texture and Grain Boundary Analysis: 180 nm wide Cu lines	132
4.3.3	Texture and Grain Boundary Analysis: 120 nm wide Cu lines	136
4.3.4	Texture and Grain Boundary Analysis: 70 nm wide Cu lines	140
4.4	Effect of Downscaling on the Microstructure of Cu Interconnects	145
4.5	Factors Affecting Microstructure Evolution in Cu Interconnects	147
4.5.1	Overall Energy Minimization during Grain Growth . . .	147
4.5.2	Sidewall Interfacial Energy and Surface Energy Contributions	148
4.5.3	Effect of the Overburden Layer	149
4.5.4	Topological Effects	151
4.5.5	Effect of Stresses	151
4.6	Impact of Observed Microstructure on Electromigration and Stress Induced Voiding	153
4.6.1	Electromigration	153
4.6.2	Stress Induced Voiding	159
4.7	High Resolution Orientation and Phase Mapping	164
4.8	Ambiguities in TEM Orientation Mapping	171
Chapter 5. Conclusions and Future Work		179
5.1	Conclusions	179
5.2	Future Work	183
Bibliography		185
Vita		208

List of Tables

3.1	Dimensional specifications of the Cu interconnect specimens with varying line widths	76
3.2	Stiffness coefficients for Cu [112]	115
3.3	Mechanical properties of the dielectric [112]	115

List of Figures

1.1	Moore's law in terms of relative manufacturing cost/component and number of components per IC [5]	3
1.2	Downscaling of local Cu interconnects	6
2.1	Gate and interconnect delay with feature size [4]	15
2.2	Hierarchical multilayer structure in cross section [8]	15
2.3	Schematic diagram of (a) conventional RIE process (b) damascene process [43]	19
2.4	EM induced interconnect failure by (a) voiding leading to open circuit (b) extrusion leading to short circuit [4]	22
2.5	Required maximum current density scaling at the intermediate level in operating conditions [8]	22
2.6	Stress state in blanket films, unpassivated and passivated Cu lines on Si substrate [6]	28
2.7	(a) Void formation under a via placed over a wide metal lead (b) Finite element analysis of dual damascene via placed over a wide metal lead showing hydrostatic stress contours. The white circles represent vacancies and the arrows depict their motion under the influence of local stress gradients [22].	32
2.8	Elastic modulus of Cu plotted along different crystal directions [6]	35
2.9	Euler angle parametrization of rotation on the three dimensional Euclidian space.	39
2.10	Five parameter description of a grain boundary. The boundary surface is discretized into a set of triangles with each triangle described by a set of five parameters [86].	42
2.11	Misorientation between crystals A and B is the net rotation that transforms the orientation of crystal A to the orientation of crystal B	45
2.12	Axis-angle representation of the misorientation between crystals A and B . A rotation by θ about the axis \mathbf{r} transforms the orientation A to orientation B . \mathbf{r} is the common axis in the two orientations.	45

2.13	Spherical polar coordinates of the grain boundary plane normal \mathbf{n} with respect to the frame of reference of the crystal containing the boundary.	47
2.14	Coherent $\Sigma 3$ boundary. Reproduced from Lu et al. [88].	47
2.15	(a) Schematic of the diffraction plane with respect to the reflecting plane, specimen and the phosphor screen (b) Kikuchi pattern taken from monocrystalline Si at 20 kV beam energy	55
2.16	Interaction and excitation volumes in EBSD	55
2.17	SAD and imaging mode in a TEM [Williams, 2008]	58
2.18	Bright field TEM image of Ag nanoparticles. The circle depicts the approximate area selected by the intermediate aperture	59
2.19	Typical selected area diffraction pattern obtained from a cluster of nanostructures	59
2.20	Electron ray path in CBD and NBD	61
2.21	Orientation mapping of 0.18mm width Cu interconnect line along normal direction, rolling direction and transverse direction. (a) Mapping of whole interested area without coating shows significant drift effects, (b) Selected area mapping with gold and carbon dual layer coating shows significant reduction in specimen drift during acquisition of EBSD patterns[24]	67
2.22	Stereogram showing the crystallographic texture for an annealed, blanket Cu film. The (111) pole plot shows that the Cu has a strong (111) fiber texture and (511) twins [26].	70
2.23	Stereogram showing the crystallographic texture results as a function of linewidth for inlaid Cu lines. The (111) pole plots for 0.35, 0.5, 0.7 and 1.06 mm show the lines are (111) oriented. The fraction of sidewall-nucleated (111) grains increases with decreasing linewidth [26].	71
2.24	(a) Stereogram showing (110) and (100) pole plots for 0.35 μm lines. with no (110) or (100) oriented grains (b) Schematic drawings illustrating the development of (111) texture in lines and the influence of these texture components on the pole plot. For lines with vertical sidewalls, (111) grains grow from the trench bottom and sidewall. Sidewall growing grains show a preferred [110] in-plane orientation [26].	72
3.1	Schematic of Cu interconnect sample in cross section	76
3.2	Schematic illustration of the dual beam FIB [An, 2007]	79
3.3	Schematic representation of ray path in D-STEM [Ganesh, 2010a]	83

3.4	Diffraction pattern showing a systematic row of reflections . .	85
3.5	Block diagram of the set up for precession electron diffraction. Reproduced from Vincent and Midgley [104].	87
3.6	Ray diagram for precession diffraction, a double-conical beam rocking system. G is the radius of the conical diffraction and C is the precession angle [98].	88
3.7	Diffraction patterns from Cu samples with (a) no precession and (b) with a precession angle of 0.4° . Note the presence of faint Kikuchi lines when the diffraction pattern is collected without precession, which vanish with the use of precession.	90
3.8	Schematic of hardware setup for the ACOM TM system. (Courtesy: E. F. Rauch).	92
3.9	(a) Screen-shots from Digistar control for (a) Beam pivot point alignment (b) Descan alignment	95
3.10	Examples from compensation alignment showing (a) lacing effect of the beam (b) elongation along Y direction (c) compensation adjustment along X direction (d) resulting pseudo-line along the Y direction (e) well aligned beam.	97
3.11	(a) Variation of the maximum correlation index with camera length. (b) Overlay of the best matching template with the observed diffraction pattern.	101
3.12	(a) Distortion correction. (b) Diffraction pattern with distortion. (c) Diffraction pattern corrected for distortion.	102
3.13	(a) Bright field image of an α -MoO ₃ crystal and (b) diffraction pattern from the same crystal.	105
3.14	(a) Bright field image of an α -MoO ₃ crystal and (b) defocused diffraction pattern from the same crystal shows that there is a 180° inversion between the bright field image and the diffraction pattern.	106
3.15	(a) Diffraction pattern collected from an an α -MoO ₃ crystal from the CCD camera and (b) the same diffraction pattern collected using the optical camera.	107
3.16	The coordinate system for the orientation maps with respect to the scanning direction. OC is the orientation of the reference direction in the diffraction pattern.	109
3.17	Comparison of the reference system used in ASTAR TM and TSL TM OIM data analysis.	111
3.18	(a) Color coded FEM model containing orientation parameters for each Cu grain (b) 2D mesh solved to obtain the stress solution	114

4.1	(a) Bright-field STEM image of Ag nanoparticles (b) diffraction pattern from P1 (~ 4 nm in size) along the $[112]$ beam direction; (c) bright-field STEM image of boron nitride nanoparticles (d) diffraction pattern from P2 (~ 3 nm in size) along the $[001]$ beam direction.	120
4.2	(a) Bright field STEM image of 120 nm wide Cu interconnect lines showing grain labeled 1-10. (b) Representative diffraction patterns obtained from grains labeled 1, 3, 4 and 6 $[113]$. . .	123
4.3	Bright field TEM images of periodic Cu lines (a) 180 nm wide (b) 120 nm wide	126
4.4	Color coded inverse pole figure map from 1.8 μm wide Cu lines. Color codes for orientations are represented in the standard stereographic triangle.	128
4.5	Schematic illustrating ND, RD and TD directions with respect to the Cu trench	129
4.6	Inverse pole plots along the Cu trench normal (ND), length (RD) and width (TD)	130
4.7	Color coded inverse pole figure map from 180 nm wide Cu lines. Color codes for orientations are represented by the standard stereographic triangle	134
4.8	Inverse pole plots along the Cu trench normal (ND), length (RD) and width (TD)	135
4.9	Color coded inverse pole figure map from 120 nm wide Cu lines. Color codes for orientations are represented by the standard stereographic triangle	138
4.10	Inverse pole plots along the Cu trench normal (ND), length (RD) and width (TD)	139
4.11	Color coded inverse pole figure map from 120 nm wide Cu lines. Color codes for orientations are represented by the standard stereographic triangle	142
4.12	Inverse pole plots along the Cu trench normal (ND), length (RD) and width (TD)	143
4.13	Orientation map in cross section showing clusters of small grains at the trench bottom (highlighted by the red ellipse)	144
4.14	Variation of the percentage of $\Sigma 3$ boundaries with Cu interconnect line width	146
4.15	(a) Bright field TEM image of the EM test line (b) Color coded inverse pole figure map (orientations along trench normal) of voided region with reconstructed boundaries. Points A, B, C have been assumed to be potential flux divergence sites before the void formation.	156

4.16	Color coded orientation map of the via (V2) connecting M2 and M3. The colors represent grain orientations along the trench normal. Grain boundaries in red are coherent $\Sigma 3$ boundaries while those in yellow are $\Sigma 9$ boundaries.	158
4.17	(a) Orientation map (b) FEM model with color coded grains (c) 2D mesh (d) Hydrostatic stress contours	162
4.18	Local misorientations in regions of high hydrostatic stresses . .	163
4.19	Virtual dark field image obtained during precession	165
4.20	Color coded orientation from Pt nanoparticles	166
4.21	Bright field TEM image of PLD Ni film	169
4.22	(a) Reliability map obtained after precession analysis (b) Colored phase map overlaid with the reliability map.	170
4.23	(a) Simulated $[112]$ diffraction pattern from Cu and (b) experimental pattern from Cu close to $[112]$ zone axis [136].	173
4.24	Reliability index for Cu as a function of the beam direction in the crystal frame of reference. Dark regions show regions of low reliability [136].	174
4.25	177
4.26	(a-b) Diffraction pattern from neighboring points (c) Indexing solution	178

Chapter 1

Introduction

1.1 Motivation: The Broad Perspective

The era of *Information Revolution* over the last few decades has been marked by tremendous technological advancements in the field of microelectronics. Since the invention of the first transistor in 1947 at the Bell Labs, and the introduction of the first integrated circuit in the 1960s, the microelectronics (semiconductor) industry has revolutionized nearly every facet of human life. More so, today's digital world continues to witness path-breaking inventions in this dynamic industry to keep pace with the insatiable demand for faster and more complex computing. The ubiquitous nature of modern semiconductor devices powering novel automation solutions in businesses ranging from automotive manufacturing and power plants to consumer banking significantly enhances their productivity and performance efficiency, thereby leading to sustainable innovation in diverse areas. Apart from its role as a technology bellwether, the semiconductor industry is also widely recognized as a key driver for global economic growth with an overall worldwide base market of \$304 bn in 2010 [1]. Its rapid pace of development has principally resulted from the ability to exponentially decrease the minimum feature size of the transistors used to fabricate integrated circuits (ICs) in modern electronic devices. This down-

scaling trend is historically associated with a paper by Gordon Moore in 1965 and is termed as *Moore's Law* [2]. From a technical standpoint, reducing the critical transistor dimensions while keeping the electric field constant results in higher switching speeds and reduced power consumption. It also enables the incorporation of more number of components per chip, thereby reducing fabrication cost-per-chip while concurrently increasing compactness and functionality [3]. Fig. 1.1 depicts Moore's Law in terms of relative manufacturing cost/component and exponential increase in the number of components per Integrated Circuit (IC).

The expected entitlements of periodic improvements according to Moore's Law has, heretofore been achieved through innovative approaches such as novel circuit designs and system architectures, improved processing techniques and the development of new materials with improved physical properties. However, these developments have constantly encountered numerous challenges. For instance, although traditional transistor scaling through reduction in channel length, dielectric thickness and junction depth has improved the gate delay, the increasing parasitic influence of the chip wiring has increased the interconnect delay (RC delay) to become the performance limiting factor [4].

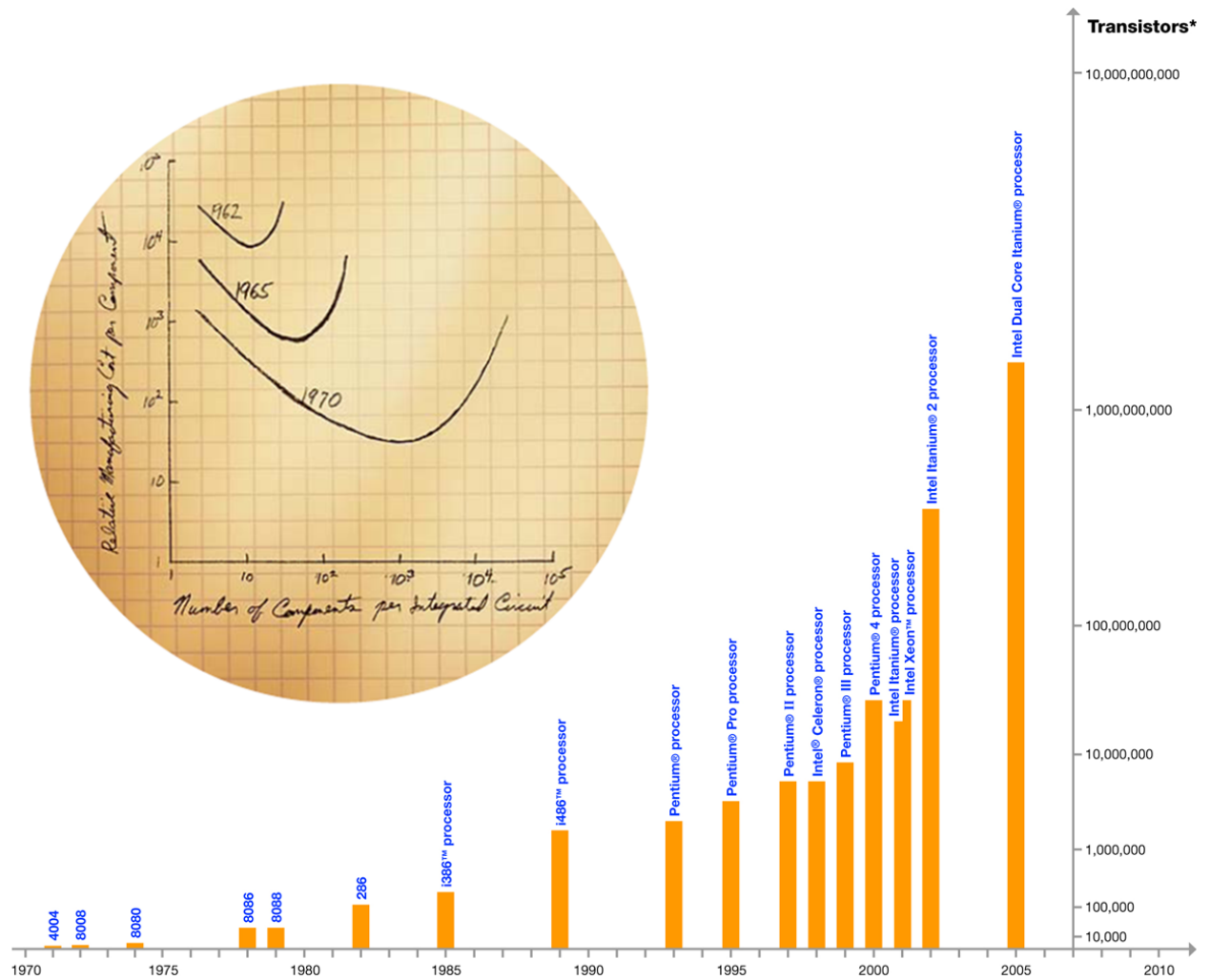


Figure 1.1: Moore's law in terms of relative manufacturing cost/component and number of components per IC [5]

To address the RC delay issue, a *hierarchical* or *reverse scaling* metallization design has been employed and the traditional Aluminum (Al)-Copper (Cu) interconnects have been replaced by Cu, which has lower electrical resistivity. The details of the scaling scheme is discussed in the subsequent chapter. In addition to lower resistivity, Cu metallization has also been chosen because Cu has a smaller coefficient of thermal expansion (CTE) and better thermal stability than Al [6]. It is also more cost effective when compared with other metals with high conductivity like Gold (Au) and Silver (Ag). Another key attribute of Cu metallization is that multiple interconnect levels can be fabricated by electroplating via the damascene process. A detailed explanation of the damascene process for Cu metallization is given in the following chapter. The first industrial implementation of Cu interconnects was reported in the year 1997 [7] and since then, there has been a remarkable reduction in the dimensions of the smallest interconnects in a chip. In fact, according to the 2010 ITRS roadmap update, the interconnect technology in production has a DRAM 1/2 pitch of 45 nm, and is expected to reduce to about 22 nm by the year 2015 [8].

Due to its favorable physical properties, Cu was expected to prevent reliability issues that had affected Al based metallizations. However, those reliability issues still exist in modern interconnects, in particular, electromigration and stress induced voiding. Electromigration occurs due to mass transport induced by momentum transfer to the metal ions by the electrons flowing in the interconnect leading to the formation of voids, hillocks and mass pileups

[9-16]. On the other hand, stress induced voiding occurs as a result of the hydrostatic stresses that build up in Cu interconnects during thermal cycling, due to a difference in the coefficients of thermal expansion between Cu and the underlying Si substrate [17-23]. As the Cu interconnect line width has downscaled with each technology node, from the sub-micron to the nanometer regime, the aforementioned reliability issues have become increasingly complex owing to drastic variations in the Cu microstructure. Therefore, understanding the impact of microstructure changes in Cu interconnects induced by scaling is quintessential to the development of reliable future metallizations. While numerous studies have been conducted to investigate the microstructure of wide Cu lines [24-30], very limited information is available on microstructure evolution in narrower Cu interconnects ($\leq 120\text{nm}$). Efforts in this direction have largely been impeded by limitations in spatial resolution for determining the statistical distribution of orientations from a large ensemble of nanocrystalline grains in an automated fashion. *In this regard, the dissertation focuses on the development of a novel high resolution electron diffraction technique for automated orientation mapping of nanostructures, and its implementation to investigate the effect of downscaling on the texture and grain boundaries in nanoscale Cu interconnects.*

The financial support for this work has been provided by the Semiconductor Research Corporation (SRC) under the Global Research Collaborative (GRC) initiative. The interconnect samples used in this work have been provided by Freescale Semiconductor, Inc. and Texas Instruments, Inc.

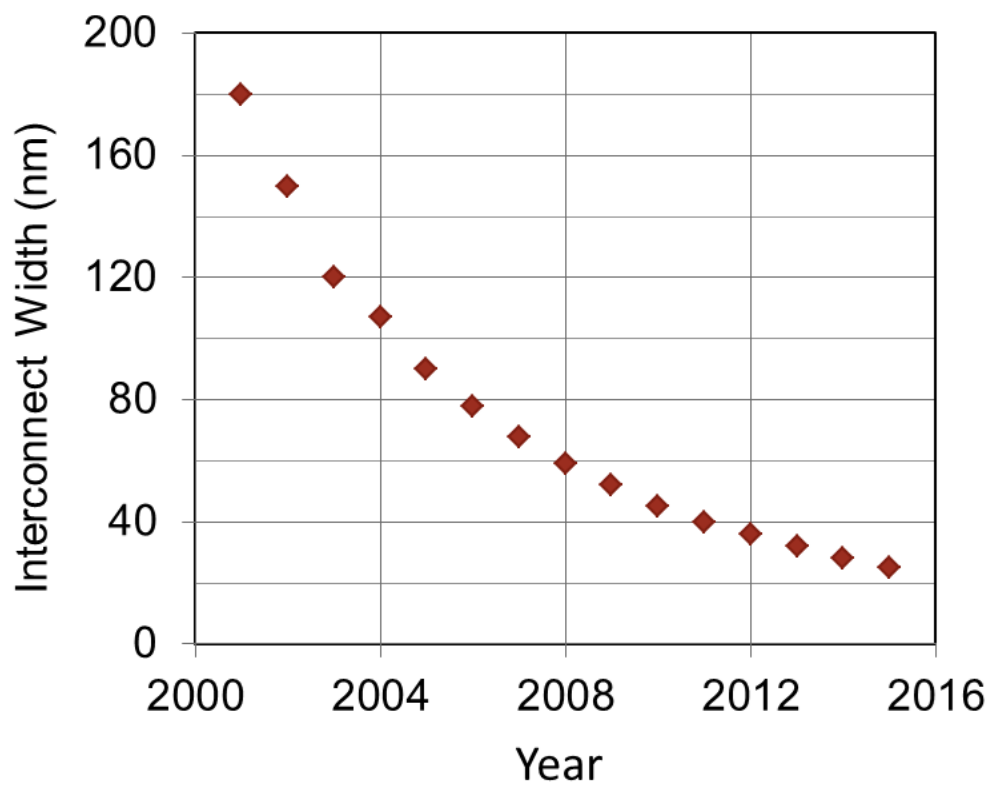


Figure 1.2: Downscaling of local Cu interconnects

1.2 The Approach

To perform orientation analysis with high spatial resolution (<5 nm), a novel electron diffraction technique called Diffraction - Scanning Transmission Electron Microscopy (D-STEM) was developed in a JEOL 2010F transmission electron microscope (TEM) / scanning transmission electron microscope (STEM). The electron optics in the STEM configuration were configured to form a 1-2 nm near parallel illumination on the specimen which could be accurately positioned at the nanoscale feature of interest on the image to obtain sharp spot electron diffraction patterns. In order to enable automated acquisition and indexing of the patterns, the lens configuration of the D-STEM technique was coupled with precession microscopy, using the ASTARTM system from NanoMEGAS. The combination of the two techniques renders about an order of magnitude improvement in spatial resolution over the electron back scattered diffraction technique, conventionally used for automated orientation mapping in a scanning electron microscope (SEM). To investigate the effects of Cu interconnect downscaling on the microstructure, the precessed D-STEM technique was employed to collect statistically significant orientation data for quantitative analysis of local texture in periodic Cu interconnects with line widths varying from $1.8\ \mu m$ - 70 nm. Subsequently, grain boundary misorientation and trace analysis was performed to comprehensively investigate the types of grain boundaries present in the Cu interconnects as a function of line width. Since the Cu interconnects are under hydrostatic stresses which arise during thermal cycling, the influence of misorientations between grains on the

local hydrostatic stresses in these lines has been analyzed by 2D finite element method (FEM) using the OOF2TM package. The grain structure around the voided regions in dual damascene Cu interconnects affected by electromigration were also analyzed and preliminary analysis of the dependence of flux divergence during electromigration on grain orientations has also been performed. Finally, as a further exploration of the capabilities of this technique, its application for phase and orientation analysis on nanomaterials with non-cubic symmetry has also been demonstrated.

1.3 Dissertation Objectives and Main Contributions

1.3.1 Objectives

The specific objectives of the dissertation are:

1. To develop a high resolution electron diffraction technique in a TEM/STEM for automated orientation and phase mapping of nanostructures.
2. To demonstrate the applicability of this technique for phase and orientation analysis of nanomaterials with cubic and non-cubic symmetry.
3. To perform quantitative texture and grain boundary analysis on Cu interconnects ranging from $1.8\ \mu m - 70\ nm$ in width, and investigate microstructure changes in Cu interconnects induced by scaling.
4. To investigate the grain structure, texture and types of grain boundaries around voided regions in 70 nm wide dual damascene Cu interconnects affected by electromigration.

5. To use the crystal orientation data and simulate local hydrostatic stresses in Cu interconnects using 2-D finite element method.

1.3.2 Main Contributions

The main contributions of the dissertation are:

1. Development of a high resolution electron diffraction technique called D-STEM to obtain orientation information from crystals smaller than 5 nm. The technique results in a 1-2 nm near-parallel beam in a STEM configuration that can be scanned to obtain an image. Subsequently, the beam can be placed at any nanoscale feature of interest on the image to obtain easily indexable sharp diffraction patterns. Conventional electron diffraction techniques in a TEM/STEM that can be used to obtain spot diffraction patterns are either limited in terms of spatial resolution or the ability to position the probe easily and accurately at the feature of interest. On the other hand, convergent beam techniques results in complex disc patterns that are very difficult to index for determining crystal orientations.

2. Integration of the D-STEM technique with precession electron microscopy using the ASTARTM system from NanoMEGAS for automated acquisition and indexing of spot electron diffraction patterns. The combination of these two techniques renders high resolution orientation and phase maps from an ensemble of nanostructures, with an order of magnitude improvement in spatial resolution over the electron back scattered diffraction technique in the SEM, conventionally used for automated orientation mapping. The dissertation also

discusses detailed routines for quantitative analysis of parameters describing the overall microstructure.

3. Determining the effects of downscaling on the texture, grain boundaries and grain structure in nanoscale Cu interconnects with line width ranging from $1.8\ \mu m - 70\ nm$. It is well known that variation in the microstructure of Cu interconnects strongly impacts their electrical resistivity [31, 32] and mechanical reliability [33-37]. In this regard, such comprehensive analysis of the interconnect microstructure with statistically significant data is critical to enable microstructure control for improved device designs, materials and processes in future metallization technologies.

4. 2-D microstructural FEM simulation of local thermal stresses in Cu interconnects. In general, Cu interconnects fabricated by the inlaid damascene process are under mechanical stresses arising during thermal cycling due to the difference in thermal expansion coefficients between the metallic interconnect, substrate and dielectric. Previous work through experiments and simulations have confirmed this, and shown that the stresses are strongly influenced by the aspect ratio of the Cu trench [38]. With increasing aspect ratios upon downscaling, the stress state in the Cu lines changes from biaxial to quasi-hydrostatic. However, these studies assumed the lines to be isotropic and thus neglected the elastic anisotropy of Cu. They also did not account for the microstructure of Cu interconnects, comprising numerous grains with different orientations. In order to investigate how the microstructure influences local stress distribution within Cu interconnects, orientation data obtained

using electron diffraction has been used to develop a model and local hydrostatic stresses have been simulated by microstructural FEM using the OOF2TM package.

1.3.3 Organization of the Dissertation

Chapter 2 starts by discussing the hierarchical multilayer interconnect structures found in modern integrated circuits. This is followed by an overview of the damascene process used to deposit the Cu interconnect lines. Next, the reliability issues associated with Cu interconnects are discussed with focus on understanding the impact of microstructure on interconnect reliability. Then, a description of the elements of the microstructure such as texture and grain boundaries is presented. The section also includes a detailed review of the mathematical techniques used to quantify the microstructure. The following section reviews the experimental techniques for microstructure analysis, particularly at the nanoscale. The advantages and limitations of the individual techniques are also discussed. Finally, a review on the research performed to understand microstructure evolution in Cu interconnects is provided. All of the sections in the chapter are supported by numerous references.

Chapter 3 is broadly divided into two sections, namely Materials and Methods. The section on Materials discusses about the samples that were analyzed through the course of the research. The section on Methods describes the experimental procedures required to accomplish the objectives of the dissertation. In particular, the development of a high resolution electron

diffraction technique for orientation mapping in the TEM is explained extensively. The detailed procedure for data acquisition and analysis for extracting relevant information is also described. Finally, model development to simulate local stresses in Cu lines by FEM is outlined.

In Chapter 4, first, the experimental results of the microstructure characterization in Cu interconnects performed using the novel TEM orientation mapping technique are presented. Specifically, quantitative results for grain orientations and grain boundary distributions are presented for Cu lines with four different line widths ranging from 1.8 μm - 70 nm. In addition to this, the grain structure in these lines was also elucidated through high resolution color coded orientation maps. The subsequent sections thoroughly discuss the evolution of microstructure in downscaling Cu lines from the standpoint of surface, interface, grain boundary and strain energy minimization. Later, the implications of the microstructure observed in narrow lines on electromigration and stress induced voiding are discussed. In this regard, results of grain orientation and grain boundary misorientation in the via region, and also close to an electromigration induced void are analyzed. Finally, some diverse applications of the TEM technique in orientation mapping of Pt nanoparticles and phase mapping of Ni structures are also included.

Finally, the general findings of the dissertation are summarized in Chapter 5. The dissertation concludes with a discussion of possible future work.

Chapter 2

Review of Microstructure Studies for Copper Interconnects

2.1 Hierarchical Scaling

In very large scale integrated circuits (VLSIs), 'interconnects' refer to metal lines connecting various electronic devices to carry current or transport charge [39]. The resistance and capacitance of interconnects directly impact the signal delay at the back end of the line (BEOL), commonly referred to as the resistance-capacitance (RC) delay. It is known that with traditional transistor scaling, the RC delay increases and becomes the major bottleneck limiting the overall chip performance (Fig. 2.1). Therefore, to reduce the line resistance, Cu (resistivity $\sim 1.8 \mu\Omega\text{.cm}$) was proposed and first implemented by IBM in 1998 [7] to replace the Al-based interconnects (resistivity $\sim 3.3 \mu\Omega\text{.cm}$).

Typical microprocessor designs utilize a multilevel interconnection layout with hierarchical or reverse scaling metallization scheme. In such a layout, interconnects can either be local, intermediate (semi-global) or global as shown in Fig. 2.2. In general, local interconnects form the first level of the interconnect structure and usually connect gates, sources and drains in metal oxide semiconductor (MOS) technology and emitters, bases and collectors in bipolar

technology. They have the smallest dimensions among the different interconnect levels and scale down in size with the active devices in each technology node. The intermediate interconnects are larger than the local interconnects and are used to connect devices within a block. The global interconnects, commonly referred to as 'fat wires' have the largest dimensions amongst all interconnects and are used as connections between individual blocks for power distribution, grounding and clocking [40]. Although local interconnects have a greatly reduced cross sectional area, the increase in their resistance is minimized due to their short length. Since the intermediate and global interconnects have to travel relatively long distances within the chip, they are designed to have a larger cross-sectional area to lower their resistance [40]. With decreasing conductor spacing, local interconnects also suffer from increased sidewall capacitance and cross-talk. In order to mitigate the parasitic capacitance issues, low permittivity (k) dielectric materials have been introduced to replace the traditional SiO_2 dielectric [4, 41]. In addition to this, a crisscross wiring layout across multiple levels is also employed. Thus, a combination of improved materials as conductors/dielectrics coupled with hierarchical scaling has prevented interconnect latency from overwhelming transistor delays in current microprocessor designs.

2.2 Damascene Process

The introduction of Cu wiring in interconnects has brought significant processing challenges to the BEOL. Due to the unavailability volatile Cu com-

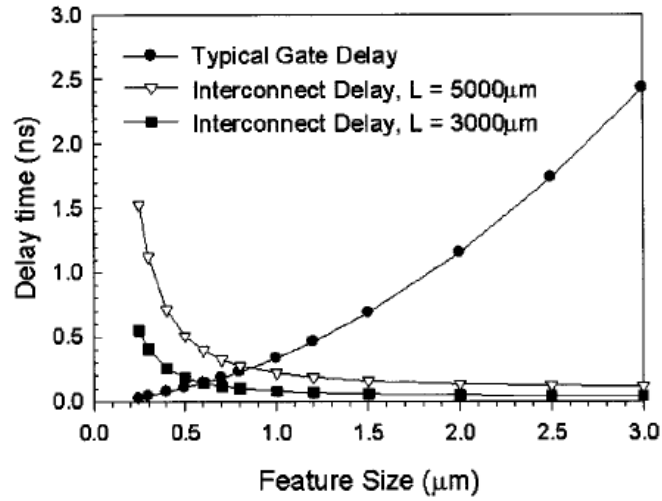


Figure 2.1: Gate and interconnect delay with feature size [4]

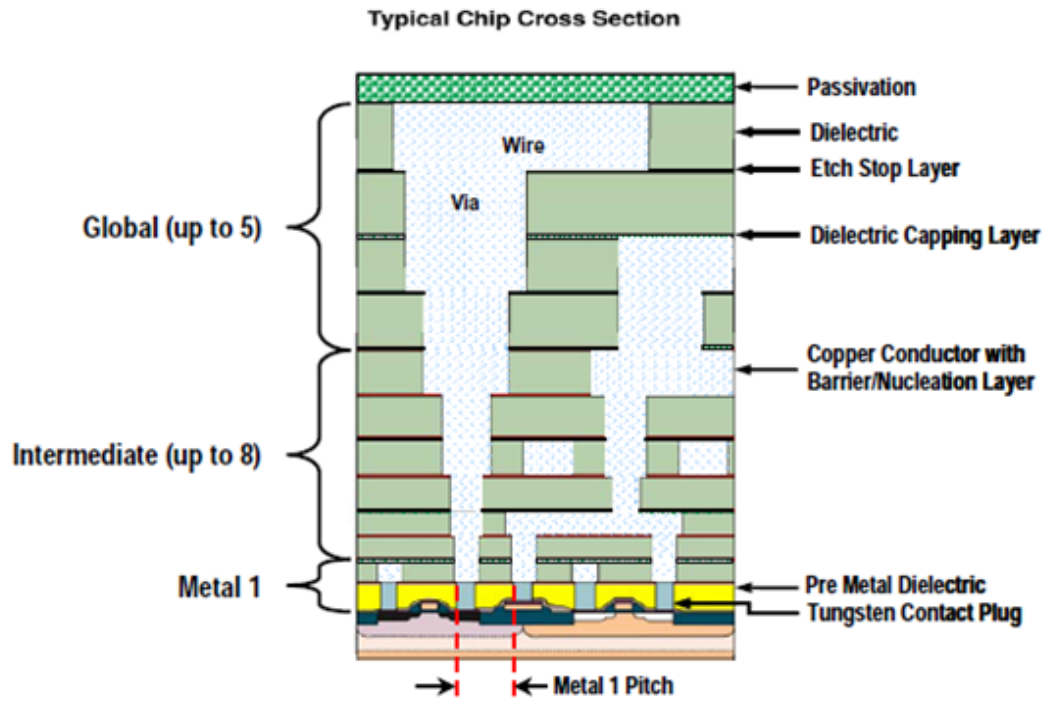


Figure 2.2: Hierarchical multilayer structure in cross section [8]

pounds at low temperatures, Cu cannot be patterned using the conventional reactive ion etching (RIE) process that was used for Al metallization [42]. Wet etching techniques are also unsuitable due to its isotropic nature, thereby making it difficult to yield uniform sub-micron wiring trenches. Unlike Al, which has a native stable oxide layer (Al_2O_3) layer to passivate the surface, Cu oxidizes easily and the unstable oxidation layer lacks the passivation function. Cu also has a high tendency to diffuse into the dielectric layers and eventually, into the underlying silicon substrate, which degrades the device performance.

To overcome the aforementioned challenges, a new process scheme, called the 'damascene' process was introduced. This process is fundamentally different from the subtractive RIE process used for Al interconnects. These two patterning processes in Al- SiO_2 and Cu/low-k system are compared in Fig. 2.3 (a-b) [43]. In the subtractive RIE process, a thin Al film is first deposited then patterned using photolithography and RIE process to form the wiring patterns. This is followed by a dielectric deposition step, forming an insulating layer between and on top of the Al wires. Following this, the chemical mechanical polishing (CMP) process is employed to planarize the top dielectric layer. Subsequently, the complete processing sequence is repeated until the multilayered interconnect structure is fabricated.

In comparison, unlike the RIE process, the damascene process is designed to only enable etching of the dielectric layer and avoid any etching process of the metal while forming the trenches. Initially, a thin layer of dielectric is deposited and patterned to form wiring trenches using photolithography and

the RIE process. This is followed by the Cu metallization process to fill in the trench openings. The Cu metallization process starts with a deposition of a very thin Ta-based diffusion barrier layer in the trench by physical vapor deposition (PVD). The barrier layer is implemented to prevent Cu from diffusing into the dielectric. It also acts as a base layer for the subsequent process. The next step is the deposition of a PVD Cu seed layer followed by a complete Cu fill in the trench by electroplating. The electrodeposited Cu is layered in thick coatings above the trenches. The excess Cu is referred to as the overburden layer. Subsequently, the Cu microstructure in the trench is stabilized by a low-temperature annealing ($150\sim 250\text{ }^{\circ}\text{C}$) treatment. Following this, a CMP process is applied to remove the Cu overburden and the excessive barrier layer on the top surface. Finally, a SiN_x or SiC_xN_y capping layer is deposited at $\sim 400^{\circ}\text{C}$ to passivate the wiring structure for one interconnect level. Additionally, in a multilayer structure, the different metal levels are connected by 'vias', and once a metal line is fabricated, the connecting via is processed in a similar manner. Such a process of fabricating the via and line separately is referred to as the 'single damascene process'. However, in modern IC fabrication, a slight modification of the single damascene process is employed to pattern the via and trench in a single step. This is called the 'dual damascene process'. The different approaches to the dual damascene process include the via first, trench first or buried via. The detailed procedures for these approaches are outlined in references [39, 44]. The advantage of this process is that only one metal filling step is required for both the via and trench structures in each level of the

interconnect. This can reduce the via resistance and improve electromigration reliability in comparison to the single damascene process. The disadvantage of this process is the high aspect ratio of the via and trench structure, making etching, cleaning, and Cu filling processes more difficult. This gives rise to more challenges for material and process integration.

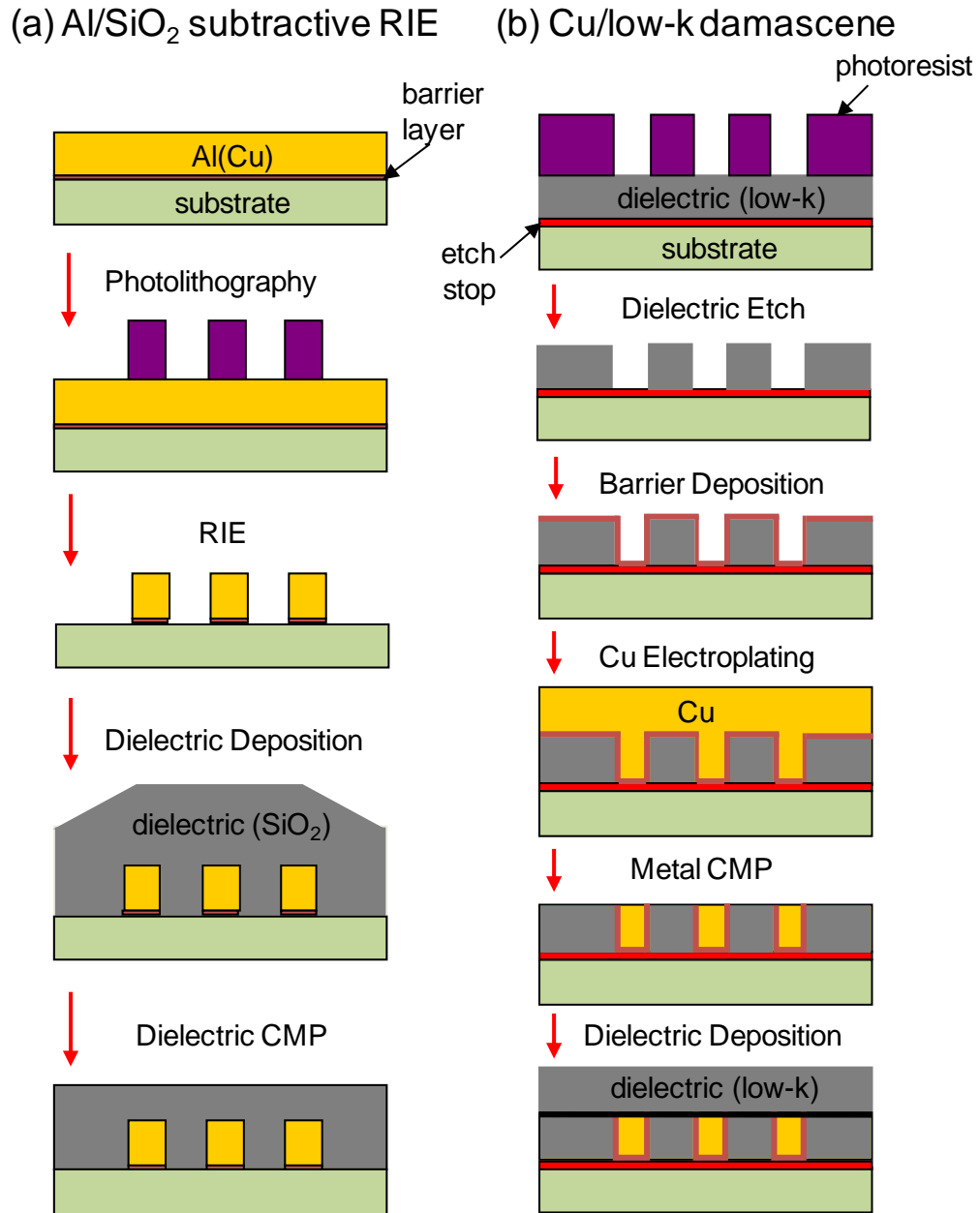


Figure 2.3: Schematic diagram of (a) conventional RIE process (b) damascene process [43]

2.3 Interconnect Reliability

The continuing improvement in device density and performance has augmented the complexity of the wiring structure for on-chip interconnects. Concurrently, the increased current density in interconnect lines, implementation of novel materials at the BEOL with drastically different physical and mechanical properties and complex processing conditions impact reliability issues in interconnects. Two major reliability issues in Cu interconnects are Electromigration and Stress Induced Voiding.

2.3.1 Electromigration

Electromigration (EM) is a diffusion-controlled mass transport phenomenon occurring by momentum transfer to the metal ions due to collisions from the moving electrons [45]. The initial observations of EM were first reported by Geradin in 1861 [Ho 1989]. However, EM was first identified as a serious reliability concern in Al-based ICs in 1967 [47]. Decades later, EM remains a dominant reliability concern for modern ICs due to aggressive scaling of interconnect dimensions and comparably aggressive increase of current densities [8]. The electric field applied across an interconnect during operation biases the net motion of metallic ions in the direction of electron flow (from cathode to anode). This net flux of atoms occurs in response to the applied electric field and is affected by two opposing driving forces: the electron wind force which transfers momentum to the metal ions in the direction of the electron flow, and a back stress that pushes the ions in the opposite direction.

Thus, under EM, a void is created at the cathode end or a hillock is accumulated at the anode end to induce EM failure. Fig 2.4 shows an example of EM induced voiding which can lead to interconnect failure by open circuit. The atomic flux (J) for EM can be expressed as

$$J = -\frac{DC}{kT}(Z^*eE - \Omega\frac{d\sigma}{dx}) \quad (2.1)$$

where D is the diffusivity, C is the concentration of atoms, k is the Boltzmann constant, T is the temperature, Z^* is the effective charge number, e is the fundamental electronic charge, E is the electric field, Ω is the atomic volume and $\frac{d\sigma}{dx}$ is the stress gradient along the line. The electric field can be expressed as

$$E = \rho j \quad (2.2)$$

where ρ is the metal resistivity and j is the current density. Eqs. 2.1 and 2.2 show that the EM atomic flux increases with increasing current density. As shown in Fig. 2.5, the required maximum current density is increasing at the intermediate level in operating conditions with future technology nodes [8]. This makes the EM problem more critical in shrinking interconnect structures.

2.3.1.1 *Effect of Microstructure on EM*

Eq. 2.1 also shows that the mass transport during EM is strongly dependent on the interconnect microstructure. During EM, metal ions have

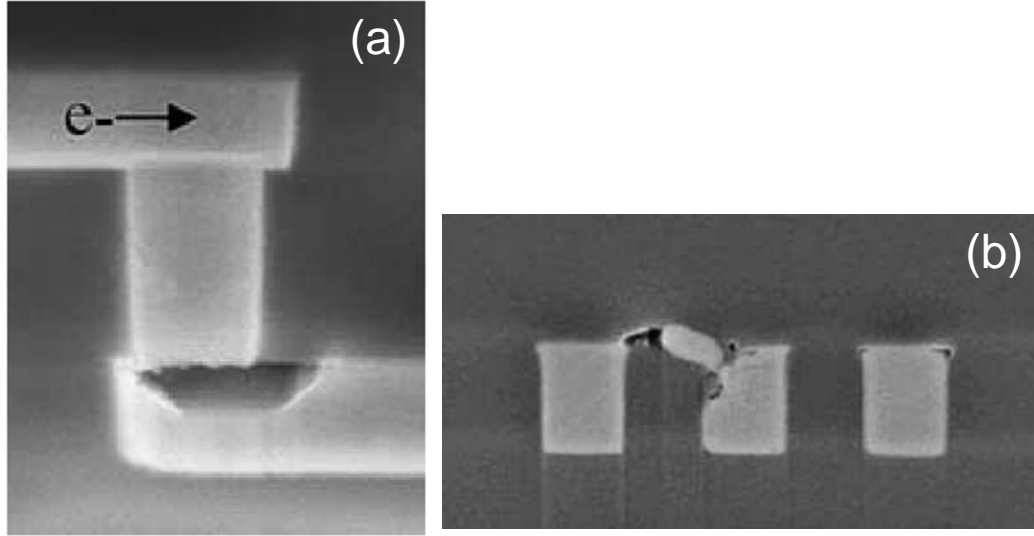


Figure 2.4: EM induced interconnect failure by (a) voiding leading to open circuit (b) extrusion leading to short circuit [4]

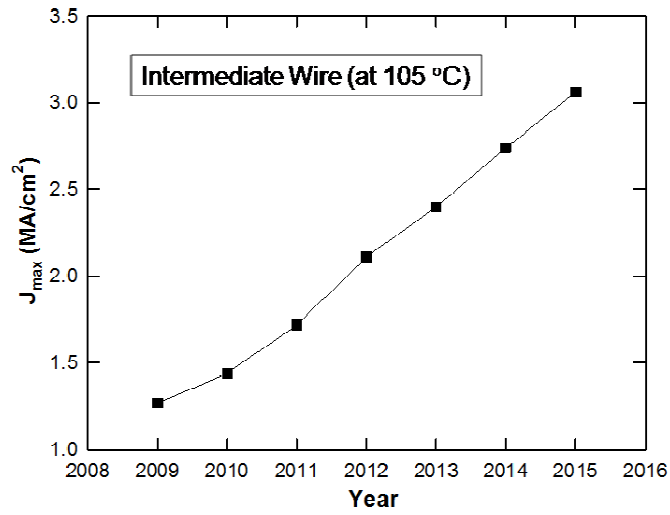


Figure 2.5: Required maximum current density scaling at the intermediate level in operating conditions [8]

various diffusion pathways, including the top interface, grain boundary, barrier interface, bulk, and the dislocation cores. Therefore, the effective diffusivity, D_{eff} , is a combination of contributions from each of the above pathways. D_{eff} can be written as

$$D_{eff} = \frac{\delta_N}{h} D_N + \frac{\delta_{GB}}{d} (1 - \frac{d}{w}) D_{GB} + \delta_{BN} (\frac{2}{w} + \frac{1}{d}) + n_B D_B + \rho_{disl} d^2 D_{disl} \quad (2.3)$$

where the subscripts N , GB , B , BN and $disl$ identify the possible diffusion pathways as the cap interface, grain boundary, bulk, barrier interface and dislocation cores respectively. D is the diffusivity and δ is the effective width for corresponding diffusion path. [48-51] The parameter h is the line thickness, d is the average grain size, w is the line width, ρ_{disl} is the dislocation density, and n_B is the fraction of ions diffusing through the bulk of the line. Due to the small dislocation core density, the mass transport through dislocations can be neglected. Since the diffusivity along a particular pathway has an Arrhenius dependence on the activation energy, the relative contributions from these diffusion paths can be compared based on their activation energies. For Cu interconnects, those activation energies have been measured to be 0.8-1.1 eV for the Cu/SiCN interface [51-53], 0.7-0.95 eV for grain boundaries [54, 55], 1.1-1.8 eV for Cu/Ta liner interface [56-59], and ~ 2.2 eV for the bulk [60]. In comparison, diffusion through the bulk and Ta liner interface is small and can be ignored. Therefore, the dominant diffusion pathways for Cu interconnects are the Cu/SiCN interface and the Cu grain boundaries. Accordingly, the

effective diffusivity term can be simplified as

$$D_{eff} = \frac{\delta_N}{h} D_N + \frac{\delta_{GB}}{d} D_{GB} \quad (2.4)$$

However, for diffusion along the Cu grain boundaries, an additional parameter to consider is the geometric factor defining the average orientation of the grain boundaries relative to the current flow direction. For instance, if a grain boundary is aligned perpendicular to the direction of current flow, the component of momentum transferred to the Cu ions by the moving electrons along the grain boundary diffusion path is zero. In contrast, if a grain boundary is geometrically aligned in the direction of current flow, the component of momentum transferred along the grain boundary is maximum. Therefore, equation 2.4 can be modified to define the parameter $Z_{eff}^* D_{eff}$ as

$$Z_{eff}^* D_{eff} = \frac{Z_{eff}^* D_N \delta_N}{h} + \frac{Z_{GB}^* D_{GB} f \delta_{GB}}{d} \quad (2.5)$$

where f is the geometric parameter accounting for the inclination of the boundary relative to the current flow direction [50]. This parameter and d , the grain size are statistical in nature, depending on the grain structure characteristics in the Cu line. For small equiaxed grains, there will be a higher proportion of grain boundaries aligned with the current flow, so the value of the $\frac{f}{d}$ ratio will be larger than that of a bamboo grain structure, where the grain boundaries span the width of the line, and are aligned nearly perpendicular to the current flow direction [50].

Although the aforementioned equations account for atomic flux driven by the EM driving force, for EM mass transport resulting in void formation, it is necessary to have flux divergence due to unbalanced flow rate. Mathematically, it can be represented by the continuity equation

$$dC = -\nabla J \quad (2.6)$$

where C is the atomic density of the metal and J is the atomic flux. The flux divergence for a given volume is equal to the atomic density change rate within that volume. Under the 'electron wind' force, voids can nucleate at flux divergence sites and grow to cause EM failure [61]. The EM lifetime is inherently statistical in nature and is related to the rate of damage formation at the various flux divergence sites. In Cu interconnects, flux divergence sites are commonly located at the grain boundary triple points, grain boundary/interface triple points, or the geometric discontinuity points. Apart from the grain structure and grain boundary distribution, the orientation of the grains normal to the Cu trench would affect the diffusivity at the Cu/capping layer interface, thereby impacting the flux divergence. Hu et. al [57, 62] and Ho et. al [50] showed that in the case of EM void formation at the cathode end of a single damascene Cu line with trench depth h , the EM lifetime τ can be written as

$$\tau = \frac{(\Delta L_{cr}) h k T}{Z_N^* D_N \delta_N e \rho j (1 + \frac{fgh}{d})} \quad (2.7)$$

where $g = \frac{Z_{GB}^* D_{GB} \delta_{GB}}{Z_N^* D_N \delta_N}$ is the ratio of the mass transport via grain boundaries vs. the cap interface.

2.3.2 Stress Induced Voiding

Stress induced voiding (SIV) or stress migration (SM) is another major reliability issue in Cu interconnects. SIV occurs due to hydrostatic stresses generated in the Cu lines during thermal cycling at elevated temperatures in the various IC fabrication processes [38]. The Cu lines, confined by the dielectric material and deposited on a thick Si substrate are subjected to elastic confinement effects during thermal cycling due to a difference in the coefficient of thermal expansion (CTE) between Cu and the underlying substrate. The average thermal stresses of a film deposited on a substrate can be expressed in the form

$$\sigma_0 = \frac{E_f}{1 - \nu_f}(\alpha_s - \alpha_f)\Delta T \quad (2.8)$$

where E_f and ν_f are the Young's modulus and Poisson's ratio of the deposited film, α_s and α_f are the coefficients of thermal expansion of the substrate and the film respectively, while ΔT is the temperature change. These thermal stresses have been well investigated for Cu and the Al based interconnect structures [63-75]. Initially when Cu was investigated for applications as interconnects, the smaller CTE of Cu (16.6 ppm at 298 K) compared to Al (23.6 ppm at 298 K) was thought to be an advantage for reducing the thermal stresses. However, the higher stiffness of Cu (120 GPa) in comparison to Al (72 GPa) offset this advantage. The product of the biaxial modulus and the difference in the CTE between Cu/Al and Si gives, -2.6MPa/°C for Cu and -2.3MPa/°C for Al [67]. This accounts for higher thermal stresses in Cu compared to Al for the same thermal cycling treatment.

2.3.2.1 *Stress State in Films and Lines*

A blanket film of Cu when deposited on a Si substrate (Fig. 2.6), upon thermal cycling experiences stresses according to Eq. 2.8. However, the stress state on the Cu film is isotropic biaxial where $\sigma_x = \sigma_y$ and $\sigma_z = 0$. In the case of unpassivated Cu interconnect, the isotropic biaxial stress state case changes to an unequal biaxial condition due to drastic variation in the in plane (x-y) dimensions of the interconnect, resulting in unequal magnitude of confinement in x and y directions. This can also be represented by $\sigma_x \neq \sigma_y$ and $\sigma_z = 0$. Finally, in case of a passivated Cu line, elastic confinement effects in all three dimensions result in a state of triaxial stress on the line where $\sigma_x \neq \sigma_y \neq \sigma_z$ and $\sigma_z \neq 0$. It can be seen from the graph in Fig. 2.6 that with increasing aspect ratio (thickness to width ratio) of the interconnect line, the magnitude of stress along the trench normal (z dimension) increases and the stress state becomes quasi-hydrostatic.

A change in the stress state from isotropic biaxial to quasi-hydrostatic also changes the stress relaxation mechanisms. It has been shown previously that while thin films undergo plastic yielding and relax stresses by dislocation mechanisms [72, 76-78], the deformation behavior in narrow passivated interconnect structures is largely elastic and occurs by void formation [79]. A qualitative understanding of the same can be developed using the von Mises criterion. For plastic deformation to occur, the von Mises stress (σ_v) given by

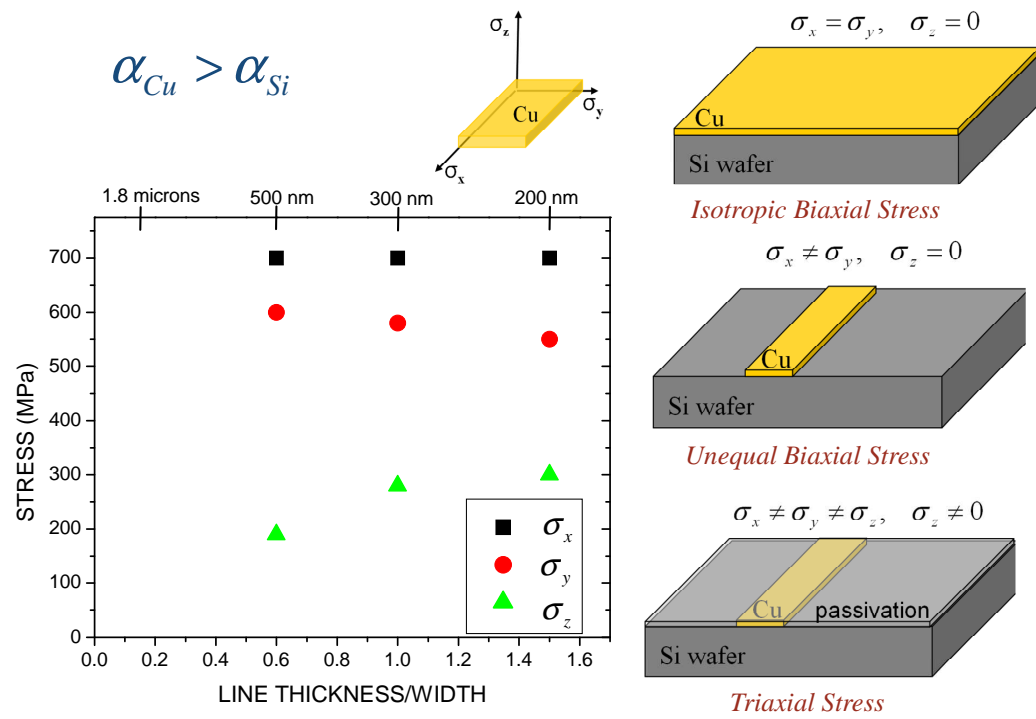


Figure 2.6: Stress state in blanket films, unpassivated and passivated Cu lines on Si substrate [6]

$$\sigma_v = \frac{1}{\sqrt{2}}[(\sigma_x - \sigma_y)^2 + (\sigma_y - \sigma_z)^2 + (\sigma_z - \sigma_x)^2] \quad (2.9)$$

must exceed the yield stress (σ_Y) of the material. Here σ_x , σ_y and σ_z represent the principal components of the stress tensor. In the case of a triaxial or quasi-hydrostatic stress condition occurring in Cu/Al line structures, $\sigma_x \neq \sigma_y \neq \sigma_z$ and $\sigma_z \neq 0$, the von Mises stress is less than the yield stress, and therefore yielding does not occur.

2.3.2.2 Factors Affecting SIV

SIV failures in Cu interconnects result from the formation of a void by diffusion and accumulation of vacancies. Vacancy motion leading to SIV is controlled by the diffusional mechanisms active within the material. Ogawa et al. [22] suggested three volumetric scales to define this diffusional problem from a mass transport perspective. The first is the interconnect volume within which the damage formation occurs. The second is the diffusion volume available during the thermal cycling time that can supply the vacancies needed to coalesce and form the void. The third is the stress gradient region which provides the necessary driving force for the vacancies to migrate towards a specific voiding site. The interconnect volume is dependent on the physical dimensions of the interconnect line. However, the concept of a diffusion volume is more complex, and depends on the active diffusion mechanisms present, the thermal cycling temperature and time. Only the vacancies lying within the 'active diffusion volume' would contribute to the voiding process. The

presence of a sufficient number of vacancies to form a void is dependent on the processing conditions. Vacancies are formed from either Cu grain growth during annealing or by process induced defects during CMP, etching and Cu trench/via filling [9]. The diffusion component of the active diffusion volume can be ascribed a characteristic diffusion length x_D such that

$$x_D = \sqrt{Dt} \quad (2.10)$$

where D is the diffusion coefficient and t is the bake time. The diffusion coefficient itself can be expressed by

$$D = D_0 e^{-E_a/kT} \quad (2.11)$$

where D_0 is the prefactor, E_a is the activation energy, k is the Boltzmann constant and T is the temperature. The activation energy for diffusion is strongly dependent on the overall microstructure, which includes grain texture, grain boundary types and the grain size. Therefore, from the aforementioned equations, it can be inferred that the active diffusion volume itself would be strongly dependent on the interconnect microstructure.

Finally, the stress gradient region is strongly dependent on the geometrical factors that define the interconnect system, the material properties of the interconnect metal (Cu), diffusion barrier layer and the dielectric. It is closely dependent on the distribution of local stresses within the interconnect line because the local stress gradients immediately affect the direction of motion of vacancies. Ogawa et al. [22] experimentally observed in Cu based dual-damascene technologies that the stress induced voids mostly formed under the

via when the via was connected to a wide metal lead below it (Fig. 2.7(a)). They inferred that a supersaturation of vacancies develops under the via in the wide metal line (providing a relatively large interconnect volume) during the grain growth process, prior to capping. This provides the required vacancy source. They also performed FEM calculations for hydrostatic stresses and showed a region of high tensile stress existing under the via. Their FEM analysis also revealed the presence of prominent stress gradients under the via that could potentially drive the vacancies under the via towards its bottom perimeter.

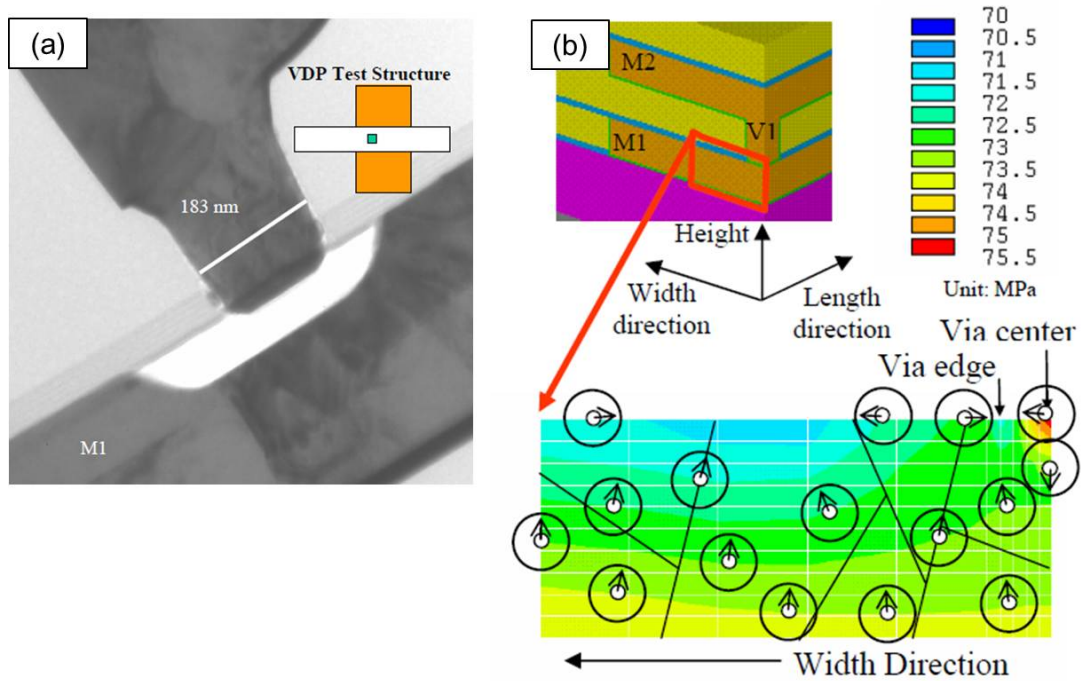


Figure 2.7: (a) Void formation under a via placed over a wide metal lead (b) Finite element analysis of dual damascene via placed over a wide metal lead showing hydrostatic stress contours. The white circles represent vacancies and the arrows depict their motion under the influence of local stress gradients [22].

As the interconnects are being scaled down and low-k dielectric materials are being integrated, it has also been observed that stress induced voids form along the Cu line structure, in addition to the underside of vias connected to wide metal leads. To understand such behavior, the concept of local stress gradients and active diffusion volume can be extended to the microstructure level. Structurally, it is well known that Cu is elastically anisotropic with an anisotropy factor

$$\frac{2c_{44}}{c_{11} - c_{12}} = 3.2 \quad (2.12)$$

where c_{ij} are the elastic constants. Consequently, the elastic modulus of Cu is different along different crystal directions. For instance, the elastic modulus along the $\langle 111 \rangle$ is approximately thrice the elastic modulus along the $\langle 001 \rangle$ direction. Fig. 2.8 shows the variation in elastic modulus as a function of angular distance from the $\langle 001 \rangle$. Therefore, the misorientation existing between the individual grains could affect local stresses and local stress gradients, thereby affecting vacancy motion and void formation. In addition to this, the grain size and the types of grain boundaries present in such regions of high stress gradients would play an important role in vacancy migration to form a void.

From the above discussion on interconnect reliability, it is clear that the microstructure of Cu interconnects strongly impacts EM and SIV induced failures. Therefore, as the interconnects are downscaled with each technology node, it is of paramount importance to understand the evolution of grain orientations (texture), grain structure and grain boundary distribution in these

lines to develop more reliable metallizations for future technologies.

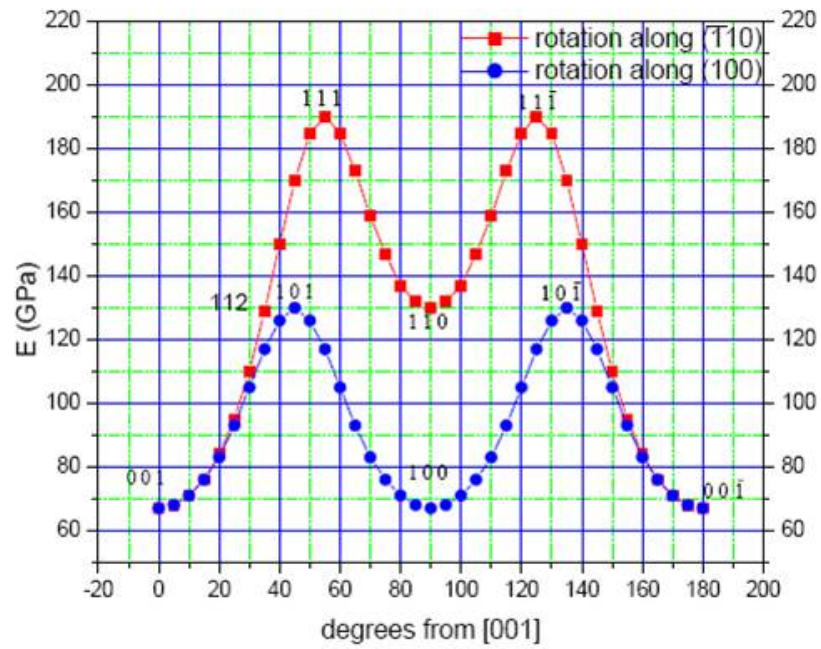


Figure 2.8: Elastic modulus of Cu plotted along different crystal directions [6]

2.4 Texture and Grain Boundaries

Before examining the evolution of texture and grain boundary distribution in downscaling Cu interconnects, a discussion on texture and grain boundaries is provided in this section to provide an insight into quantitative understanding of microstructure.

2.4.1 Grain Orientations and Texture

The orientation of a crystal with respect to its environment is a rotation on the three dimensional Euclidean space and can be represented by the group of orthogonal matrices with determinant $+1$. Three parameters are required to specify the crystal orientation. Parametrization for crystal orientations include Euler angles, the Rodrigues-Frank vector and unit quaternion parametrization [80, 81, 82]. The most commonly used description for rotation in three dimensions in quantitative texture analysis is the Euler angle parametrization. A general rotation transformation on three dimensional Euclidean space can be written in terms of three angles $(\varphi_1, \phi, \varphi_2)$, known as the Euler angles and can be understood geometrically in the following manner. Let \mathbf{x}' be the image of \mathbf{x} after the rotation transformation $\mathcal{O}(\mathbf{z}, \phi_2)$ and \mathbf{z}'' be the image of \mathbf{z} after $\mathcal{O}(\mathbf{x}', \Phi)\mathcal{O}(\mathbf{z}, \phi_1)$ (Fig. 2.9). In the above notation $\mathcal{O}(\mathbf{n}, \theta)$ represents a matrix specifying a rotation by an angle θ about an axis \mathbf{n} . A general rotation g can be decomposed as

$$g = \mathcal{O}(\mathbf{z}'', \phi_2)\mathcal{O}(\mathbf{x}', \Phi)\mathcal{O}(\mathbf{z}, \Phi_1). \quad (2.13)$$

The sequence of rotations are represented in Fig. 2.9. The set of three angles (ϕ_1, Φ, ϕ_2) is known as Euler angles for representing crystal orientation. The set of Euler angles calculated using the sequence of rotations in Fig. 2.9 is known as Bunge Euler angles and it is the convention used for the remainder of the work. The relation between Euler angles and the three dimensional rotation matrix is given as

$$g = \begin{bmatrix} c\phi_1 c\phi_2 - s\phi_1 s\phi_2 c\Phi & s\phi_1 c\phi_2 + c\phi_1 s\phi_2 c\Phi & s\phi_2 s\Phi \\ -c\phi_1 s\phi_2 - s\phi_1 c\phi_2 c\Phi & -s\phi_1 s\phi_2 + c\phi_1 c\phi_2 c\Phi & c\phi_2 s\Phi \\ s\phi_1 s\Phi & -c\phi_1 s\Phi & c\Phi \end{bmatrix} \quad (2.14)$$

where c represents *cosine* and s represents *sine* of the angle in the equation.

In a polycrystalline material, crystals of various orientations occur at different frequencies. In some cases, particular orientations occur more frequently and polycrystalline materials where this is observed are referred to as textured materials. For an aggregate of crystals with different orientations, it is useful to define a distribution function that gives the relative occurrence of a particular orientation. Such a function is known as the *Orientation Distribution Function* (ODF), defined as

$$\Delta V_{\Delta\xi}/V = \frac{\int_{\Delta\xi} F(g)dg}{\int_{\xi} F(g)dg} \quad (2.15)$$

where ξ represents the orientation space and $\Delta\xi$ is the particular orientation of interest. $\Delta V_{\Delta\xi}/V$ gives the volume fraction within the orientation $\Delta\xi$. The ODF is usually given as multiples of random distribution where $F = 1$ represents the frequency of occurrence of a particular orientation if the distribution of orientations is completely random [81]. Generalized spherical harmonics are used as the basis functions to describe the ODF and can be mathematically represented by

$$F(g) = \sum_{l=0}^{\infty} \sum_{m=-l}^l \sum_{n=-l}^l C_l^{mn} T_l^{mn}(g) \quad (2.16)$$

where $T_l^{mn}(g)$ is the symmetrized spherical harmonics. The spherical harmonics are expressed in the form of orthogonal Legendre polynomial functions, and involve the crystal orientation information obtained in the terms of Euler angles [81, 83]. This is mathematically given by the expression

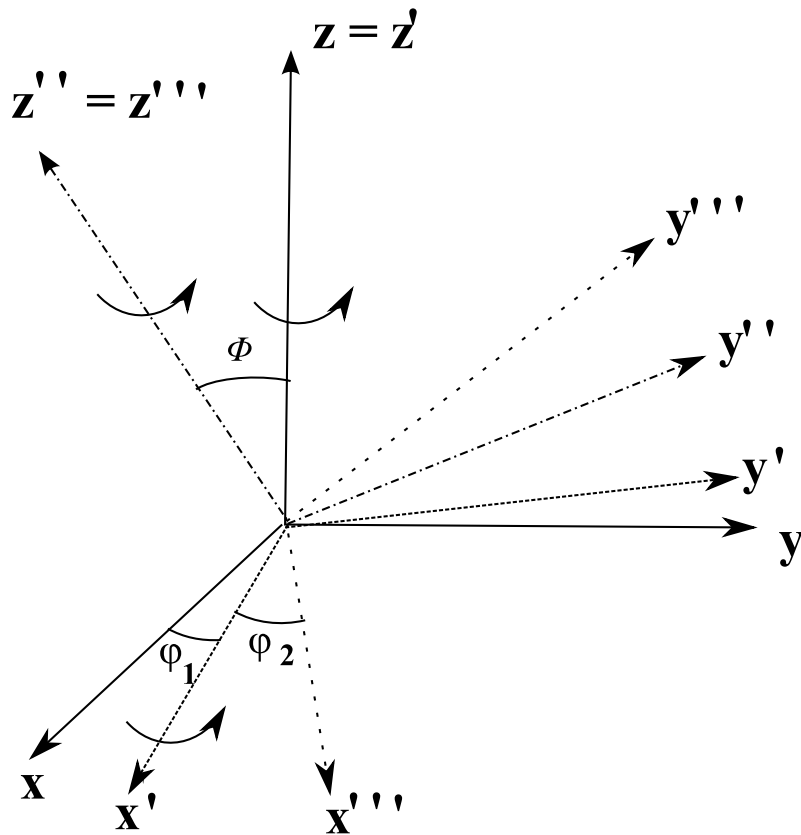


Figure 2.9: Euler angle parametrization of rotation on the three dimensional Euclidian space.

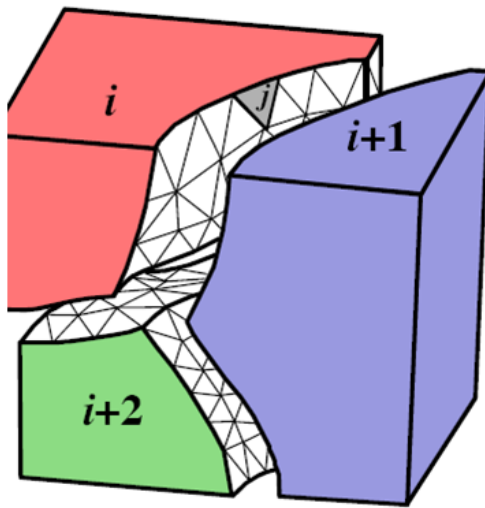
$$T_l^{mn}(g) = e^{im\phi_2} P_l^{mn}(\Phi) e^{im\phi_1} \quad (2.17)$$

where $P_l^{mn}(\Phi)$ are the associated Legendre polynomials. The number of terms needed in the series expansion to represent the ODF can be reduced by accounting for the crystal and sample symmetries [81].

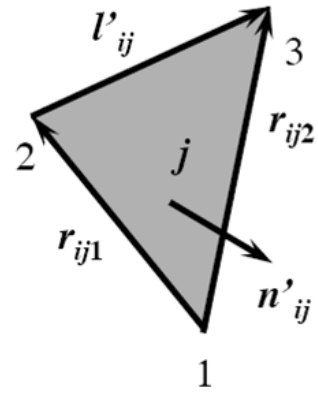
2.4.2 Grain Boundaries

A grain boundary is an interface that separates two crystals of the same phase that differ in their crystallographic orientation. Since this work is concerned with boundaries in a single phase material, the use of the term grain boundary refers to boundaries separating two crystals differing in their crystallographic orientation. This chapter gives an introduction to grain boundaries and their distribution in terms of the misorientation and the inclination of the boundary normal. A brief discussion on $\Sigma 3$ boundaries is presented. Detailed accounts on the structure and properties of grain boundaries are available in the literature [84, 85]. A general grain boundary can be described in terms of five macroscopic parameters: three parameters to describe the misorientation between the adjoining crystals and two parameters to describe the inclination of the boundary normal (Fig. 2.10). For a complete description of the boundary one also needs to specify the microscopic boundary parameters which are required to determine the atomic level translations at the boundary. The microscopic description of boundaries is difficult to realize experimentally and

the discussion of grain boundaries presented here is limited to macroscopic boundary parameters.



Three parameters for the
misorientation: $\Delta \mathbf{g}_{i,i+1}$



Two parameters for the grain
boundary plane orientation: \mathbf{n}_{ij}

Figure 2.10: Five parameter description of a grain boundary. The boundary surface is discretized into a set of triangles with each triangle described by a set of five parameters [86].

2.4.2.1 Grain Boundary Misorientation

If g_A and g_B be the orientation matrices of two adjoining crystals A and B , with respect to a reference orientation (Fig. 2.11). The misorientation matrix Δg is given by

$$\Delta g = g_B g_A^{-1}. \quad (2.18)$$

The misorientation matrix is the composition of the rotation that transforms the orientation of crystal A to the reference orientation and the rotation that transforms the reference orientation to the orientation of crystal B (Fig. 2.11). In other words, the matrix represents the rotation necessary to transform the crystal axes of crystal A onto those of crystal B . A useful description for misorientation is by the axis-angle representation $\mathcal{O}(\mathbf{r}, \theta)$. The misorientation in this representation is specified by giving the common axis \mathbf{r} in the two crystals and the rotation angle θ , known as the *misorientation angle*, about this axis needed to make the two crystals coincide with each other (Fig. 2.12). The axis-angle representation for a given misorientation is not unique and the smallest misorientation angle to specify a given misorientation is known as the *disorientation angle*. The disorientation angle is obtained by accounting for the various symmetry operations of the crystal. The misorientation matrix Δg is initially premultiplied by the each of the matrices representing the crystal symmetry operations. In the case of a crystal with cubic symmetry, (neglecting inversion symmetry), there are 24 such matrices [81, 87]. Subsequently, the misorientation matrix with the smallest trace (Δg_m) is used to calculate the *disorientation angle* and axis. Mathematically, the calculation for the smallest

misorientation angle (θ) is given by

$$\theta = \cos^{-1}\left(\frac{\text{tr}(\Delta g_m) - 1}{2}\right) \quad (2.19)$$

where $\text{tr}(\Delta g_m)$ is the trace of the matrix Δg_m . If the individual elements of the matrix Δg_m are represented by a_{ij} ($i, j = 1, 2, 3$), the misorientation axis ($U : V : W$) is given by

$$U : V : W = (a_{32} - a_{23} : a_{13} - a_{31} : a_{21} - a_{12}) \quad (2.20)$$

The distribution of grain boundary misorientations is also important in the quantitative studies of microstructure-property relationship. The *Misorientation Distribution Function* (MDF) $f(\Delta g)$ is the probability density of finding a particular boundary within the space used to parametrize the misorientation so that

$$\Delta A/A = \frac{\int_{\Delta\Omega} f(\Delta g) dg}{\int_{\Omega_0} f(\Delta g) dg}, \quad (2.21)$$

where ΔA is the total boundary area with a misorientation lying within the range $\Delta\Omega$ in the misorientation space and Ω_0 is the total volume of the misorientation space. For a random distribution of boundaries, the MDF has value of 1 everywhere. The MDF is given in units of multiples of random distribution (MRD).

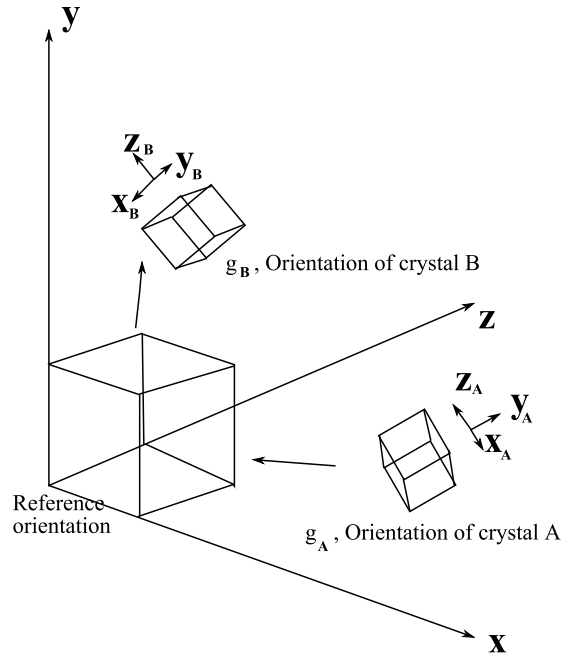


Figure 2.11: Misorientation between crystals *A* and *B* is the net rotation that transforms the orientation of crystal *A* to the orientation of crystal *B*.

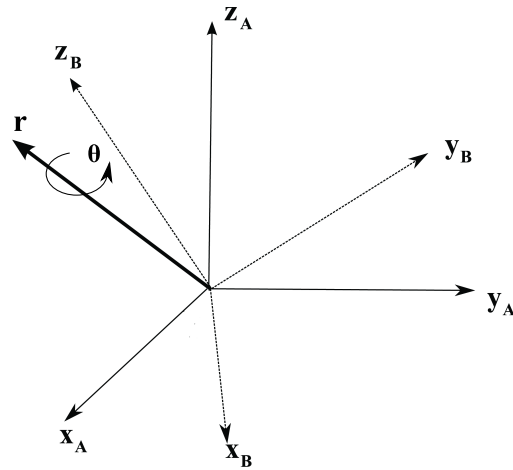


Figure 2.12: Axis-angle representation of the misorientation between crystals *A* and *B*. A rotation by θ about the axis \mathbf{r} transforms the orientation *A* to orientation *B*. \mathbf{r} is the common axis in the two orientations.

2.4.2.2 Grain Boundary Plane and Types

The orientation of the grain boundary plane (Fig. 2.10) can be described by specifying the orientation of the normal to the boundary plane. The set of all boundary normals can be represented as points on a unit sphere. The inclination of the grain boundary plane normal \mathbf{n} can be specified using the spherical polar coordinates (α, β) of the boundary normal with respect to the crystal frame of reference (Fig. 2.13). For the particular choice of Euler angle parametrization of the misorientation space and grain boundary plane normals represented using spherical polar coordinates (α, β) , a distribution f of boundaries can be defined with respect to a volume element dV in the five parameter space as

$$dA/A = f dV, \quad (2.22)$$

where dA/A is the fraction of the areas of grain boundaries with parameters in dV to the total area of the grain boundaries A . The volume element dV is given by

$$dV = (32\pi^3)^{-1} \sin \alpha \sin \beta d\alpha d\beta d\varphi_1 d\phi d\varphi_2, \quad (2.23)$$

where (α, β) are the spherical polar angles of the boundary normal and $(\varphi_1, \phi, \varphi_2)$ are the Euler angles. The distribution defined in Eq. 2.22 is referred to as the *grain boundary character distribution (GBCD)* and $f = 1$ is considered to be a random distribution of boundaries.

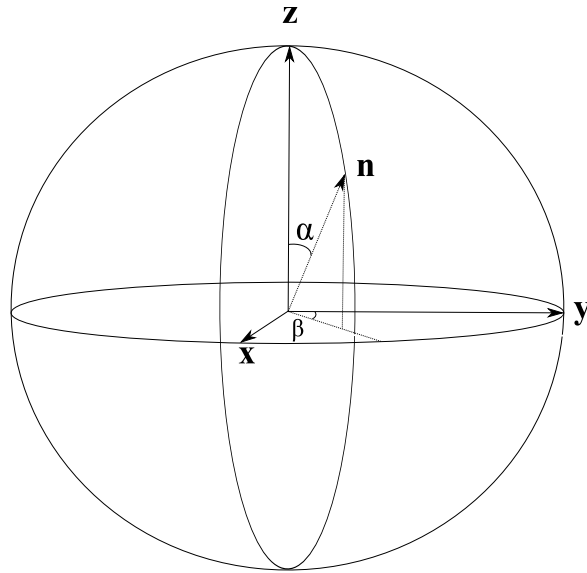


Figure 2.13: Spherical polar coordinates of the grain boundary plane normal \mathbf{n} with respect to the frame of reference of the crystal containing the boundary.

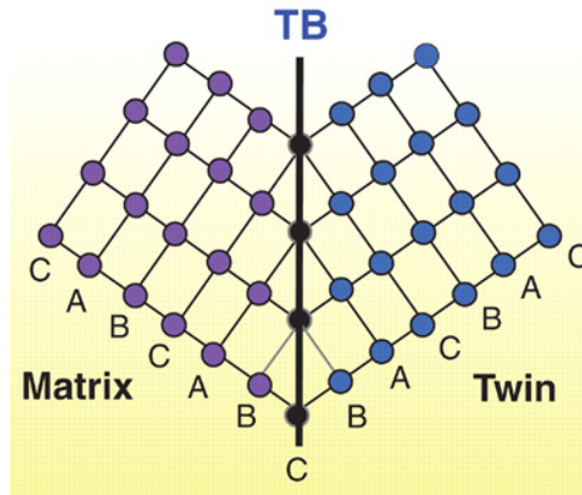


Figure 2.14: Coherent $\Sigma 3$ boundary. Reproduced from Lu et al. [88].

Twin Boundaries

Twin boundaries are special boundaries with specific orientation relationships between the grains such that the two adjoining lattices have a high density of coincident lattice sites. Boundaries with a high density of coincident lattice sites are interesting because of good atomic fit and hence lower energy. The crystallographic geometry of such boundaries is understood using the coincidence site lattice (CSL) model [89]. According to the CSL model, the boundaries are described using the Σ value, which is defined as the ratio of the area enclosed by a unit cell of the coincidence sites, and the standard unit cell. In other words, the Σ is the reciprocal density of coincident sites [87].

The $\Sigma 3$ boundaries in Cu are of particular interest due to their frequent occurrence and low energy [90]. In the axis-angle description, the $\Sigma 3$ misorientation is a rotation of 60° about the $\langle 111 \rangle$ axis (In terms of Euler angles: $(45^\circ, 70.53^\circ, 45^\circ)$). In coherent $\Sigma 3$ boundaries the grain boundary plane normal is oriented along the rotation axis resulting in a high degree of order in the atomic arrangement at the boundary (Fig. 2.14). The $\{111\}$ plane is the twinning plane for the $\Sigma 3$ misorientation. When the grain boundary plane for a $\Sigma 3$ misorientation does not coincide with the twinning plane, then the boundary is referred to as the incoherent $\Sigma 3$ boundary. The properties of coherent and incoherent $\Sigma 3$ can be significantly different. The special properties associated with $\Sigma 3$ boundaries such as low energy, low diffusivity and low mobility are valid only in the particular case of coherent $\Sigma 3$ boundaries. The incoherent $\Sigma 3$ boundaries with any other boundary plane are incoherent and can be treated

as regular high angle boundaries.

2.5 Techniques to Determine Local Orientation and Grain Boundary Texture

In general, X-ray diffraction and electron diffraction techniques in a TEM or SEM are used for analyzing grain orientations and grain boundary information in polycrystalline structures. The physical process of diffraction refers to elastic and coherent scattering of waves from scattering centers. Coherency of the scattering process preserves the precision of wave periodicity [91, 92]. In a crystal, atoms act as multiple scattering centers, and the emission of scattered waves by atoms of different types and positions results in constructive or destructive interference along different directions. Such interference results in maxima and minima of intensities which provide a spectrum of real space periodicity of the crystal [91]. The resulting pattern is called a diffraction pattern. In a common diffraction experiment carried out for crystal structure elucidation, the incident waves must have wavelengths comparable to the atomic spacings in the crystal [91].

2.5.1 X-ray Diffraction

X-ray diffraction (XRD) is the most commonly employed technique for determining texture information in polycrystals. In XRD, the oscillating electric field of the incident X-ray moves the atomic electrons and their accelerations generate an outgoing wave [91]. Experimentally, the intensities of the X-rays after interaction with the specimen are collected and plotted for various incident angles. As a geometrical construct, for a certain set of crys-

tallographic planes in the structure, an intensity maxima is observed when the incident angle satisfies the Bragg's condition.

$$2d_{hkl}\sin\theta_B = n\lambda \quad (2.24)$$

where d_{hkl} is the interplanar spacing of the (hkl) plane, θ_B is the Bragg's angle, λ is the wavelength of the incident x-ray and n is an integer representing the order parameter [93]. Analysis of the obtained data can provide a direct measurement of the average texture in the material. XRD can also be used to obtain strain related information in the structure and for accurate lattice parameter measurements [91, 93, 94]. Based on the peak width, x-rays can also be used to obtain the average crystallite size. However, since X-rays do not carry any charge, they cannot be deflected/focused by electric or magnetic fields to sample individual nanoscale grains for local texture. Thus, although XRD provides a wealth of quantitative microstructure information, other diffraction techniques are required to image and characterize local texture from individual nanocrystals in an ensemble.

2.5.2 Electron Backscatter Diffraction

The electron backscatter diffraction (EBSD) is a microstructure characterization technique employed in the SEM to obtain individual grain orientations, local texture, misorientations and phase identifications in bulk polycrystals. EBSD patterns are generated due to backscatter of a stationary high energy electron beam from the different planes in a crystal thereby generating

Kikuchi bands [95]. The geometry of a Kikuchi pattern can be interpreted as a gnomonic projection of the crystal lattice on the screen with the point of impingement of the primary beam on the specimen surface being the center of projection. The set of diffracted beams in three dimensions form pairs of cones oriented symmetrically about the diffracting planes [91]. Fig. 2.15(a) contains a schematic showing the incident beam on the specimen resulting in diffraction from a specific set of planes giving rise to backscatter Kikuchi diffraction. Fig. 2.15(b) shows a typical EBSD pattern taken from monocrystalline Si at 20kV beam energy. When more than one Kikuchi band is considered, the angles between the projected plane normal orientations correspond to the interplanar angles, and the angular width of the Kikuchi band $\{hkl\}$ is twice the Bragg angle. The extinction rules of the expected reflections for the crystal structure are determined by structure factor calculations.

EBSD analysis is carried out on a specimen which is tilted between 60° and 70° from the horizontal, which is the optimum position for examining the microstructure using backscattered electrons. Following such examination the specimen is tilted to the EBSD operating position, and the diffraction patterns are acquired on the phosphor screen. The pattern is either viewed through a high sensitivity camera through a window from outside the specimen chamber, or the phosphor screen is placed on a fiber optic bundle directly coupled to a camera sensor. The acquired patterns are then indexed in an automated manner using a template matching algorithm. Initially, during indexing, a Hough transformation is applied to the EBSD patterns [96, 97]. After the transforma-

tion each Kikuchi line is mapped to a point in Hough space. Subsequently, the transformed patterns are compared with precalculated templates using cross correlation [97]. The match with the highest correlation index is considered as the best solution. Since EBSD uses Kikuchi patterns which possess the actual crystal symmetry, for orientation determination, it has a high orientation resolution of the order of $\sim 0.1^\circ$ [97], which can be extremely valuable for extracting quantitative microstructure and strain related information. The complete process automation feature also allows for rapid and reliable orientation mapping of polycrystalline structures.

However the EBSD technique possesses certain disadvantages as well. Even while using a field emission gun (FEG) equipped SEM, the spatial resolution of EBSD falls more than an order of magnitude behind the resolution in conventional SEM imaging. This is because the inherent resolution of the EBSD is not governed by the diameter of the beam spot at the point of incidence on the sample surface, but primarily by the excitation volume i.e. the fraction of the interaction volume of the primary electrons within the sample from which the backscattered electrons leave the crystal (Fig. 2.16). Therefore, reducing the probe size to below the diameter of the interaction volume would not improve the resolution and in turn would adversely affect the beam current. This interaction volume also increases for light materials and higher beam voltages. Therefore, to improve the spatial resolution, EBSD is performed by lowering the beam voltages to below 20 kV. However, this results in significant lowering of the beam brightness and consequently the pattern in-

tensity collected on the screen. Thus, as a consequence of the steep sample tilt and the elongated projection of the beam spot, the lateral spatial resolution of EBSD at its best in a FEG SEM is about 25 nm for Cu [97].

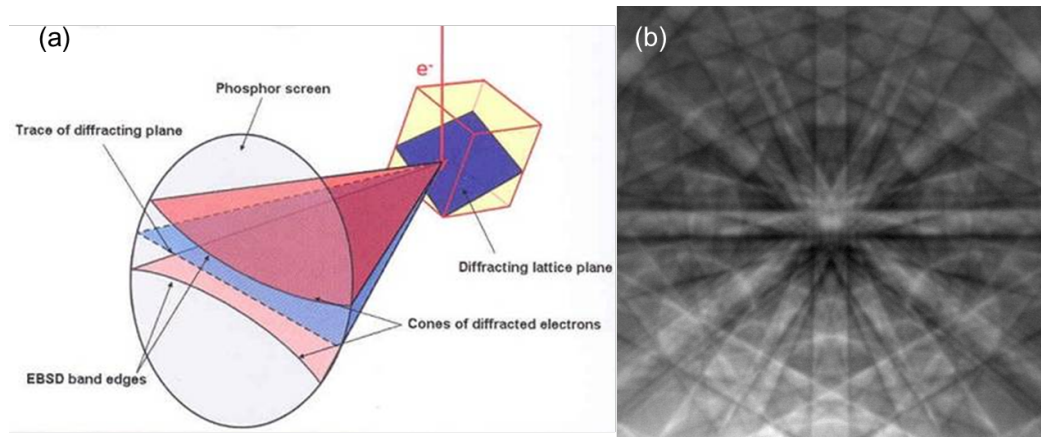


Figure 2.15: (a) Schematic of the diffraction plane with respect to the reflecting plane, specimen and the phosphor screen (b) Kikuchi pattern taken from monocrystalline Si at 20 kV beam energy

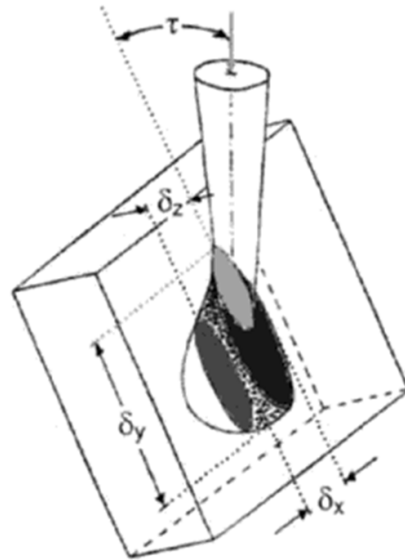


Figure 2.16: Interaction and excitation volumes in EBSD

2.5.3 Electron Diffraction in TEM/STEM

The existing electron diffraction techniques in a TEM/STEM are selected area diffraction, nanobeam diffraction and convergent beam diffraction.

2.5.3.1 *Selected Area Diffraction*

Selected area electron diffraction (SAD) is the oldest and most common technique employed for obtaining spot diffraction patterns from crystals. In this process, a parallel electron beam is incident on the specimen. The electron ray-path at such a setting is depicted in Fig. 2.17. A selection aperture called the intermediate aperture is inserted coplanar with the image in order to allow only the transmitted and diffracted rays emanating from the selected area to enter the remaining magnification system. Insertion of such an aperture at the image plane, which is conjugate with the specimen creates a virtual aperture in the plane of the specimen. Then, the intermediate lenses are adjusted to project the back focal plane of the objective lens onto the viewing screen. Consequently, although all electrons from the specimen contribute to the diffraction pattern formed at the back focal plane, only those from the region of interest are allowed to contribute to the diffraction pattern formed on the viewing screen/CCD camera [91]. The coherent incident illumination in SAD results in the production of sharply defined diffraction spots. The high resolution obtained in reciprocal space is particularly useful for perfect crystals. However, the sample volume contributing to the diffraction pattern is limited by the aperture size in the image plane and the aberrations in the

objective lens. Since it is very challenging to make apertures smaller than about 5-10 μm , and the demagnification back to the specimen plane is about 25X, the minimum area that can be selected is of the order of 0.2-0.4 μm [98]. This renders SAD unsuitable for obtaining diffraction information from individual nanocrystals within an ensemble. Fig. 2.18 illustrates the aforementioned problem associated with SAD. It is evidently impossible to obtain a spot diffraction pattern from an individual nanoparticle in the cluster because of the large aperture size. Instead, the pattern obtained contains diffraction information from the group nanoparticles encompassed by the aperture (Fig. 2.19).

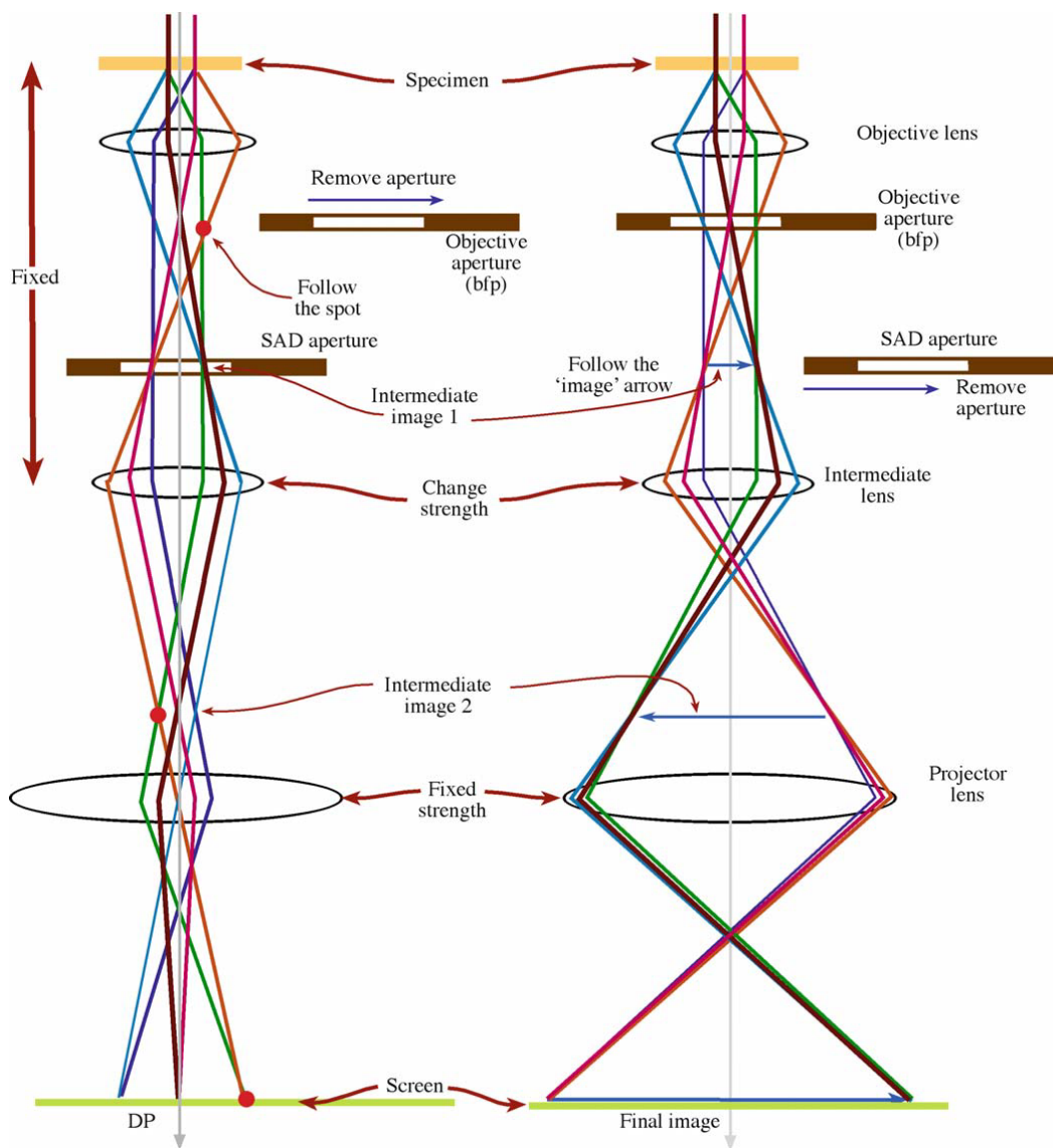


Figure 2.17: SAD and imaging mode in a TEM [Williams, 2008]

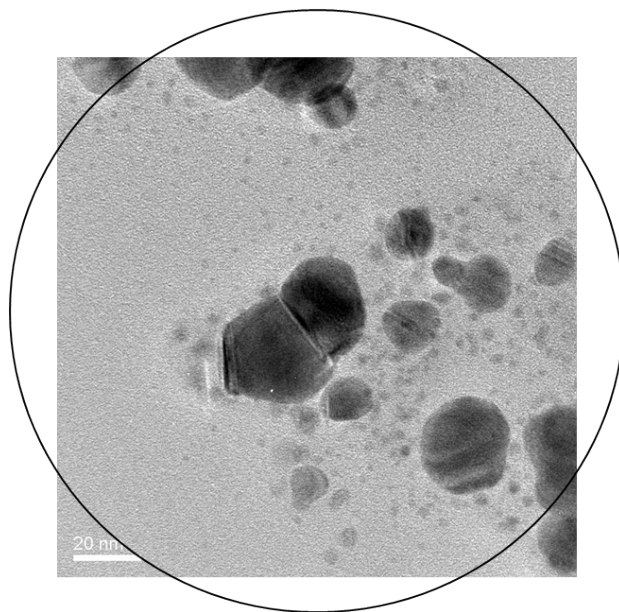


Figure 2.18: Bright field TEM image of Ag nanoparticles. The circle depicts the approximate area selected by the intermediate aperture

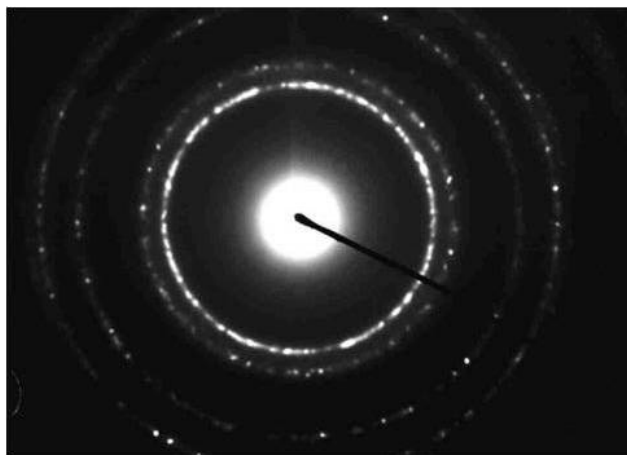


Figure 2.19: Typical selected area diffraction pattern obtained from a cluster of nanostructures

2.5.3.2 *Nanobeam Diffraction*

The nanobeam diffraction (NBD) technique was developed to obtain spot patterns from individual nanosized crystals. In this technique, improvement in spatial resolution compared to SAED has been achieved by limiting the area of illumination on the specimen. The NBD technique uses a nano-sized quasi-parallel illumination, which enables the formation of sharp spots in the diffraction plane and subsequent easy indexing. A schematic of the pre-specimen electron ray path in NBD is depicted in Fig. 2.20. In this mode, excitation of the first condenser lens (C1) is stronger than in conventional TEM/SAED illumination condition in order to achieve a greater demagnification of the electron source. This results in an effective reduction of the spot size on the specimen. A small condenser aperture (10 or 20 μm) is also employed to reduce the convergence angle of the beam. The cross over formed above the front focal plane of the objective pre-field lens results in a quasi parallel illumination. Consequently, this results in sharp maxima at the back focal plane of the objective lens. Although NBD results in the production of easily indexable spot patterns, the reduced beam size affects precise positioning of the beam at the nanostructure of interest. Frequent toggling required between TEM and NBD modes may also result in beam shifts, which is undesirable. These limitations makes this technique tedious for obtaining diffraction information from a large number of nanosized grains. Furthermore, the inability to automate this process makes this method extremely time consuming if attempted to be used for characterizing numerous grains.

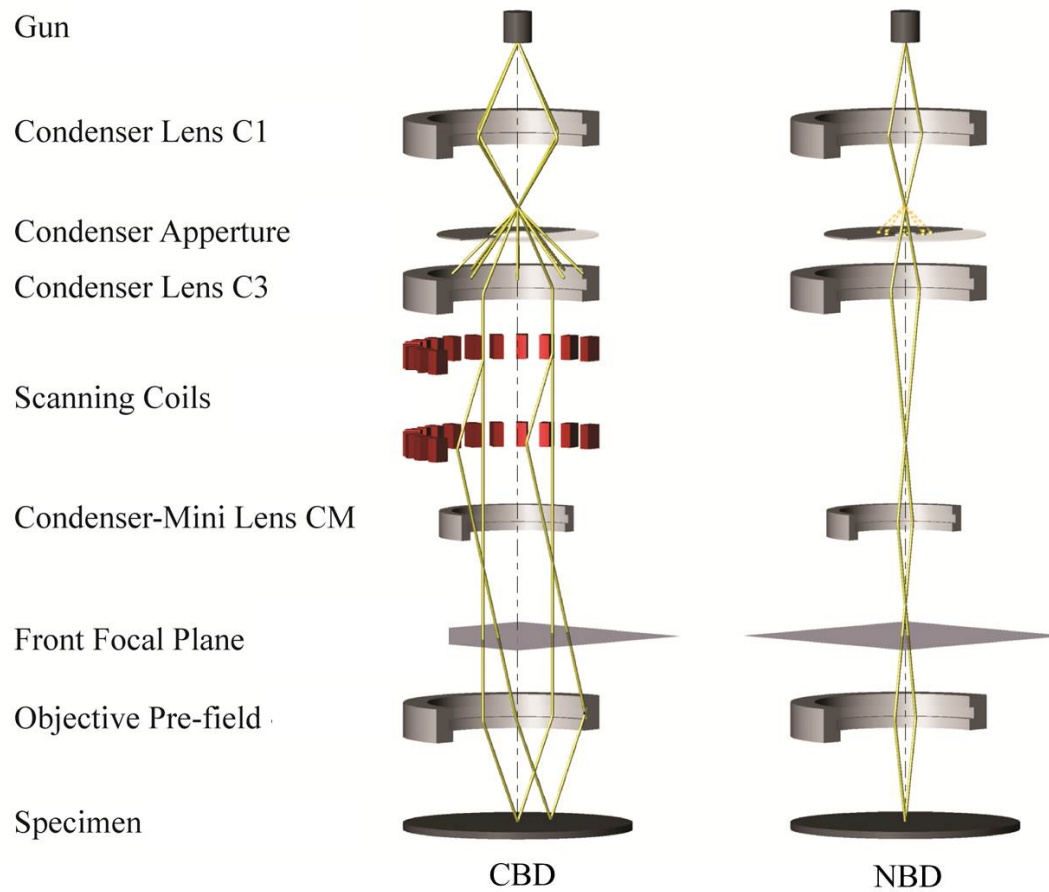


Figure 2.20: Electron ray path in CBD and NBD

2.5.3.3 *Convergent Beam Diffraction*

In the previously discussed SAD and NBD conditions, the incident electron beam is a plane wave traveling in one direction, usually parallel to the optic axis, represented by a single wave vector. In convergent beam diffraction (CBD), the incident electron beam is a cone of electron waves impinging on the sample over an angular range (semi-angle of convergence). This phenomenon can be visualized in reciprocal space as a continuum of Ewald spheres rocking about the origin over the same angular range [91]. This results in a diffraction pattern consisting of discs instead of spots. In modern electron microscopes, CBD can be performed in a TEM/STEM mode. From an optics perspective, as depicted in Fig. 2.20, the first condenser lens is strongly excited to greatly demagnify the electron source. Usually, in order to obtain a large convergence angle at the specimen, a large condenser aperture ($>40 \mu m$) is used. Since, the CM lens is deactivated, parallel rays following C3 set up a virtual source at an infinite distance for the objective pre-field lens. This results in a sharply converged probe at the specimen, which is at the focal plane of the objective pre-field lens. As a consequence of having incident electrons over a range of angles, the diffraction pattern consists of disks. Some scattering vectors that have larger components along the z-direction cause higher-order Laue zones (HOLZs) to become visible in diffraction patterns, which makes diffraction in CBD mode, a three-dimensional phenomenon. The obtained diffraction disks carry a wealth of information regarding the structure of the specimen and can be used to determine lattice parameter, point group and space group of the

crystal [91, 98].

However, it is challenging to index the disks accurately, particularly for local orientation determination due to possible disk overlaps and contrast variations within the disks. Furthermore, when operated in the TEM mode, CBD like NBD requires frequent toggling between the image and diffraction modes. This can be a potential cause for beam shifts, which is a significant problem affecting accuracy, especially while operating on individual nanostructures, often separated by just a few nanometers. In the particular case of CBD, the STEM mode can also be employed. In this fashion, it is possible to obtain a scanned image using a convergent probe, while acquiring diffraction patterns without the need for switching between the image and diffraction modes. This improves the accuracy with which a region can be selected. In addition, the scanning of the beam reduces the risk for specimen damage, while beam shifts can also be minimized. However, the presence of diffraction discs would still pose problems during pattern-indexing.

2.5.3.4 *Other nano-area diffraction techniques*

With the growth of nanotechnology, other novel nano-area diffraction techniques were developed to address the problems associated with conventional electron diffraction techniques. Cowley et al. [99] showed that the use of a convergent beam in the STEM mode, combined with the use of a small aperture and optimum defocus of the electron beam on the specimen, reduced the size of the diffraction discs, thereby reducing disc overlapping. Kolb et

al. [100] used this approach in a Technai F-30 FEG TEM/STEM equipped with a small condenser aperture (10 mm), to obtain a quasi-parallel beam for coherent electron diffraction while in STEM mode. This technique generated probe sizes between 15-50 nm at the specimen. Similarly, He et al. [101] developed a nano-area parallel beam diffraction STEM method on a Libra 200 FEG microscope, using Kohler illumination. By altering the condenser defocus, a quasi-parallel electron beam of 80 nm diameter was achieved on the specimen. Although these methods were capable of obtaining spot patterns from individual nanostructures, the relatively large beam diameters still posed challenges for obtaining isolated diffraction information from a dense ensemble of small nanosized crystals. In addition, problems associated with possible beam shifts while switching between convergent and parallel illumination modes still persisted.

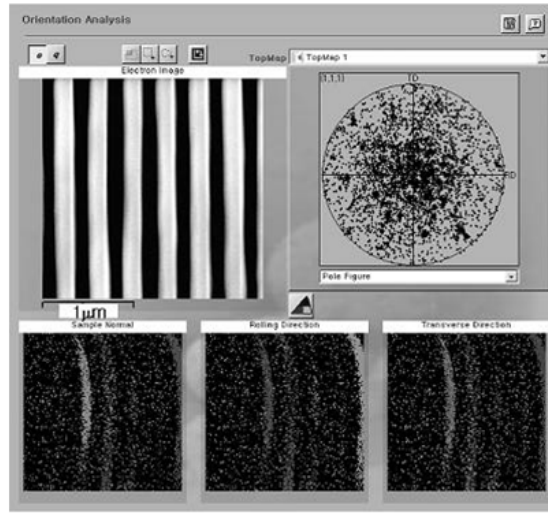
2.5.4 Microstructure Changes in Downscaling Cu Interconnects

The aforementioned diffraction techniques have been used by numerous researchers to understand the evolution of annealing textures in Cu interconnects as a function of downscaling. Among these techniques EBSD and XRD have been most commonly used. Lee et al [102] analyzed the texture changes in electrodeposited Cu interconnect specimens ranging from $6\mu m$ to $0.2\mu m$ in trench width using EBSD. They found that the $0.2\mu m$ wide lines had a $\{111\}\langle 110\rangle$ texture wherein the $\{111\}$ grains grew normal to the trench with a $\langle 110\rangle$ orientation along the trench length. Minor textures of the

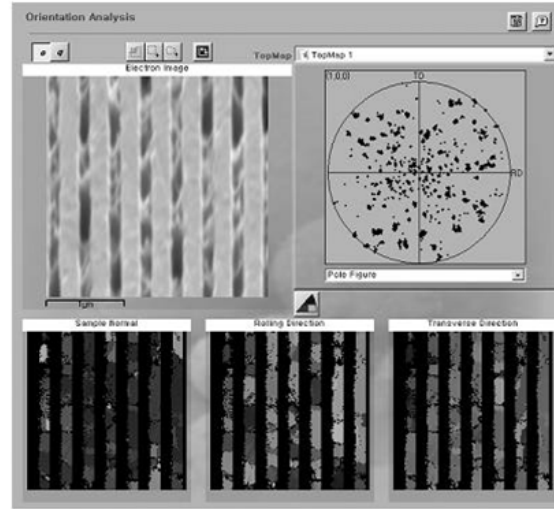
twin components of $\{115\}\langle 110 \rangle$ and $\{115\}\langle 141 \rangle$ were also found. In the wider lines, $0.5\ \mu m$ - $2\ \mu m$ in trench width, $\{111\}\langle 112 \rangle$ orientation dominated with a weaker fiber component while the $4\ \mu m$ and $6\ \mu m$ wide lines showed mixed $\{111\}\langle 110 \rangle$ and $\{111\}\langle 112 \rangle$ component textures. The texture evolution is discussed on the basis of stress and strain energy distributions. They mention that when the polycrystalline deposit having a fiber texture is annealed under balanced stresses, the resulting annealing texture is always of a fiber character irrespective of whether the resulting texture differs from the deposited one or not. They also account for the elastic anisotropy of Cu and discuss that to minimize the overall strain energy of the system, selective growth occurs for the grains aligned with the minimum Young's modulus direction along the direction of maximum stress. Similar findings have also been observed by Cho et al. [103] in electrodeposited Cu lines less than $2\ \mu m$ in width who observed $\{111\}\langle 110 \rangle$ texture and minor $\{115\}$ type textures.

Kim et al. [24] also investigated the microtexture of $0.18\ \mu m$, $0.25\ \mu m$, $0.70\ \mu m$ and $2\ \mu m$ wide damascene Cu lines using EBSD. They observed strong $\{111\}$ textures for the $0.18\ \mu m$ and $0.25\ \mu m$ lines. Minor $\{114\}$ and $\{112\}$ textures were also observed in the $0.18\ \mu m$ and $0.25\ \mu m$ wide lines respectively. The $2\ \mu m$ wide lines showed a relatively weak texture. A major part of their work was directed towards addressing image drift issues during EBSD analysis on their test specimens. They mention that while analyzing specimens with multiple phases (capping layer, dielectric, metal line), different levels of charge accumulation can occur at the interfaces between the different

phases, and this can worsen drift issues. Therefore, they they shortened the measurement time and employed a selected area mapping technique with Au and C dual layer coating. The results of the orientation mapping with and without the selected mapping technique is shown in Fig. 2.21 The details of the technique can be found in the paper by Kim et al. [24].



(a)



(b)

Figure 2.21: Orientation mapping of 0.18mm width Cu interconnect line along normal direction, rolling direction and transverse direction. (a) Mapping of whole interested area without coating shows significant drift effects, (b) Selected area mapping with gold and carbon dual layer coating shows significant reduction in specimen drift during acquisition of EBSD patterns[24]

Besser et al. [26] also comprehensively investigated the microstructure of inlaid electroplated Cu lines as a function of annealing conditions, post-plating, and post-CMP using XRD and EBSD. The analysis was performed on lines with widths ranging from $0.35\ \mu m$ to $1.06\ \mu m$. Pole figure analysis was performed by tilting the sample to measure the entire population of a particular family of crystallographic planes relative to the surface normal. Pole plots generated by XRD from $1.06\ \mu m$ wide lines showed the (111) peak at 0° and the (11-1), (1-11) and (-111) at 70.5° . Similar results were obtained in the case of a blanket Cu film (Fig. 2.22). The lines also exhibited a reduction in (511) intensity, suggesting a reduction in the twinning relative to the blanket films. As the linewidth decreased from $1.06\ \mu m$ to $0.35\ \mu m$, the (111) intensity reduced and sidewall nucleated (111) grains were observed. The (11-1), (1-11) and (-111) peaks also exhibited asymmetry (Fig. 2.23). These observations were explained by the fact that for lines, the (111) grains nucleated and grew from both the trench bottom and the sidewall. Therefore, the pole plot obtained was the sum of these individual contributions from the trench bottom and the trench sidewall. The (111) grains that nucleated from the trench bottom were also found to have a [110] type texture parallel to the trench sidewall. They also observed that the texture of $0.35\ \mu m$ wide lines was not strongly dependent on the presence of the overburden layer of Cu. In order to understand the independence of the Cu line texture on overburden, they performed cross-section analysis after post-plating anneal, prior to CMP. Their observations showed significant grain growth in the Cu overburden, but the Cu grains

in the overburden layer were not found to extend into the trenches. The (110) and the (100) pole plots also revealed the absence of $\{110\}$ and $\{100\}$ type textures in these lines (Figs. 2.24(a) and (c)) . However, the (110) pole plot (Fig. 2.24(b)) also showed increased intensity of the sidewall nucleated (111) grains at 90° tilt, suggesting a preferred in-plane orientation of $[110]$ along the trench bottom for the sidewall-nucleating (111). The authors explain that the sidewall growing grains are affected by the presence of the trench bottom in the confined structure, and that they minimize their total surface energy with this in-plane orientation.

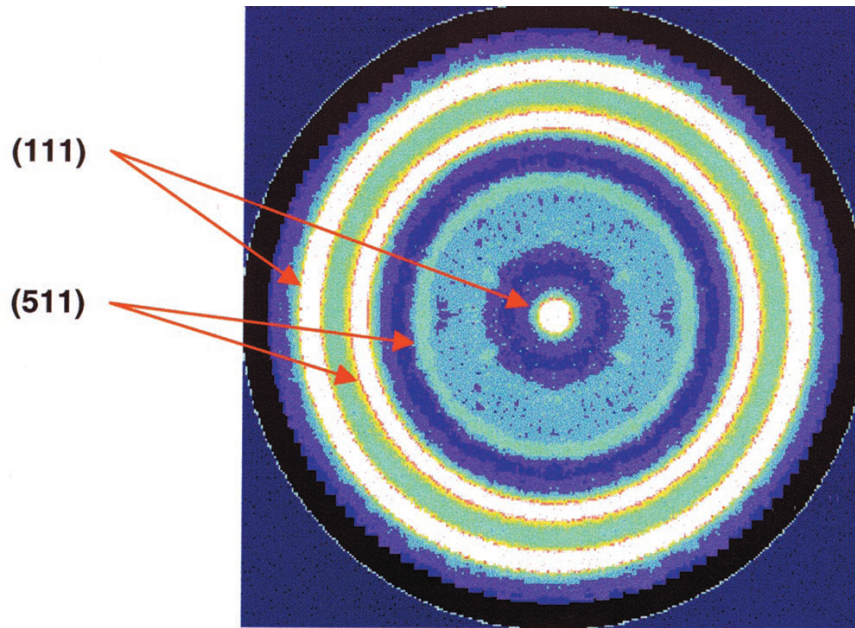


Figure 2.22: Stereogram showing the crystallographic texture for an annealed, blanket Cu film. The (111) pole plot shows that the Cu has a strong (111) fiber texture and (511) twins [26].

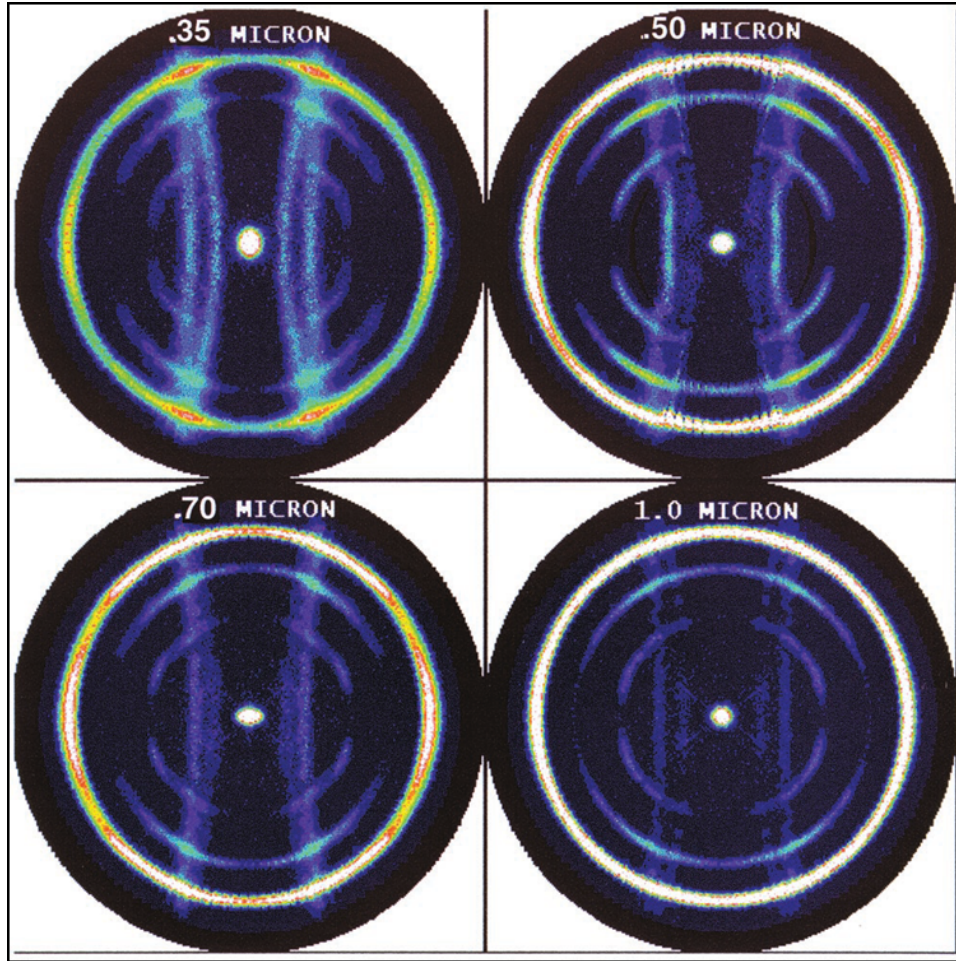


Figure 2.23: Stereogram showing the crystallographic texture results as a function of linewidth for inlaid Cu lines. The (111) pole plots for 0.35, 0.5, 0.7 and 1.06 mm show the lines are (111) oriented. The fraction of sidewall-nucleated (111) grains increases with decreasing linewidth [26].

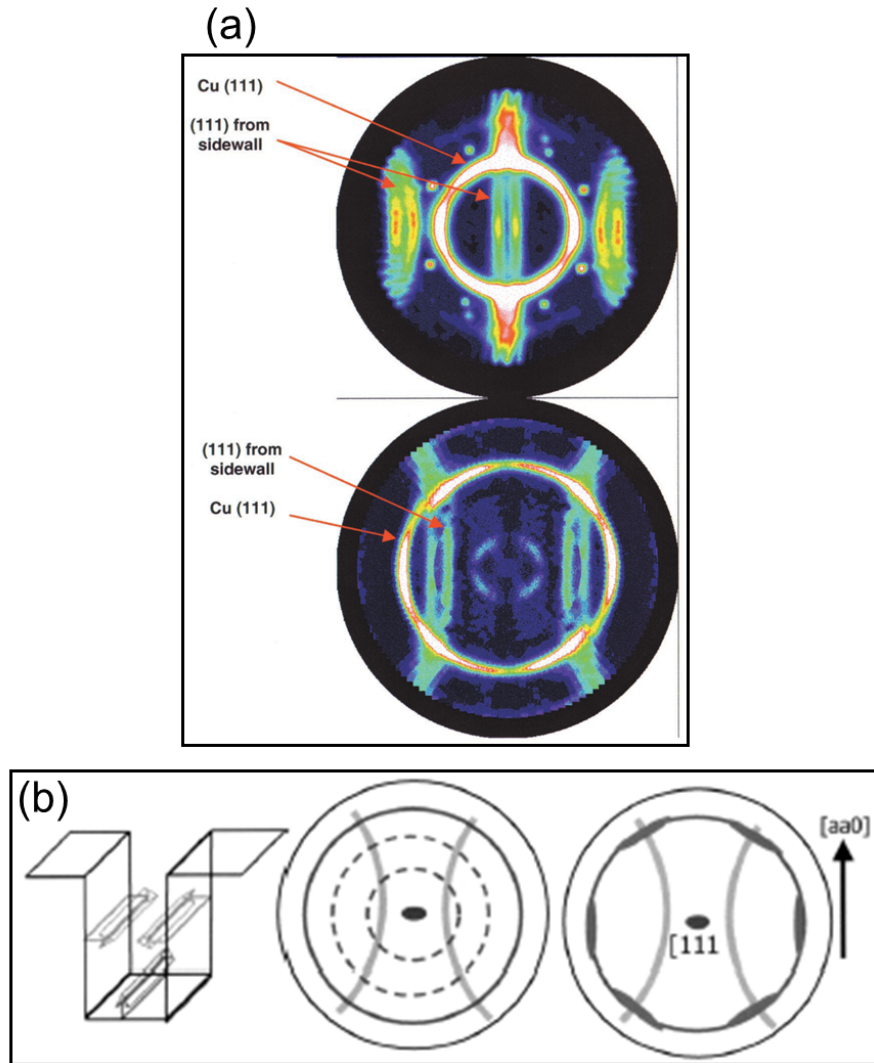


Figure 2.24: (a) Stereogram showing (110) and (100) pole plots for $0.35 \mu m$ lines, with no (110) or (100) oriented grains (b) Schematic drawings illustrating the development of (111) texture in lines and the influence of these texture components on the pole plot. For lines with vertical sidewalls, (111) grains grow from the trench bottom and sidewall. Sidewall growing grains show a preferred [110] in-plane orientation [26].

Recently, Legros et al. [29, 30], using TEM studies have studied morphology evolutions on *in-house* fabricated Cu lines with line widths of 80 nm, 250 nm and 3 μm . Specifically, they have investigated the influence of the overburden layer on the final microstructure of the interconnect lines with different annealing treatments. They observed that the grain structure of wide (>250 nm) Cu lines was strongly connected to the grain structure of the overburden layer. However, as the line width was downscaled to 80 nm, the invasion depth of the overburden layer reduced. Even annealing treatments at 400°C only resulted in a minor increase in the invasion depths. Furthermore, they propose that other parameters, such as the line section, side taper of the trench geometry, intrinsic stress states and chemical contamination of Cu grains can affect this invasion mechanism.

Chapter 3

Experimental Procedure

3.1 Materials

This section discusses the fabrication procedures of the materials investigated for orientation, phase mapping and also details of the sample preparation techniques for TEM observations.

Copper Interconnects

Sample fabrication: Periodic Cu interconnects with line widths of 1.8 μm , 180 nm and 120 nm were fabricated using the damascene process by Freescale Semiconductor, Inc. The 70 nm wide periodic damascene Cu lines were obtained from Texas Instruments, Inc. The thickness of the underlying Si wafer was 750 μm . Fluorinated tetra-ethyl orthosilicate (F-TEOS) was deposited as the interlayer dielectric (ILD) material for the 1.8 μm and 180 nm wide lines. The 120 nm wide lines were embedded in a carbon-doped oxide (SiCOH) dielectric, while the 70 nm lines were separated by a porous SiCOH dielectric. Ta was used as the diffusion barrier layer for Cu. The electrodeposited Cu was annealed at 250°C for 30 minutes before the chemical mechanical planarization (CMP) process. Subsequently, the silicon carbon nitride (SiCN) capping layer was deposited by chemical vapor deposition (CVD). The dimensional specifi-

cations of the different layers are shown in Table 1. A representative schematic of the structure in cross section is shown in Fig. 3.1.

Line Width (nm)	Trench Depth (nm)	Capping Layer Thickness (nm)	Aspect Ratio
1800	260	50	0.14
180	260	50	1.44
120	200	20	1.74
70	144	15	2.05

Table 3.1: Dimensional specifications of the Cu interconnect specimens with varying line widths

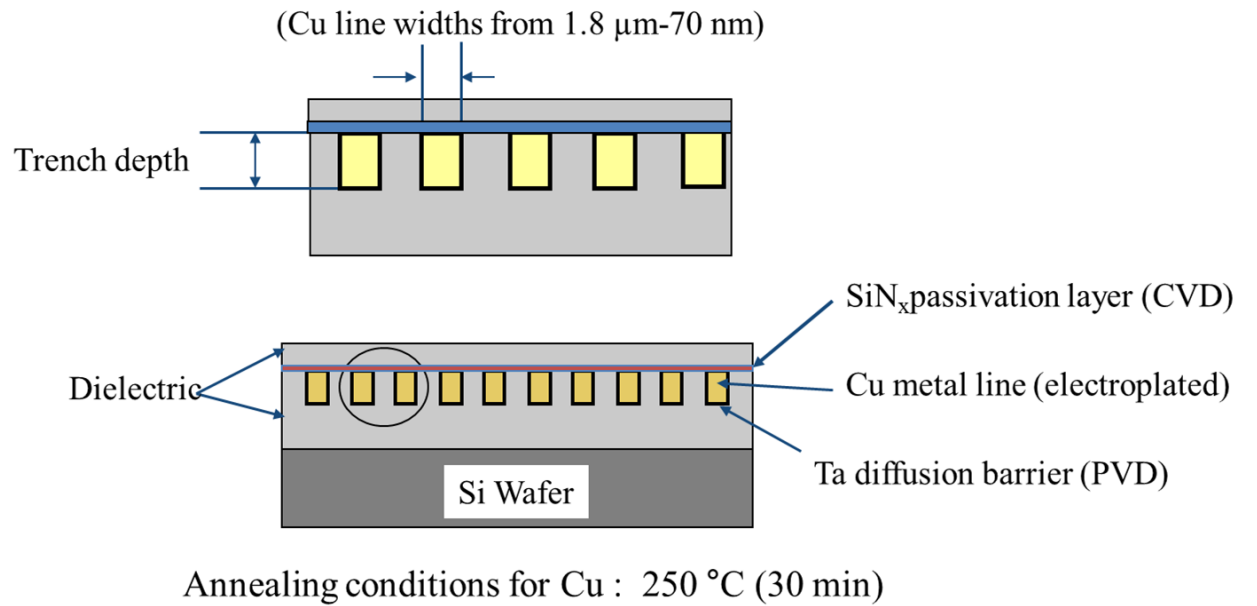


Figure 3.1: Schematic of Cu interconnect sample in cross section

TEM sample preparation for planar view observation: Electron transparent samples for planar observations in a TEM were prepared using conventional sample preparation methods. The sample preparation consisted of disc cutting, mechanical polishing, dimpling and ion milling. A Fischione 150TM Ultrasonic Disk Cutter was used to cut a 3 mm disc from the wafer. The disc was then mechanically polished from the underlying Silicon side using a diamond lapping film with grit sizes in order of 30, 15, 3, 1, and 0.5 μm to a thickness of $\sim 100 \mu m$. The sample thickness during lapping was accurately controlled by using a Gatan Tripod PolisherTM. The polished sample was dimpled to a thickness of $\sim 4 \mu m$ using a GatanTM 656 Dimpling GrinderTM. The sample was then ion-milled to electron transparent thickness with a Gatan 691 Precision Ion Polishing SystemTM (PIPS) using 3.0 KeV/3.0 mA beam at an angle of $< 5^\circ$. To minimize changes in the microstructure during TEM sample preparation, the ion-milling process was carried out under liquid Nitrogen conditions, primarily from the Si side. The top layer was milled for only a few minutes at 2.0 keV/2.0 mA to completely remove the ILD layer on top. It also ensured that the Cu grains in contact with the passivation layer were kept intact. This is important since the Cu/passivation interface is the fastest diffusion path during EM and SIV, and the orientation of the Cu grains in contact with this interface significantly affects the interfacial diffusivity.

TEM sample preparation for cross-section observation: TEM samples for cross-

sectional observations were prepared by the focused ion beam (FIB) technique using the FEI StrataTM 235 dual beam FIB equipped with a FEG. In FIB, a Ga ion source is employed, and the resulting ion beam is rastered to sputter the material from the target substrate. The instrument also possesses an electron gun inclined at an angle of 52° with respect to the ion gun that facilitates regular SEM imaging during the milling process. The technique allows for the precise fabrication of electron transparent specimens down to below 100 nm in thickness. Specifically, the trench-bar technique (H-bar) was employed to prepare the Cu interconnect samples [6]. The 3mm wide samples were initially thinned to $\sim 100 \mu m$. Subsequently, trenches were milled using the Ga ion beam resulting in a thin TEM sample. Finally, cleaning was done with a 30 keV/10 pA beam to minimize damage to the target specimen.

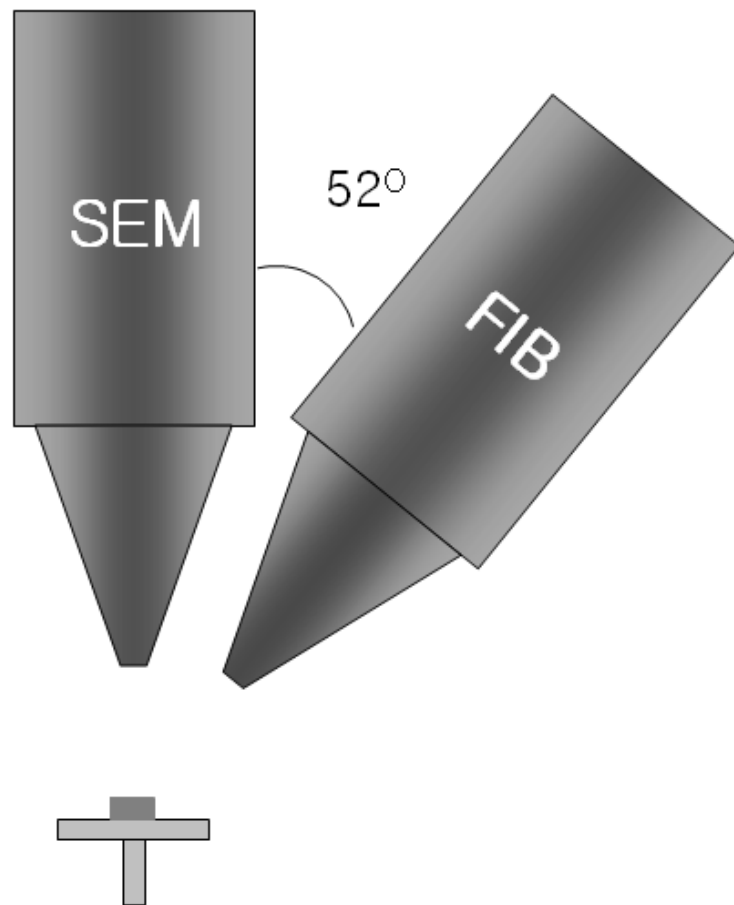


Figure 3.2: Schematic illustration of the dual beam FIB [An, 2007]

Pulsed Laser Deposited Nickel Films

The pulsed laser deposited (PLD) Nickel films were fabricated at Sandia National Laboratories and were analyzed for phase mapping (*In collaboration with Dr. S. Rajasekhara, Dr. J. Knapp and Dr. K. Hattar from Sandia National Laboratories*) 50 nm thick films were deposited on $\langle 001 \rangle$ NaCl crystals by the pulsed laser deposition technique. A KrF laser ($\lambda = 248$ nm), with pulse width of 34 ns full-width half-maximum, a pulse rate of 35 Hz, and an energy density of approximately 1-2 J/cm² at the nickel target was used to create a nickel plume that deposited on the NaCl substrate. The deposition rate was approximately 0.25 nm/s. Subsequently, thin bar AtheneTM 300 mesh TEM grids (Ted Pella, Inc.) were glued at the edges to the PLD Ni films using a few drops of M-bond 610TM adhesive. To prevent sample heating, the epoxy was cured at room temperature for at least one day. Later, the salt crystal below the film/grid assembly was dissolved away in a bath of de-ionized water. Finally, the remaining electron transparent film/grid assembly was carefully lifted out and dried at room temperature to be used for TEM observations.

Platinum Nanoparticles

Nanosized Pt cubes were fabricated by refluxing H₂PtCl₆ in ethylene glycol in the presence of polyvinylpyrrolidone (PVP) and tetramethylammonium bromide (TMABr). The synthesis was performed by C. Atkinson from Prof. Stevenson's research group at UT Austin. 0.75mmol of TMABr was

dissolved in 6mL of ethylene glycol and subjected to three cycles of vacuum purge and nitrogen flush. Using an oil bath and working under inert gas, the stirred reaction vessel was heated to 180 °C. The platinum mixture was purged with nitrogen and injected into the heated solution through a septum. The vessel was held at temperature for 30 min after the solution turned black at the onset of nucleation and allowed to cool. The platinum cubes were separated from solution by centrifugation after adding acetone. The concentrated particle precipitate was then re-dispersed in 8mL ethanol and filtered through Millipore Amicon UltraTM centrifugal filter units. The dispersion/filtration cycle was repeated twice more with water, and the final rinsed product was dispersed in 15 mL of water for storage. Subsequently, a few drops from the solution were collected and deposited on Cu grids (300 mesh) covered with lacey carbon for automated orientation analysis in the TEM.

3.2 Methods

3.2.1 D-STEM

In order to address the limitations of the existing electron diffraction techniques like EBSD, SAD, NBD and CBD, a novel parallel electron diffraction technique called D-STEM (Diffraction Scanning Transmission Electron Microscopy) was developed in a JEOL 2010F TEM/STEM instrument. In D-STEM, the electron optics inside the microscope were modified to obtain a 1-2 nm near-parallel illumination ($<1^\circ$ convergence) on the specimen in the STEM configuration [104]. This probe could be scanned to produce both bright-field

and dark-field STEM images. Subsequently, the probe could be positioned on the image at the nanostructure of interest, as small as 3 nm, to obtain sharp spot diffraction patterns. A schematic representation of the ray path in D-STEM is shown in Fig. 3.3. Furthermore, for automated acquisition of sharp spot patterns in the STEM mode, the D-STEM technique was coupled with the STEM Diffraction ImagingTM software from Gatan. The coupling of the two techniques combined the rich information of electron diffraction with the spatially resolved power of spectrum imaging (line and area scans) and thereby enabled a fast pixel-by-pixel acquisition of diffraction patterns.

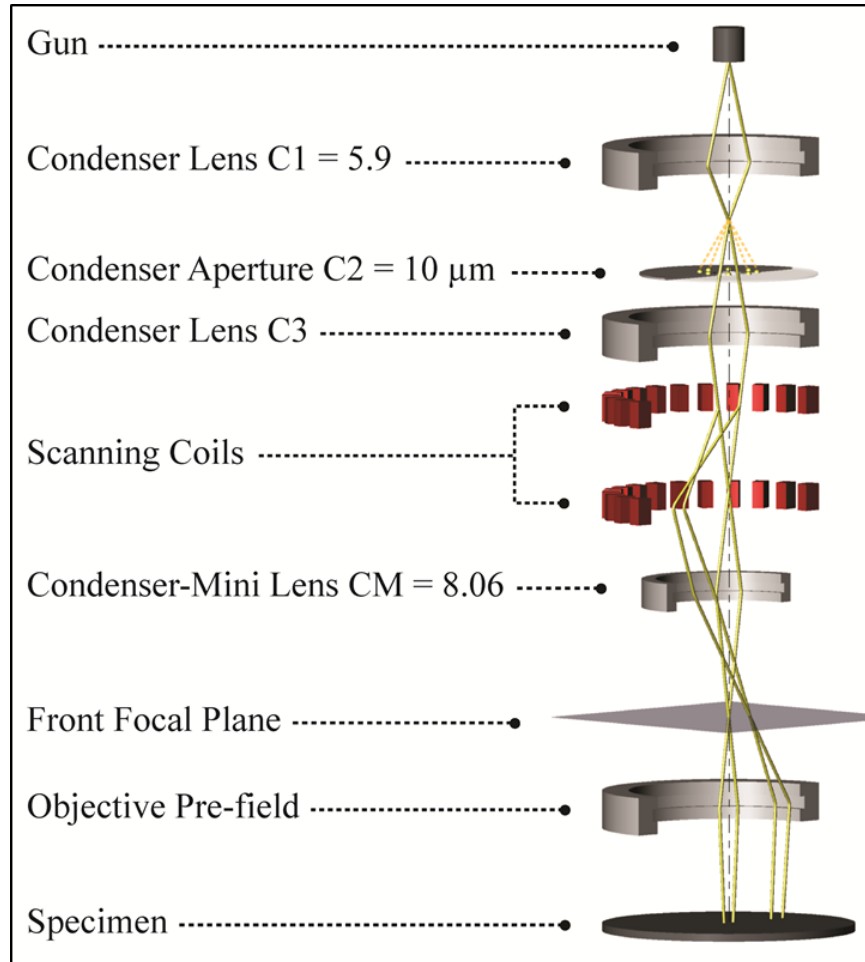


Figure 3.3: Schematic representation of ray path in D-STEM [Ganesh, 2010a]

Although the D-STEM technique can be used for automated diffraction pattern acquisitions, sometimes, crystals can be orientated off a prominent zone axis resulting in a quasi-two beam condition or a systematic row of reflections. An example of such a case is shown in Fig. 3.4. In such situations, it is impossible to index the crystal orientation accurately without significant specimen tilts in the microscope. This limits the automation features associated with the technique. In order to address this limitation, the a novel high resolution electron diffraction technique was developed by combining D-STEM with precession electron diffraction using the ASTARTM system from NanoMEGAS.



Figure 3.4: Diffraction pattern showing a systematic row of reflections

3.2.2 Precession Electron Diffraction

The use of specimen rocking as a means to reduce strong dynamical effects is well understood in X-ray diffraction [94]. By rocking the specimen, the intensities of the Bragg peaks in X-ray diffraction are integrated over various specimen orientations. This concept has been recently extended to electron diffraction. However, in electron diffraction instead of rocking the specimen, dynamical effects are reduced by precessing the incident beam about the optic axis. In precession electron diffraction, the incident beam is tilted with respect to the optic axis of the TEM, simultaneously rotated at a constant angle and scanned on the sample to obtain diffraction intensities integrated over the entire scan (Fig. 3.5). The use of precession in electron diffraction was introduced by Vincent et al. in 1994 [105]. As the incident beam undergoes deflection and is scanned conically, on the specimen, the diffraction pattern oscillates as well. To compensate for the movement of the diffraction pattern and keep the diffraction pattern stationary, the diffracted beams are tilted in a complementary manner. The net effect of such a scan-descan setup is equivalent to precessing the sample about a stationary focused beam. Fig. 3.6 shows a schematic ray diagram for the precession diffraction.

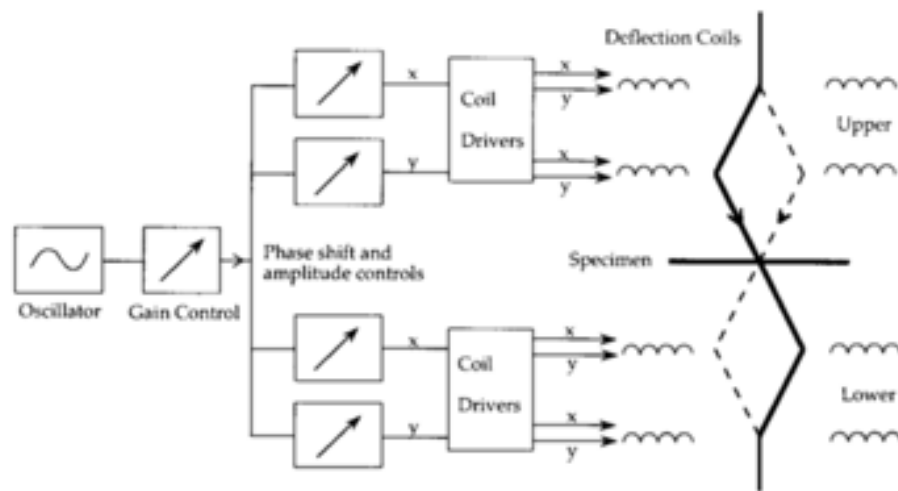


Figure 3.5: Block diagram of the set up for precession electron diffraction. Reproduced from Vincent and Midgley [104].

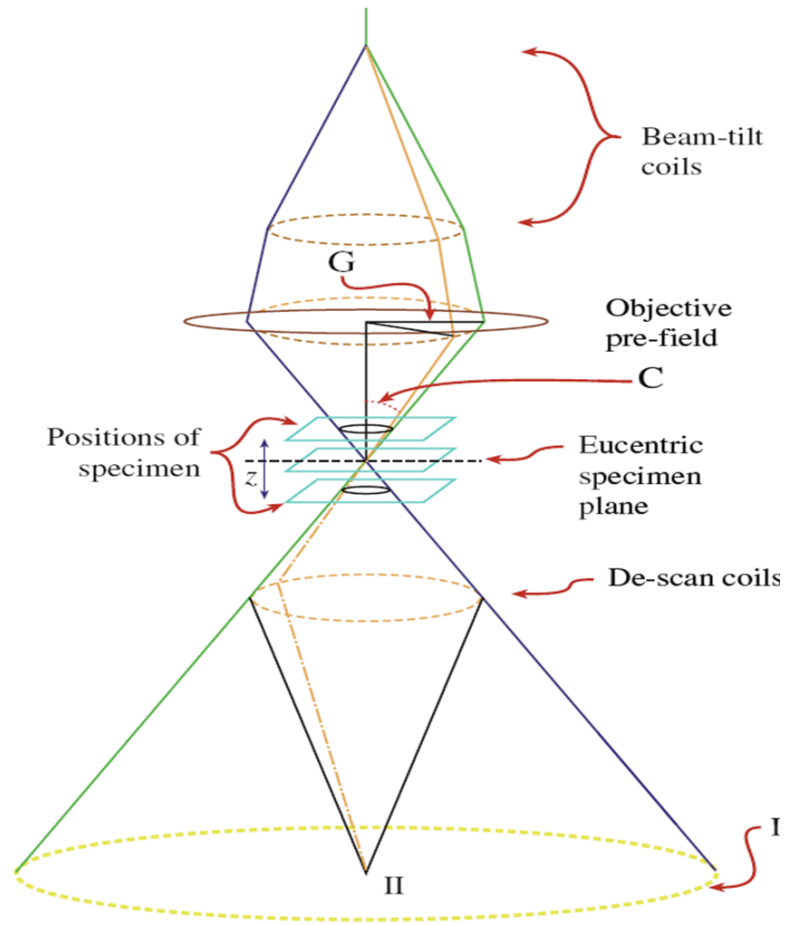
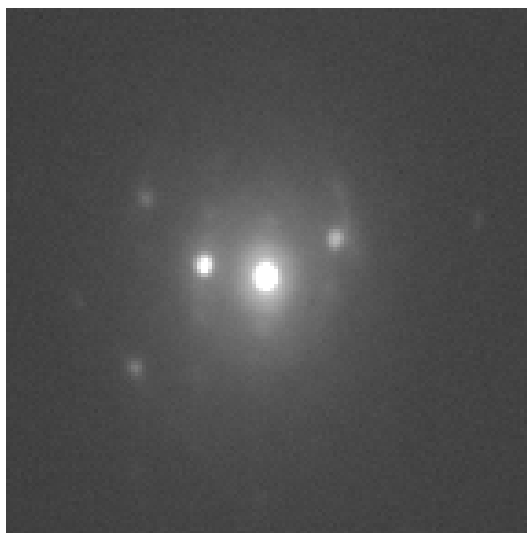
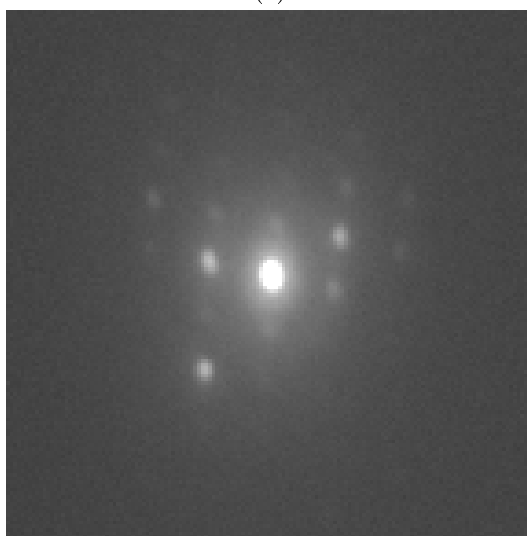


Figure 3.6: Ray diagram for precession diffraction, a double-conical beam rocking system. G is the radius of the conical diffraction and C is the precession angle [98].

When precession is employed, the observed diffraction pattern is an average of all the diffraction patterns within the precession cone. Since the intensities are integrated over many crystal orientations which are off zone axis, fewer beams are strongly excited simultaneously. Therefore, zone axis channeling and consequently, dynamical effects are reduced. Dynamical effects are reduced as the incident beam is not exactly on axis and fewer beams are excited simultaneously. Thus, precession diffraction can be used to achieve quasi-kinematical conditions [105-109]. Also, the use of precession enables the collection of higher order Laue reflections, which are useful in eliminating the ambiguities in indexing the spot diffraction patterns [107]. Additionally, it is possible to obtain quite symmetric patterns even when the crystal is off zone axis by 1° when precession is employed and hence, off zone axis patterns can also be indexed in a reliable manner. Due to the aforementioned advantages, the reliability of orientation solutions from patterns collected using precession is much higher. As an example of the improvement in the pattern quality when precession is employed, diffraction patterns from the same region acquired with and without precession are compared in Figs. 3.7(a) and (b). The reduction of dynamical effects with the use of precession can be observed by noting the disappearance of the Kikuchi lines Fig. 3.7(b). Also, the presence of more spots can be seen when precession is used.



(a)



(b)

Figure 3.7: Diffraction patterns from Cu samples with (a) no precession and (b) with a precession angle of 0.4° . Note the presence of faint Kikuchi lines when the diffraction pattern is collected without precession, which vanish with the use of precession.

3.2.3 D-STEM with ASTAR: The Instrumentation

The ASTARTM system comprises a dedicated unit called DigistarTM for externally controlling the beam and image deflector coils of the TEM (Fig. 3.8). Components from the DigistarTM unit were hardwired to the amplifiers of the individual deflector coils. Such a setting enabled automated precession and scanning of the incident electron beam. During precession, it also allowed complimentary descan of the beam below the specimen plane for collecting stationary spot patterns (Fig. 3.6). Initially, the D-STEM lens configuration was set up to achieve a 1-2 nm near-parallel illumination. Subsequently, the precession of the beam was enabled and a high frame rate external optical camera unit was mounted at an angle of 45° to the phosphor screen for rapid acquisition of the diffraction patterns. During acquisition, the viewing screen was tilted by the same angle so that the optical camera was aligned perpendicular to it. The acquired patterns were automatically indexed using a template matching software called ACOMTM. The following two subsections discuss the alignment and operating procedures for reliable orientation imaging using ASTARTM.

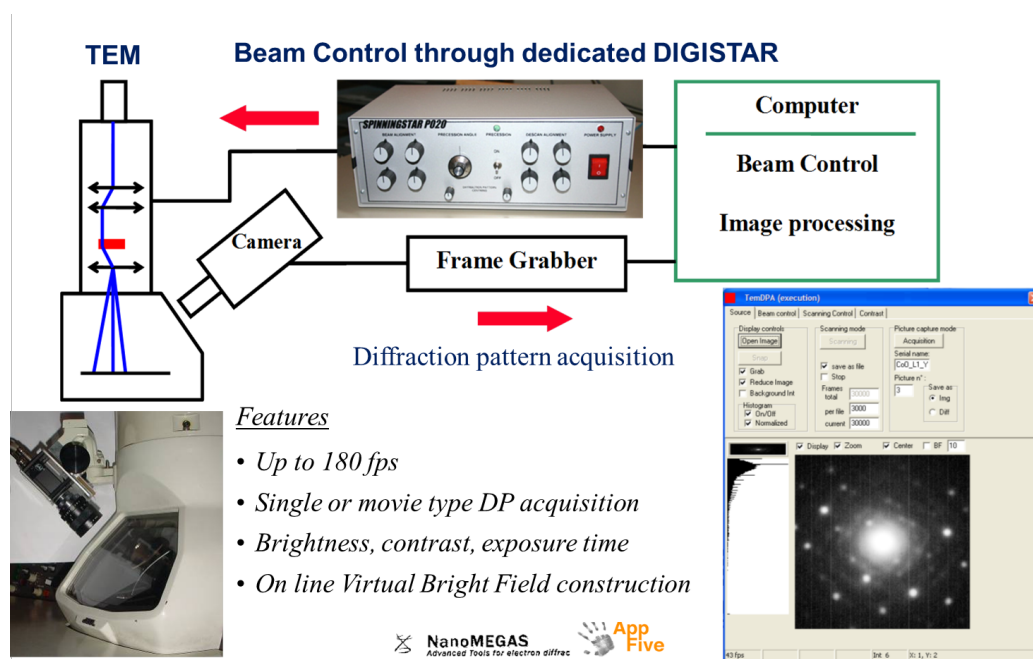


Figure 3.8: Schematic of hardware setup for the ACOM™ system. (Courtesy: E. F. Rauch).

3.2.3.1 *Alignment Procedure for Precession Using Digistar*

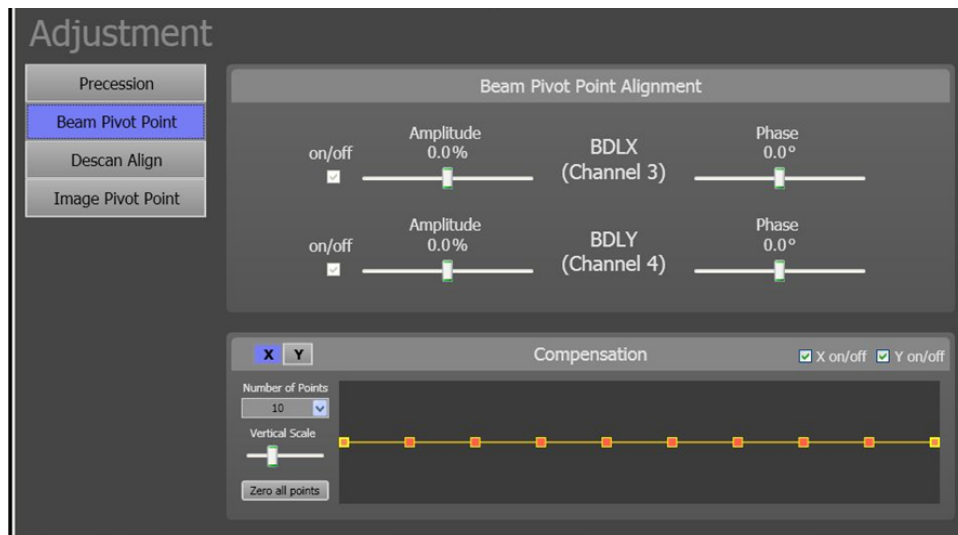
The main objective of the alignment procedures is to ensure that the incident beam, diffraction pattern and image are laterally stationary during precession. Specifically, the corresponding alignments can be categorized into: (a) beam pivot point (b) descant and (c) image pivot point. Before carrying out the alignments with a precessed beam, the basic TEM alignments like the high tension alignment, voltage center alignment and the condenser aperture alignments must be carried out with an unprecessed beam. The specimen of interest should also be located at the eucentric position and the objective lens excitation should be set to the reference value for the microscope. Usually a precession frequency of 100Hz is chosen

(a) *Beam pivot point alignment*: The beam pivot point alignment is carried out at the precession angle of interest to ensure that the incident beam is circular and stationary while it rotates. This alignment is carried out in the imaging mode by controlling the amplitude and phase of the external signal provided to the lower set of beam deflector coils in the X and Y directions (BDLX and BDLY). The amplitude and phase options can be changed in the adjustment panel of the GUI (Fig. 3.9(a)).

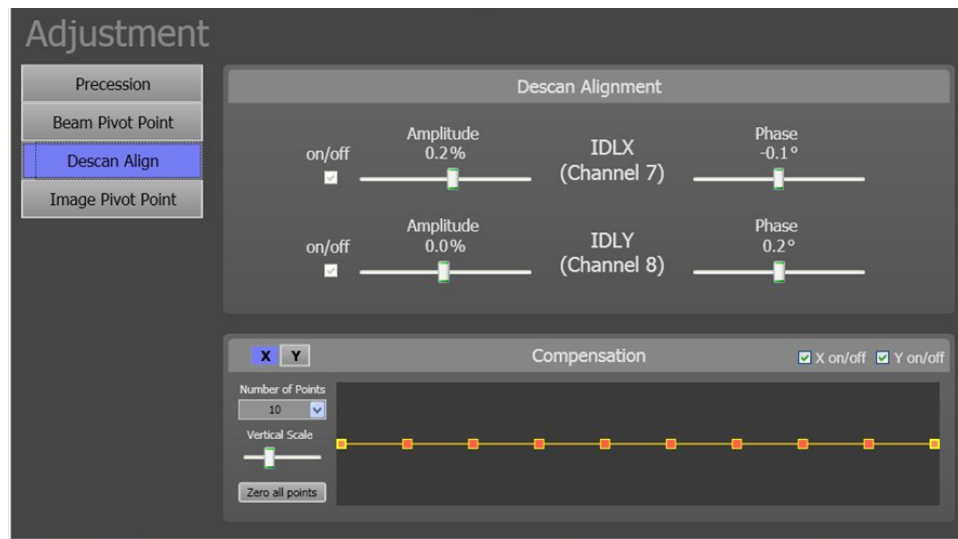
(b) *Descant alignment*: Descant of the beam refers to the complimentary tilt and rotation given to the inverted cone of electrons formed during precession below the specimen plane. The descant alignment ensures that the diffraction pattern formed at the back-focal plane of the objective lens remains stationary as the beam is precessed. This alignment is carried out in the diffraction mode

by controlling the amplitude and phase of the external signal provided to the lower set of X and Y image deflector coils (IDLX and IDLY) as shown in Fig. 3.9(b).

(c) *Image pivot point*: The image pivot point alignment is carried out to refine the eucentric adjustment of the specimen thereby ensuring that the apex of the precession cone lies on the specimen plane. In this alignment, the Z-height of the specimen in the microscope is adjusted with a spread beam, to obtain a sharp image. The combination of the beam pivot point and the image pivot point ensures that there is no lateral motion of the beam on the specimen plane as it precesses.



(a)



(b)

Figure 3.9: (a) Screen-shots from Digistar control for (a) Beam pivot point alignment (b) Descan alignment

Compensation adjustments: It is known that conventional alignments in a regular TEM can only correct up to 2 fold astigmatism. Sometimes, due to additional inherent aberrations of the microscope, especially revealed while precessing at high angles, the amplitude and phase adjustments can be insufficient to form a stationary circular probe. In such conditions, the compensation adjustment feature provided in the DigistarTM control panel can be employed. Compensation adjustments provide the freedom to distort the conventional sinusoidal waveform of the external signal supplied to the deflector coils. The signal can be divided into 10, 20 or 40 segments thereby dividing the waveform into sectors of 36°, 18° and 9° respectively. Subsequently, the default sinusoidal signal to the deflectors is superposed upon the compensating signal to achieve a circular, stationary electron probe. The compensation feature is provided for both the beam pivot point and descans modes. An example of a situation requiring compensation adjustments is shown in Fig. 3.10(a) where the precessed incident beam suffers from a *lacing effect*. To correct the complex beam distortions, initially, the beam is elongated along the Y direction (Fig. 3.10(b)). Then, a compensating amplitude is provided to the signal in the X direction (Fig. 3.10 (c)) to alter the beam shape to a pseudo-line (Fig. 3.10 (d)). The same process is repeated by elongating the beam along the X direction and correspondingly shaping the beam to a pseudo-line along the Y direction. Finally, the amplitude and phase controls in the adjustment panel for the beam pivot point or the descans alignment can be used to form a circular beam (Fig. 3.10 (e)).

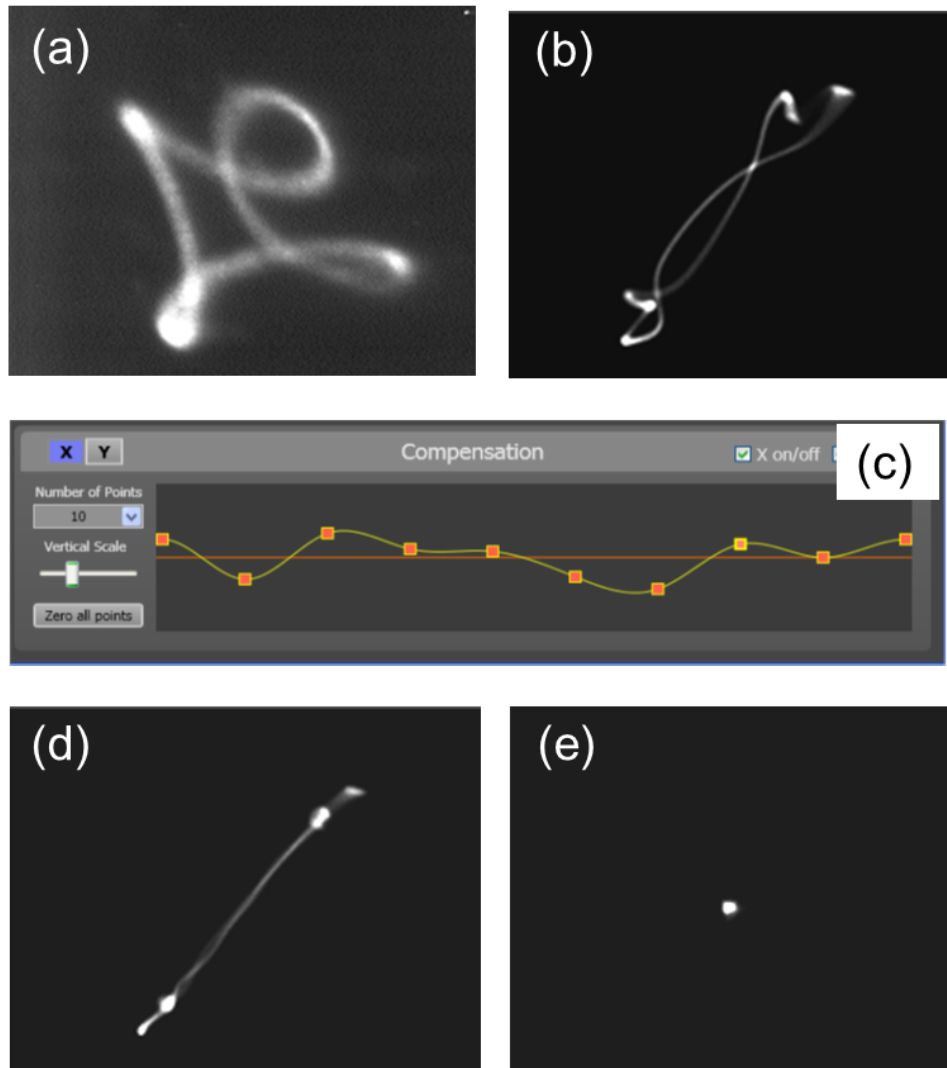


Figure 3.10: Examples from compensation alignment showing (a) lacing effect of the beam (b) elongation along Y direction (c) compensation adjustment along X direction (d) resulting pseudo-line along the Y direction (e) well aligned beam.

3.2.3.2 Automated Indexing Using ACOMTM

As previously mentioned, the ASTARTM system comprises a software called ACOM for automated indexing of diffraction patterns. Automated indexing of the spot diffraction patterns is achieved in the following manner [110, 111]. Initially spot patterns for a given material are generated for all the Euler angles in the fundamental zone depending on the symmetry of the crystal. Then every experimentally acquired diffraction pattern is converted to a polar image and the intensity at each (r, θ) coordinate (where r is the radius from the central spot and θ is the azimuth) is cross correlated with the generated templates. The best match for a given template is found by maximizing the correlation index $Q_i(x, y)$, which is defined for a pixel in the orientation map with coordinates with (x, y) gives the degree of matching between the diffraction pattern from this point and the template i and is given by the equation

$$Q_i(x, y) = \frac{\sum_{j=1}^m P(x_j, y_j) T_i(x_j, y_j)}{\sqrt{\sum_{j=1}^m P^2(x_j, y_j)} \sqrt{\sum_{j=1}^m T_i^2(x_j, y_j)}}, \quad (3.1)$$

where $P(x, y)$ and $T_i(x, y)$ give the intensities of the points (x, y) for the diffraction and the template i [111]. The maximum value of Q , known as the image quality or correlation index, for a given pixel corresponds to the best matching template. the reliability index¹ R_Q of an indexing solution as

$$R_Q = \left(1 - \frac{Q_2}{Q_1} \right), \quad (3.2)$$

¹The reliability index is also referred to as the confidence index.

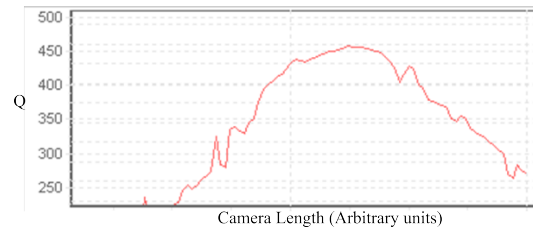
where Q_1 and Q_2 are the correlation indices for the two highest maxima. A vanishing R_Q implies that there is more than one solution to the given diffraction and it is not possible to specify a unique solution with the given information. This would be the case for patterns where the spot intensities is too low or the number of spots is not sufficient. This is also true for two overlapping patterns which would be the case at the grain boundaries. The reliability index is low for the patterns with the 180° ambiguity.

For the purpose of indexing, about 2500 templates were generated. Template bank is the collection of all the diffraction patterns generated for a given structure. For a template bank of this size, the disorientation between two successive templates is less than one degree. The indexing routine involves optimizing a number of adjustable parameters. Of the many adjustable parameters, optimizing two of the parameters was found to be critical for obtaining reliable indexing solutions. These two parameters are the camera length and the distortion correction. Each of these is discussed below.

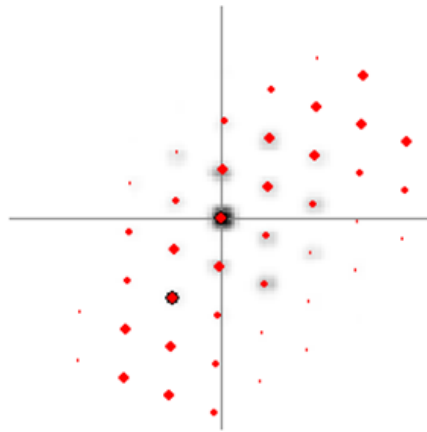
Camera Length: Camera length is optimized by selecting the camera length that maximizes the maximum correlation index Q for a given diffraction pattern. For the purpose of camera length calibration, it is important to select a diffraction pattern with many spots from the same crystal so that at the correct camera length the correlation index has a distinct maximum (Fig. 3.11). Camera length was optimized for indexing each acquisition.

Distortion: Since the electron diffraction patterns are collected on a plane inclined at 45° angle the diffraction pattern is always distorted. Without

correcting for the distortion, the orientation solutions will be incorrect. The distortion is corrected by stretching the image in the vertical direction and compressing in the horizontal direction (Fig. 3.12 (a)). An example of a diffraction pattern before and after distortion correction is shown in Figs. 3.12 (b) and (c). The distortion correction is determined by selecting a diffraction pattern for which the correct solution can be identified easily and then the distortion correction is determined by maximizing the correlation index for this solution. It should be noted that camera length and distortion should be optimized in an iterative manner.



(a)



(b)

Figure 3.11: (a) Variation of the maximum correlation index with camera length. (b) Overlay of the best matching template with the observed diffraction pattern.

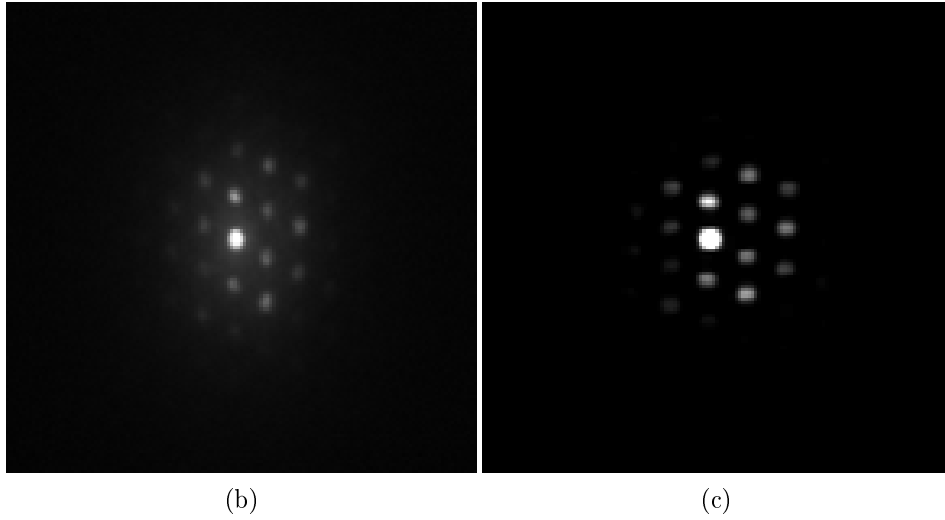
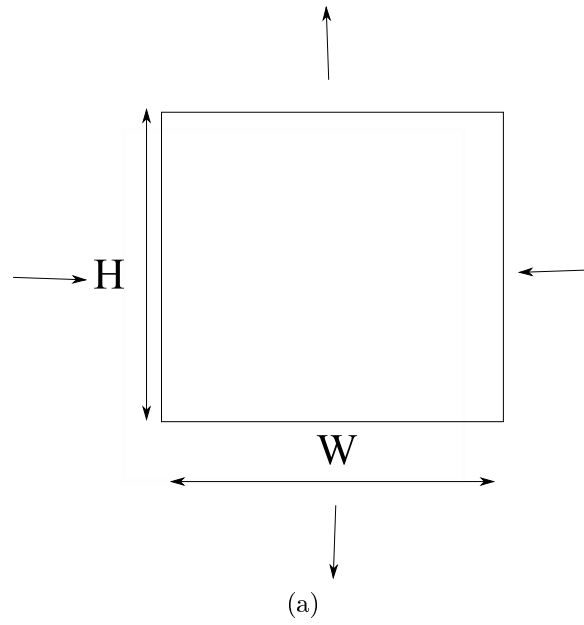


Figure 3.12: (a) Distortion correction. (b) Diffraction pattern with distortion. (c) Diffraction pattern corrected for distortion.

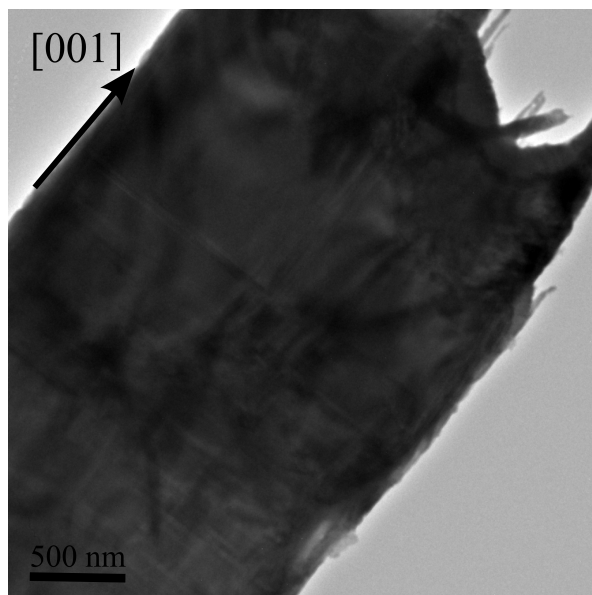
3.2.4 π - Inversion Calibration of a Consistent Frame of Reference

It is important to consistently and unambiguously specify the frame of reference for the orientation maps. Without the knowledge of the reference system with respect to which the crystal orientations are specified, it is only possible to determine the relative orientation of a grain with respect to another grain in an orientation map, while the orientation of a crystal with respect to a fixed sample reference is ambiguous. Therefore, only the grain boundary misorientations can be determined while it is not possible to determine any information about the orientation of the grain boundary planes.

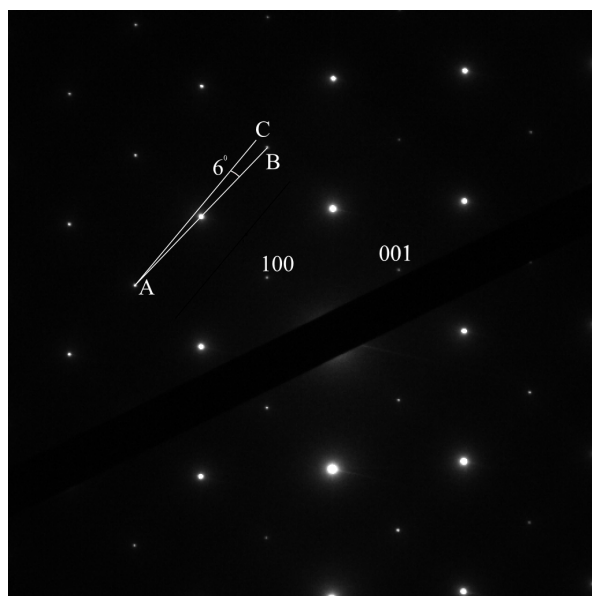
In ACOMTM, the positive x direction is given by the scan direction and the direction parallel to the optic axis of the microscope is taken as the z direction, where the direction from the sample to the gun is taken to be positive direction. The y direction is chosen to obtain a right handed orthogonal coordinate system. However, it should be noted that the crystal orientation is determined from the diffraction pattern and in a TEM the diffraction pattern is rotated with respect to the image about the optic axis. Therefore, to unambiguously specify the frame of reference it necessary to calibrate the image rotation with respect to the diffraction pattern and the orientation of the scanning direction.

To calibrate the image rotation with respect to the diffraction pattern for the JEOL 2010F TEM, a specimen of α -MoO₃ was used. Details of this calibration procedure is discussed in the literature [98]. α -MoO₃ is an orthorhombic crystal and forms asymmetric thin platelets with length along the

[001] direction. Fig. 3.13(a) shows the bright field image of an α -MoO₃ crystal. The diffraction pattern from the same crystal is shown in Fig. 3.13(b), with the 100 and 001 reflections identified. The angle between the [001] directions in the image and the diffraction pattern is nearly 6°. To resolve the 180° ambiguity arising due to the symmetry of the diffraction pattern in Fig. 3.13(b), a defocused diffraction pattern was collected [98]. Comparison of the bright field image in Fig. 3.14(a) and the defocused diffraction pattern in Fig. 3.14(b) shows that a rotation of 186° in the counter-clockwise direction of the diffraction pattern is needed to make it coincide with the diffraction pattern.

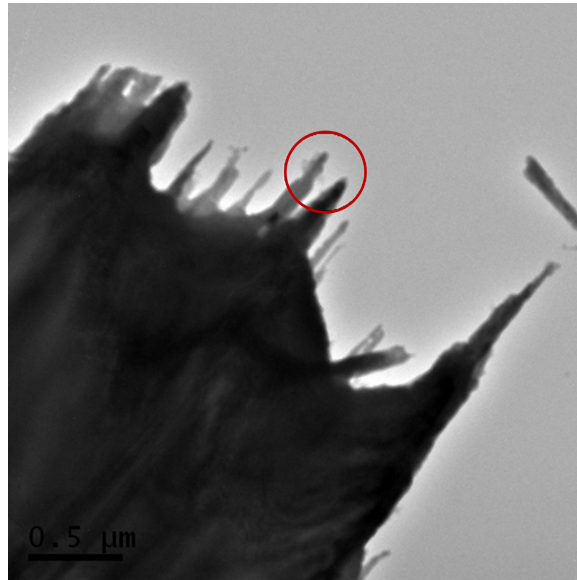


(a)

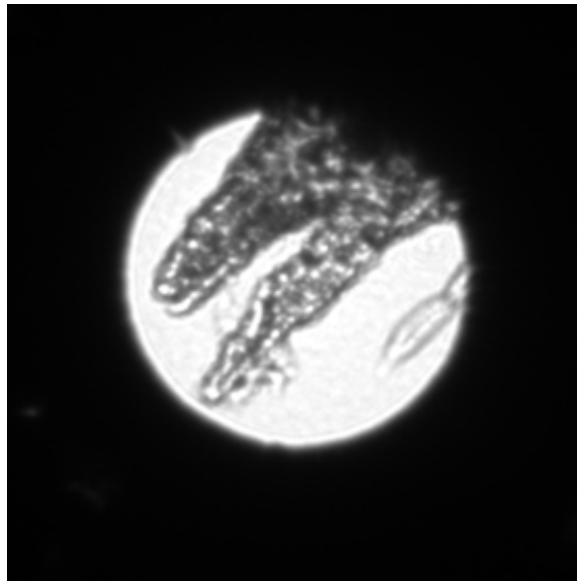


(b)

Figure 3.13: (a) Bright field image of an α - MoO_3 crystal and (b) diffraction pattern from the same crystal.

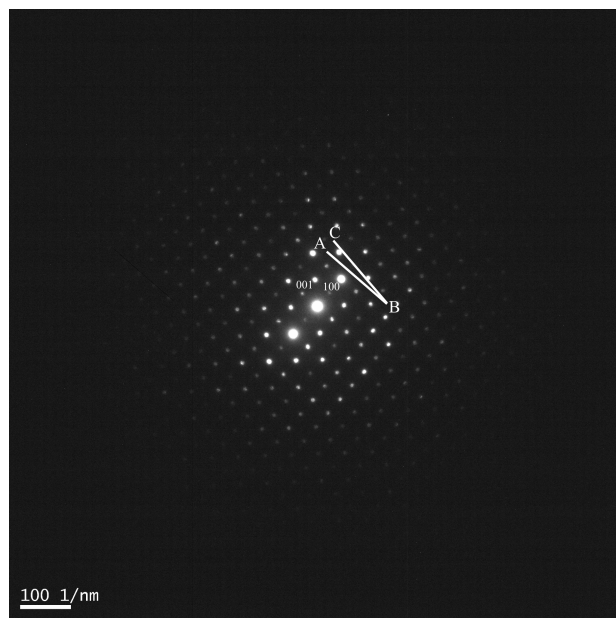


(a)

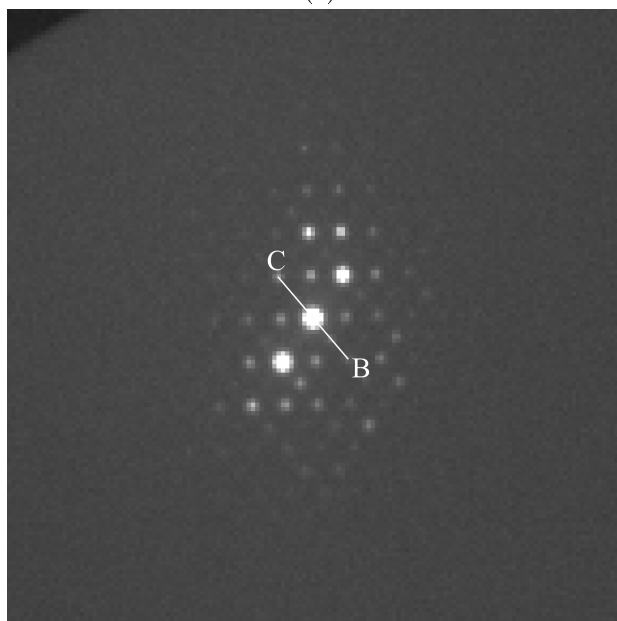


(b)

Figure 3.14: (a) Bright field image of an α - MoO_3 crystal and (b) defocused diffraction pattern from the same crystal shows that there is a 180° inversion between the bright field image and the diffraction pattern.



(a)



(b)

Figure 3.15: (a) Diffraction pattern collected from an α - MoO_3 crystal from the CCD camera and (b) the same diffraction pattern collected using the optical camera.

It should be noted that the diffraction pattern shown in Fig. 3.13(b) for the purpose of calibration was collected using the Gatan CCD (Charge-Coupled Device) camera installed on the microscope, instead of the optical camera that is used in the ASTARTM system. It is important to note that the diffraction pattern collected using the optical camera is always distorted and therefore, should not be used for the purpose of calibration. The [001] in Fig. 3.15(b) (BC) is rotated by approximately 10° with respect to the [001] in Fig. 3.15(a) (AB)

As mentioned earlier, the direction of scanning is considered as the x direction. Therefore, it is necessary to have a reference to specify the orientation of the scan direction. For this purpose, the scanning direction, from left to right, that coincides with the horizontal direction in the image is considered as the reference orientation, which was also set as the default scan direction (Fig. 3.16). For a scanning direction oriented at an angle Θ with respect to the reference direction, an active rotation of $186^\circ + \Theta$ about the z direction in counter-clockwise direction on the diffraction pattern is required to make the diffraction pattern into coincidence with respect to the image.

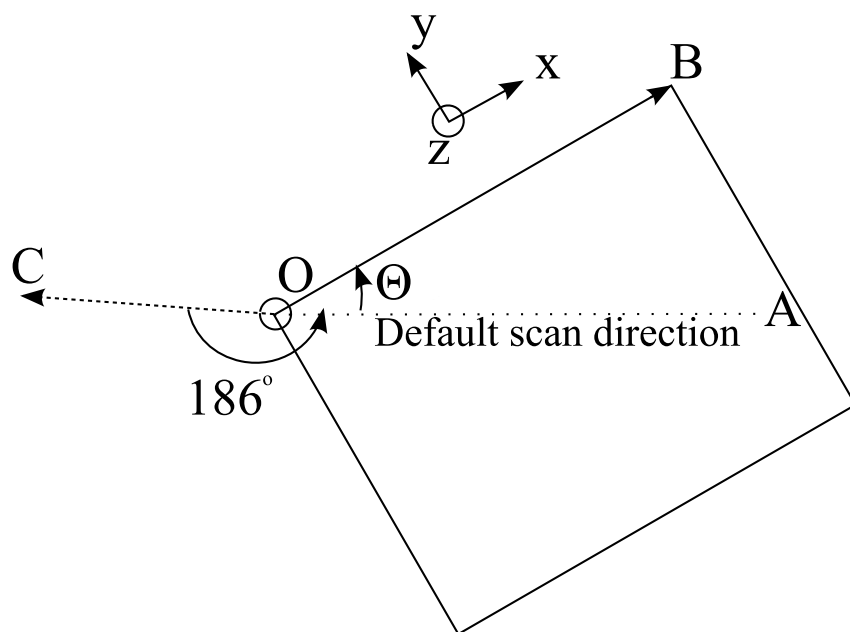


Figure 3.16: The coordinate system for the orientation maps with respect to the scanning direction. OC is the orientation of the reference direction in the diffraction pattern.

3.2.5 Relation between TSLTM and ASTARTM Frames of Reference

The orientation maps generated by ASTARTM contains 3D orientation information of each pixel in the microstructure and is expressed in terms of Euler angles. However, for subsequent analysis, the TSLTM OIM data analysis software developed by EDAXTM was used. Therefore, the orientation data from ASTARTM was first exported to a *.ang* file format. However, before analysis of the exported data, it is important to have a consistent definition of the frames of reference for TSLTM data analysis software and ASTARTM. According to the notation used in TSLTM OIM data analysis, the x axis is denoted as the Rolling Direction (RD), the y axis is denoted as the Transverse Direction (TD) and the z axis is denoted as the Normal Direction (ND). Fig. 3.17 shows the presence of a 90° rotation between the reference systems. The [111] pole figure from a point in the orientation map from a Cu thin film in the frame of reference used in ASTARTM is shown in the figure. The [111] pole figure from the same point plotted using the TSLTM OIM data analysis software is shown. The difference in the two pole figures is due to the fact that definitions of the reference systems for TSLTM OIM data analysis and ASTARTM are different and this is taken not into account when the data from ASTARTM is exported to TSLTM OIM data analysis. This can be corrected by applying a rotation of 90° in the counter-clockwise direction about ND to the frame of reference used in TSLTM OIM data analysis. The pole figure in Fig. 3.17 after this correction is also shown.

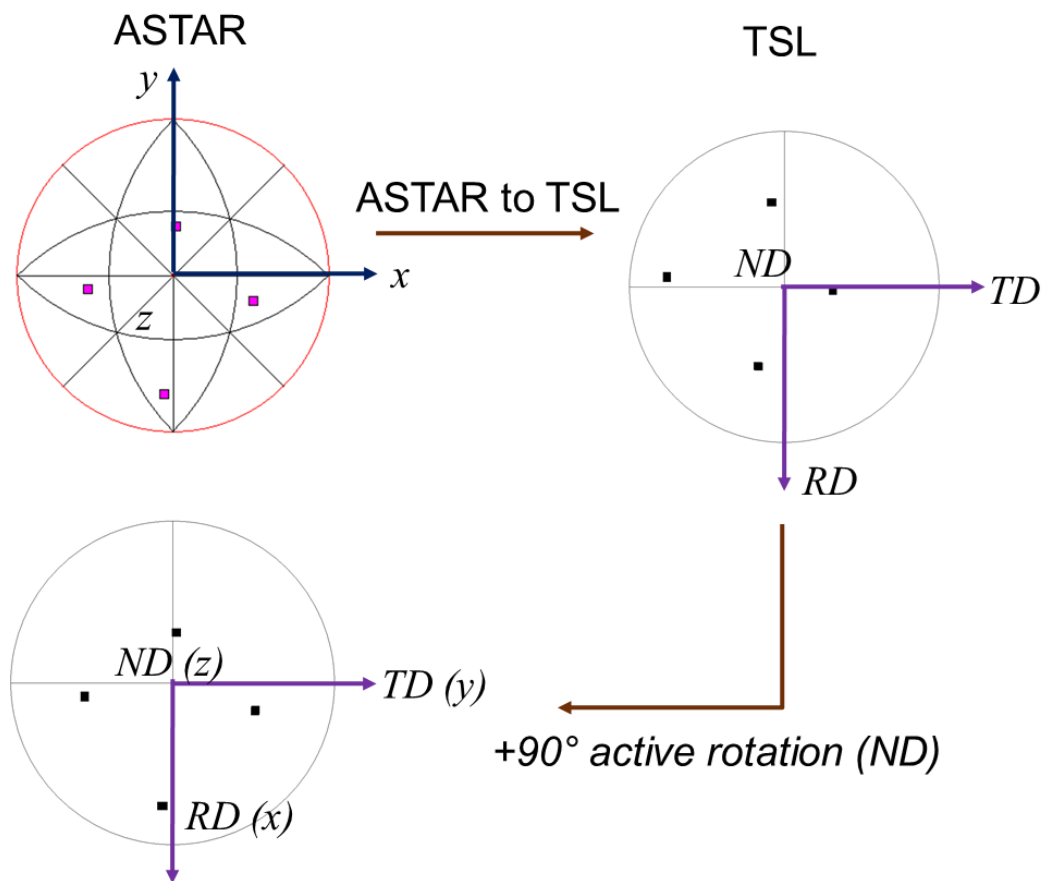


Figure 3.17: Comparison of the reference system used in ASTARTM and TSLTM OIM data analysis.

3.2.6 Finite Element Analysis for Local Stresses in Cu Interconnects using OOF2

As previously discussed in section 2.3.2, stress induced voiding in Cu interconnects depends upon three factors, namely, the source of vacancies, driving force (stress gradients) and mass transport. Amongst these factors, stress gradients and mass transport are dependent on the interconnect microstructure. Therefore, to correlate the local hydrostatic stresses and stress gradients with the experimentally determined interconnect grain structure, a microstructural FEM approach was employed using the Object Oriented Finite Element (OOF2TM) package developed by the National Institute of Standards and Technology (NIST). Unlike conventional FEM packages, OOF2TM recognizes that crystalline materials are composed of grains, and allows for the input of individual crystal orientations. In this way, the stress simulations for Cu interconnects can account for the elastic anisotropy of Cu (Eq. 2.12) instead of assuming an average elastic modulus for Cu. It must be noted that the OOF2TM can be used to perform 2D simulations. Although Cu interconnect lines are 3D structures, the stress simulations at this scale could provide critical insight into the local stress gradients in the microstructure.

Initially, the orientation map of the Cu interconnects obtained by electron microscopy was used to identify the individual grains. The orientation information was extracted from each grain in the microstructure in the form of Euler Angles. Subsequently, grains with the same orientation were color coded in the Adobe PhotoshopTM software. The color coded image was used as the

model microstructure for FEM analysis (Fig. 3.18(a)). In the FEM model, the dielectric surrounding the Cu was also assigned a unique color. The pixel color groups thus created were used by the OOF2TM program to identify individual grains. Subsequently, the color coded grains and dielectric layers were assigned the corresponding mechanical properties and orientation information. The assigned mechanical properties of Cu and the dielectric material are shown in Tables 3.2 and 3.3. The influence of the thin Ta diffusion barrier ($\sim 10\text{-}15$ nm) was neglected in the simulation.

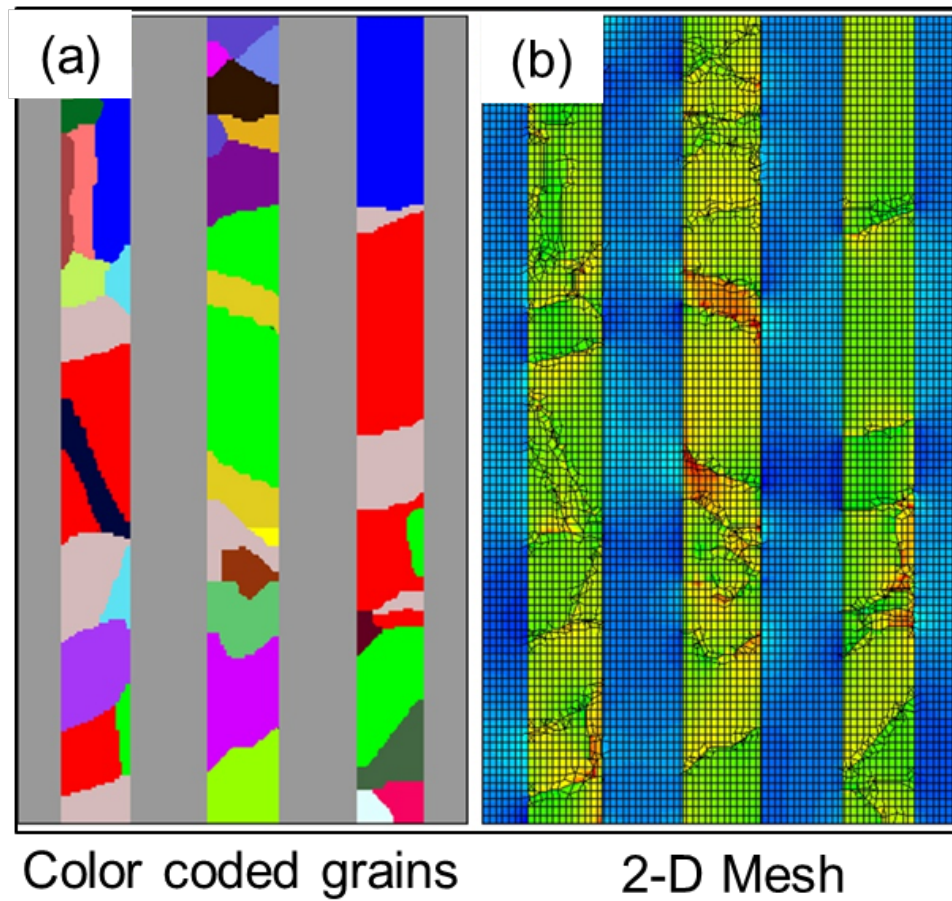


Figure 3.18: (a) Color coded FEM model containing orientation parameters for each Cu grain (b) 2D mesh solved to obtain the stress solution

	Stiffness coefficient of Cu (GPa)
c_{1111}	168
c_{1122}	121
c_{2323}	75

Table 3.2: Stiffness coefficients for Cu [112]

Material	Young's modulus (GPa)	Poisson's ratio
SiO ₂	72	0.2

Table 3.3: Mechanical properties of the dielectric [112]

After the creation of the model, and assignment of the material properties, displacement boundary conditions were applied in the x (along the interconnect length) and y (along the interconnect width) directions. The displacements along the length and width of the line were indirectly obtained from the average stress and strain values along these directions experimentally determined by Gan et al. [73] using XRD. The local hydrostatic stresses in the Cu microstructure were computed at room temperature. After including the relevant boundary conditions, a mesh was generated. Initially, a coarse mesh consisting of quadrilaterals was generated. Subsequently, it was refined to include triangular elements especially close to grain boundaries and interfaces. The final mesh was well refined to map the overall microstructure model within computational limitations (Fig. 3.18(b)). After meshing, the software was instructed to solve for the force balance equation represented by

$$-\nabla \cdot \sigma = P \quad (3.3)$$

where σ is the stress and P is the total body force per unit volume. It must be noted that the stress tensor is expressed as a product of the stiffness tensor and the strain tensor. However, since the stiffness constants for Cu are along the regular laboratory coordinate system, they were transformed into the crystal coordinate system for the individual Cu grains using a transformation matrix generated by the Euler angle representation of the individual Cu grains. This transformation can be mathematically represented as

$$c_{ijkl} = \sum_{m=1}^6 \sum_{n=1}^6 \sum_{o=1}^6 \sum_{p=1}^6 \alpha_{im} \alpha_{jn} \alpha_{ko} \alpha_{lp} c_{mnop} \quad (3.4)$$

where α is the direction cosine matrix, c_{mnop} is the stiffness tensor and c_{ijkl} is the transformed stiffness tensor. Finally, after solving the differential equation, hydrostatic stress contours were plotted.

Chapter 4

Results and Discussions

4.1 Orientation Determination by D-STEM

The D-STEM technique was used to obtain orientation information from individual nanoparticles from a cluster. The bright-field STEM image in Fig. 4.1(a), taken under D-STEM conditions, depicts an agglomerate of silver nanoparticles. To obtain the diffraction pattern from a single particle in the agglomerate, the D-STEM probe was positioned on particle P1 (~ 4 nm in size). Figure 4.1(b) shows the spot diffraction pattern from particle P1. Regular indexing procedure revealed that the orientation of particle P1 was near the $[112]$ zone axis (Fig. 4.1(b)). In another experiment carried out to demonstrate the spatial resolution of the D-STEM technique, diffraction information was obtained from an individual particle of cubic BN in an ensemble of monodispersed BN particles. A bright field STEM image of the particles shown in Figure 4.1(c). The dark particle P2 was specifically chosen for diffraction analysis because dark features in a bright field image are under strong diffracting conditions for the given incident beam direction. This condition is essential to obtain proper zone axis patterns. The spot diffraction pattern obtained from P2 measuring ~ 3 nm in size indicates a $[001]$ zone axis orientation of the particle (Fig. 4.1(d)). Thus, the acquired diffraction

patterns from both the particles clearly demonstrate that despite the high particle density, it is possible to obtain crisp and easily indexable spot diffraction patterns from individual nanoparticles up to 3 nm in size using D-STEM.

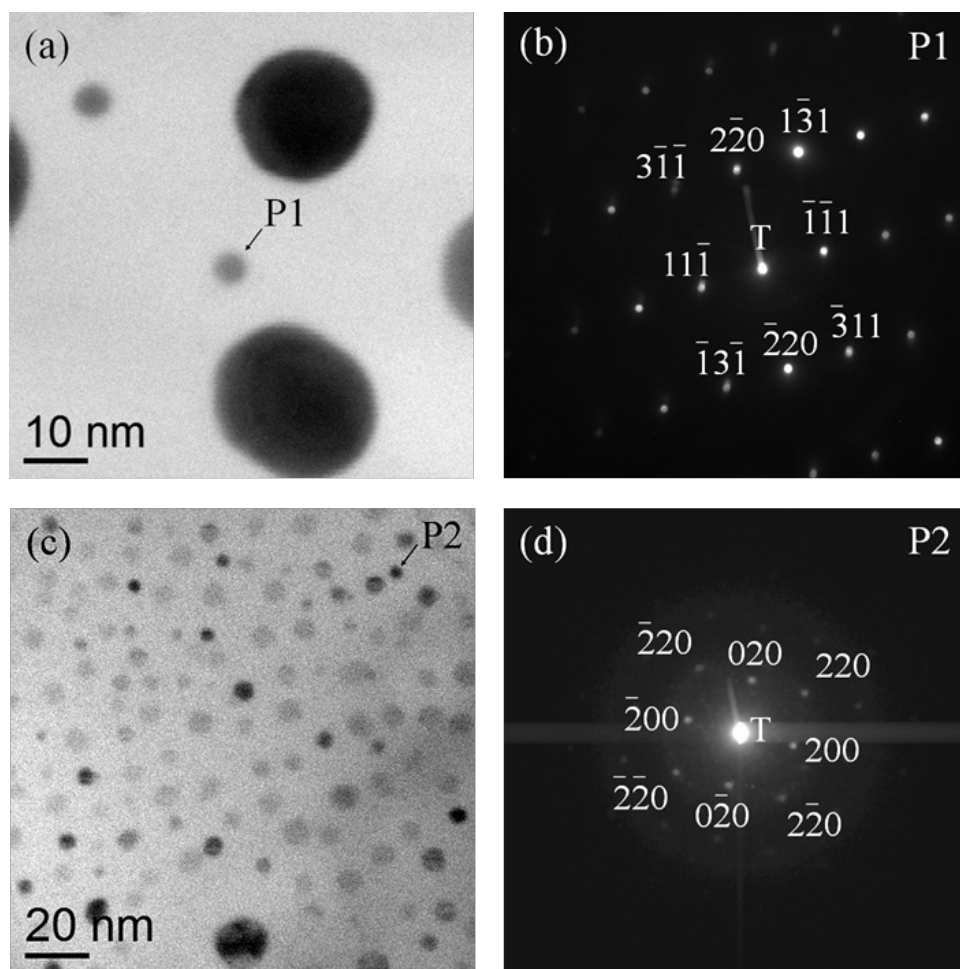


Figure 4.1: (a) Bright-field STEM image of Ag nanoparticles (b) diffraction pattern from P1 (~ 4 nm in size) along the $[112]$ beam direction; (c) bright-field STEM image of boron nitride nanoparticles (d) diffraction pattern from P2 (~ 3 nm in size) along the $[001]$ beam direction.

4.2 Automated Orientation Determination in Cu Interconnects using D-STEM and STEM Diffraction Imaging

Although using the D-STEM technique, it was possible to accurately position the electron probe at nanostructure of interest in the STEM image and obtain sharp spot diffraction patterns, the process was still manual. In order to acquire orientation information from hundreds of grains in a polycrystalline sample, it was deemed essential to develop a technique to automate the pattern acquisition process. Therefore, the D-STEM technique was coupled with spectral imaging using the Gatan STEM Diffraction ImagingTM software. The combination of the two techniques enabled the automated acquisition of diffraction patterns by performing line or area scans on the polycrystalline sample. This process is similar to the conventional line and area scans in EDS or EELS analysis, with each pixel in the data set being mapped with a diffraction pattern. In addition to pattern acquisition, indexing of hundreds of diffraction patterns obtained is extremely tedious and time consuming. Therefore, the indexing software called Automated Crystallography for TEM (ACT) was used to index the obtained diffraction patterns. This technique was employed to obtain local orientation information in 120 nm wide Cu interconnects.

Fig. 4.2(a) shows a bright field STEM image of periodic 120 nm wide Cu interconnects. A line scan was performed across the grains labeled 1-10 in the image such that at each spatial position (user defined step size), diffraction patterns were collected and stored before the probe translated to the next pixel

location. Four of the representative spot diffraction patterns obtained from grains labeled 1, 3, 4 and 6 are shown in Fig. 4.2(b-e).

The obtained diffraction patterns were indexed in ACT using a pattern matching cross correlation algorithm given in Eq. 3.1. The results are generated in the form $(hkl)[uvw]$ where (hkl) represents the zone axis while $[uvw]$ depicts the reciprocal space vector parallel to the transverse direction (TD) of the diffraction pattern as shown in Fig. 4.2(b-e). Except for grains 1, 7 and 9, all other grains seemed to exhibit a $\{110\}$ or a near $\{110\}$ normal texture. After rotation calibration of the diffraction pattern with respect to the STEM image, it was found that grains with $\{110\}$ normal texture were oriented with the $\langle 112 \rangle$ and $\langle 111 \rangle$ directions aligned along the length and width of the CI line, respectively [113]. Previous results of grain orientations in wide Cu lines have shown the presence of Cu grains with a $\{111\}$ normal texture. However, the texture observed in the current work can be attributed to the sidewall growth of $\{111\}$ grains in narrow Cu lines, as evidenced by Besser et al. [26] as well.

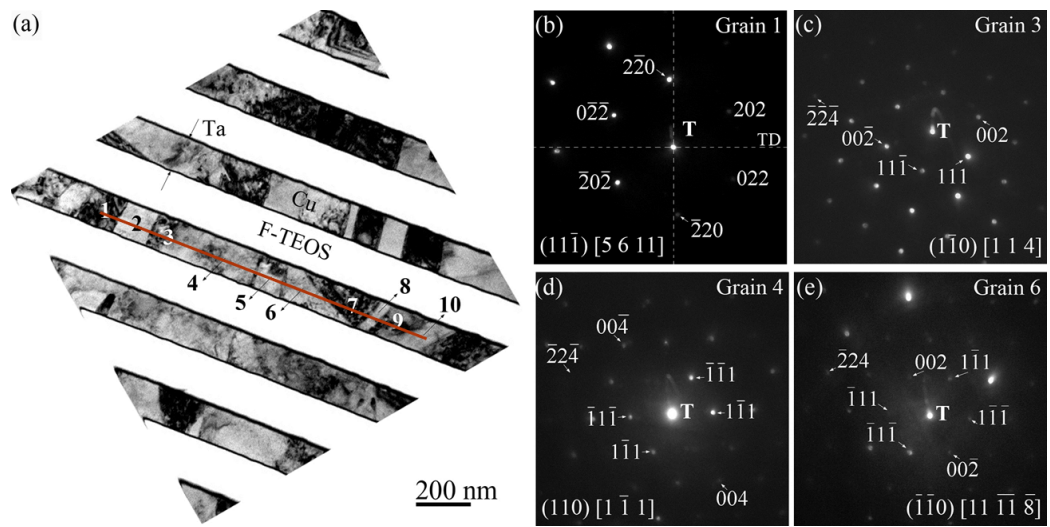


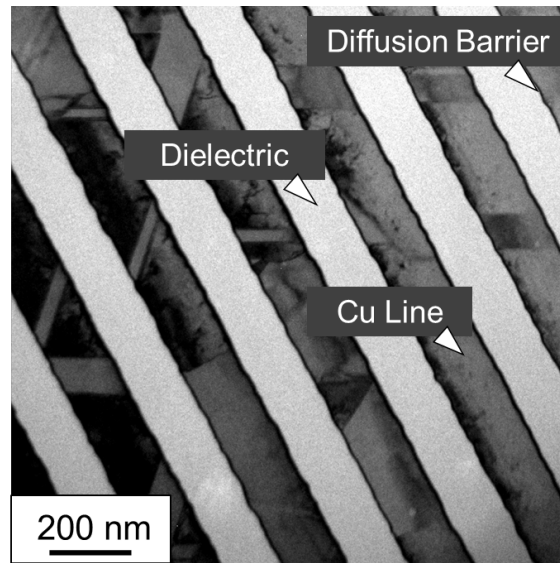
Figure 4.2: (a) Bright field STEM image of 120 nm wide Cu interconnect lines showing grain labeled 1-10. (b) Representative diffraction patterns obtained from grains labeled 1, 3, 4 and 6 [113]

4.3 High Resolution Orientation Mapping in Copper Interconnects ($1.8\ \mu\text{m}$ - $70\ \text{nm}$ in width) using D-STEM and Precession Electron Diffraction

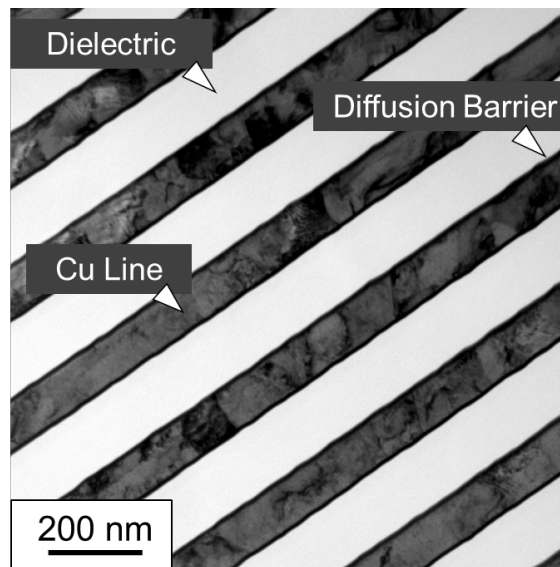
The D-STEM technique combined with spectral imaging and ACT enables automated acquisition and indexing of diffraction patterns from numerous grains in the Cu interconnect structure. However, as previously mentioned, some grains may be oriented far off a prominent zone axis, resulting in a near two-beam condition or systematic row of reflections (Fig. 3.4). In such cases, it is nearly impossible to index the crystal orientation accurately without significant specimen tilts in the microscope. This severely limits automation of the pattern acquisition process, making it difficult to obtain statistically significant orientation data from nano Cu interconnects. In order to address this issue, a high resolution orientation mapping technique was developed by coupling the D-STEM technique with precession electron diffraction. Using this technique, microstructure evolution in downscaling Cu interconnects was comprehensively investigated.

Figs. 4.3(a-b) show representative bright field TEM images of two sets of periodic Cu interconnect lines, 180 nm and 120 nm in width respectively. The bright field images show strong diffraction contrast from defects such as dislocations. However, these defects mask the contrast from grain boundaries, thereby making it very difficult to identify the grain structure or grain size in these lines. Identifying all of grains by TEM imaging would again require a series of tedious specimen tilts. These examples also clearly show that conven-

tional NBD and SAD techniques are unsuitable and impractical for obtaining rapid and reliable orientation data from individual Cu grains.



(a)



(b)

Figure 4.3: Bright field TEM images of periodic Cu lines (a) 180 nm wide (b) 120 nm wide

4.3.1 Texture and Grain Boundary Analysis: 1.8 μm wide Cu lines

Plan-view microstructure observations on 1.8 μm wide periodic damascene Cu interconnect lines showed the presence of large micron-sized grains with significant twins. A representative color coded inverse pole figure map overlaid with the reconstructed grain boundaries is shown in Fig. 4.4. The colors in the map depict normal orientations consistent with the color-coded standard stereographic triangle. In the standard triangle, the principal directions namely, $[001]$, $[101]$ and $[111]$ are colored in red, green and blue respectively.

For quantitative and statistical analysis of texture and grain boundary distribution in the 1.8 μm wide lines, four different sets of samples were analyzed. As a standard notation in the thesis, RD and TD refer to the directions along the length and width of the interconnect while ND refers to the out-of plane normal direction (along trench normal). The schematic in Fig. 4.5 illustrates these directions clearly with respect to the Cu trench. Fig. 4.6 shows the collective inverse pole plots obtained from these samples. The textures in the inverse pole plots are quantified and color coded to indicate the frequency of occurrence of a particular texture. The numbers adjacent to each of the colors are the ODFs (refer to section 2.4.1), and are expressed in units of multiples of random distribution. The plots revealed a strong $\langle 111 \rangle$ fiber texture // ND with a mixed $\langle 110 \rangle$ and $\langle 112 \rangle$ texture along the line length (RD). This observation is consistent with the fact that crystallographically, with the $\langle 111 \rangle$ texture // ND, the directions in the $\langle 111 \rangle$ zone are favored along RD, and these lie along the great circle connecting $\langle 110 \rangle$ and $\langle 112 \rangle$.

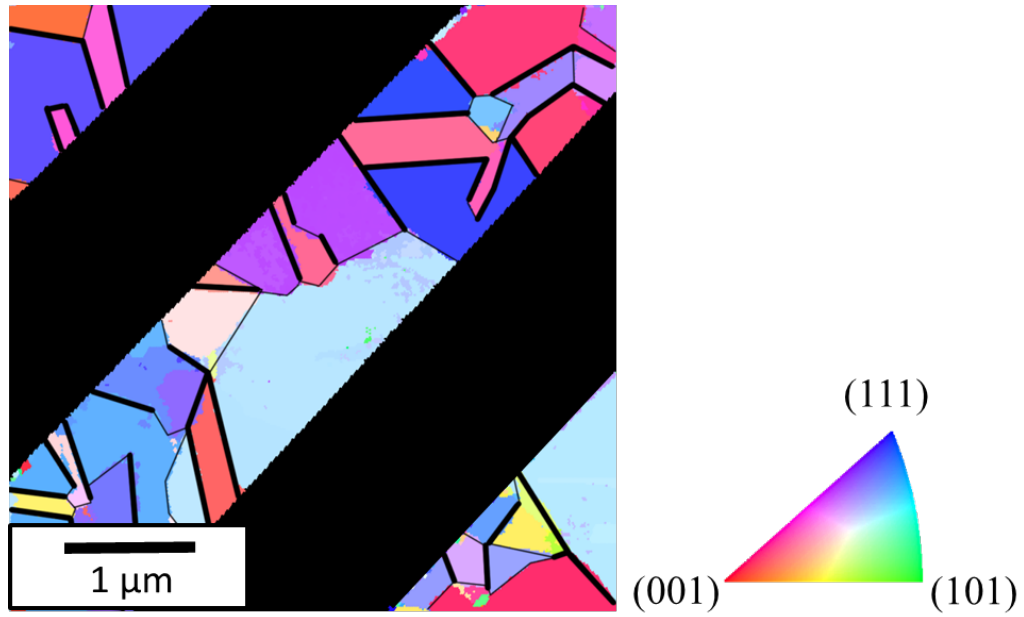


Figure 4.4: Color coded inverse pole figure map from $1.8\ \mu\text{m}$ wide Cu lines. Color codes for orientations are represented in the standard stereographic triangle.

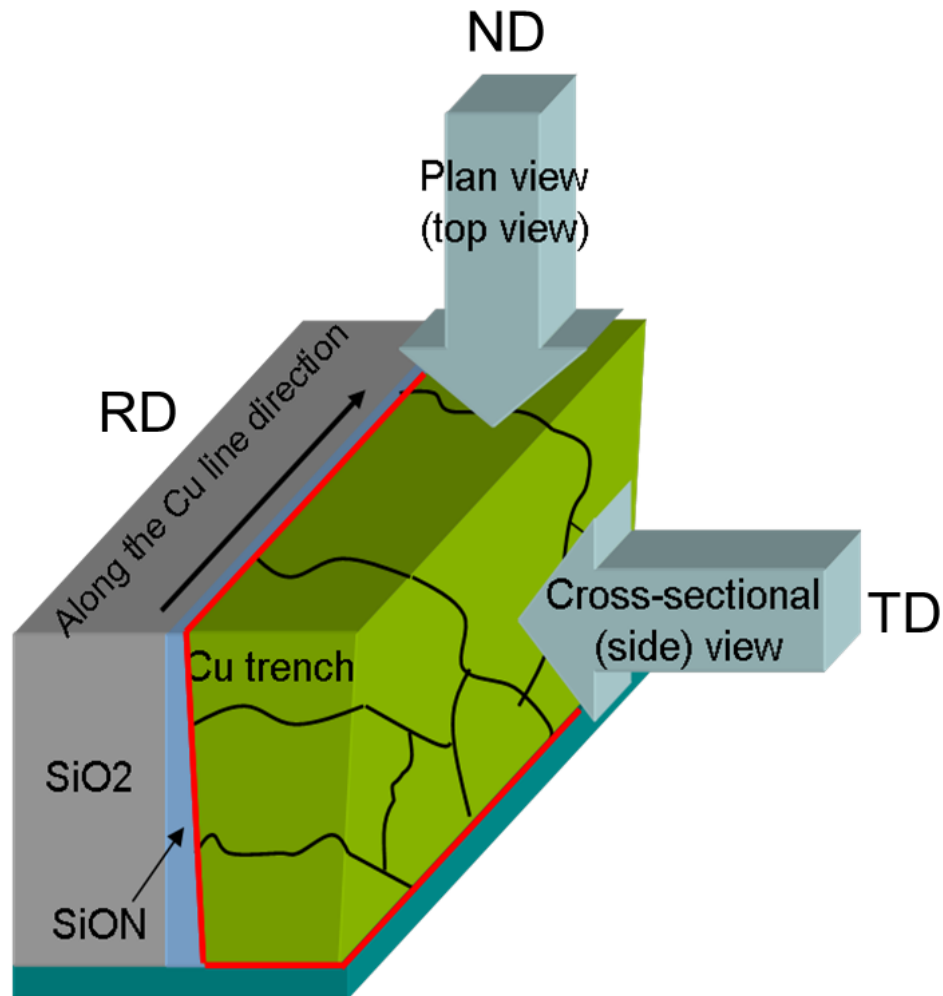


Figure 4.5: Schematic illustrating ND, RD and TD directions with respect to the Cu trench

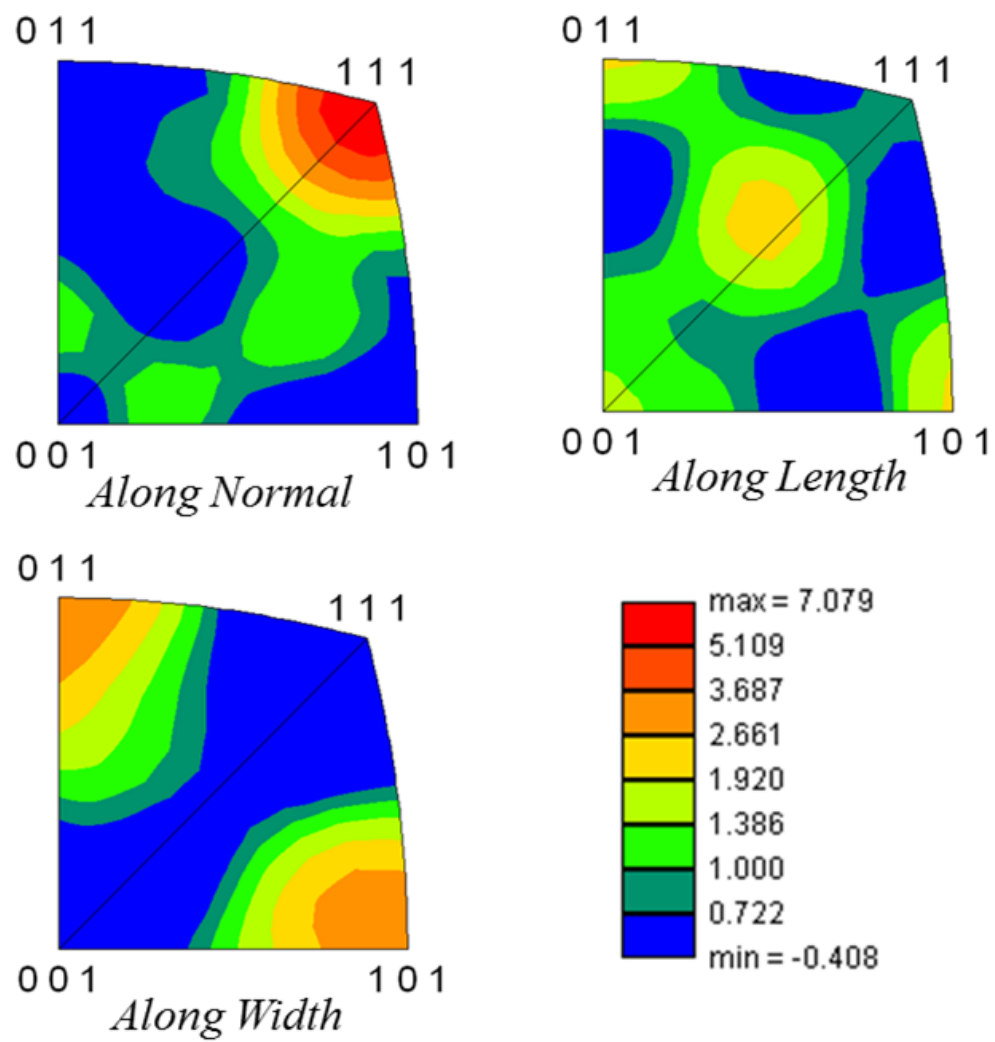


Figure 4.6: Inverse pole plots along the Cu trench normal (ND), length (RD) and width (TD)

The orientation data collected was also used to quantify the fraction of $\Sigma 3^n$ ($n = 1, 2, 3$) type and non-CSL high angle boundaries. As mentioned previously in section 2.4.2, $\Sigma 3$ boundaries in Cu are of particular interest due to their frequent occurrence. However, the special properties associated with $\Sigma 3$ boundaries such as low energy, low diffusivity and low mobility are valid only when their grain boundary plane is of a $\{111\}$ type. Such boundaries are coherent $\Sigma 3$ boundaries, also known as coherent twin boundaries. $\Sigma 3$ boundaries with any other boundary plane are incoherent and can be treated as regular high angle boundaries. The higher order $\Sigma 3$ boundaries also have other grain boundary planes for coherency, namely the $\{110\}$ and $\{001\}$ type. To determine the fraction of coherent $\Sigma 3$ boundaries, grain boundary trace analysis was performed.

In trace analysis, to determine whether a $\Sigma 3$ twin boundary is coherent, the trace of the grain boundary plane is matched with the trace of the $\{111\}$ plane in both the crystals on either side of the boundary [114]. If the boundary trace and the $\{111\}$ traces are within a pre-defined tolerance, then the twin boundary is considered to be coherent. In this thesis, the tolerances for coherency have been set according to Brandon's criterion with a tolerance of 8.7° for the misorientation and 10° for the trace deviation [115]. However, it should be noted that the matching between the trace of the boundary plane and the $\{111\}$ is a necessary but not a sufficient condition for a twin boundary to be coherent. This is because the trace of the boundary plane matches the trace of all the planes whose normals are perpendicular to the boundary line

segment. Therefore, when a boundary is classified as a coherent boundary it is ambiguous and the true fraction of coherent twin boundaries is always less than or equal to the estimate from trace analysis.

Analysis of grain boundary misorientations from a data set of 8000 boundaries in 1.8 μm lines revealed that the fraction of $\Sigma 3$ type boundaries was about 42% (length fraction). Among these, more than 98% (by length) were coherent in nature. In Fig. 4.4, the boundaries marked with thick lines are coherent $\Sigma 3$ boundaries while those marked by thin lines are non-CSL high angle boundaries. The total length fraction of $\Sigma 9$ and $\Sigma 27$ boundaries was about 6% while that of other CSL boundaries was negligible. Low angle boundaries categorized by the Brandon criterion [31] accounted for about 5% of the total boundary length. These results are consistent with EBSD and XRD measurements carried out on 1.8 μm lines by Besser et al. [26] and Cho et al. [116].

4.3.2 Texture and Grain Boundary Analysis: 180 nm wide Cu lines

Comprehensive characterization of texture and grain boundary distribution was performed on 180 nm wide periodic Cu interconnect lines. A representative color coded inverse pole figure map overlaid with the reconstructed grain boundaries is shown in Fig. 4.7. The colors in the map, consistent with the color coded standard stereographic triangle, depict the normal orientations of the grains. The grain structure these lines was different from that of the 1.8 μm wide lines and was observed to be near-bamboo. By definition, a bamboo

grain structure is one in which individual grains traverse the width of the line and the grain boundaries are perpendicular to the line itself. In a near-bamboo grain structure, one or more grains span the width of the line and majority of the grain boundaries are nearly perpendicular to the line [117].

Quantitative texture analysis for these lines was performed using a consolidated set of raw orientation data from 5 separate samples in order to obtain statistically meaningful texture plots. Inverse pole plots shown in Fig. 4.8 reveal a prominent biaxial texture of $\{111\}\langle 110\rangle$ ($\langle 110\rangle$ // RD and $\langle 111\rangle$ // ND). Analysis of the grain boundary misorientations and traces in these lines performed from a data set of 10000 boundaries revealed that the length fraction of the $\Sigma 3$ boundaries reduced to 25% when compared with 42% for 1.8 μm . Among all of the $\Sigma 3$ boundaries present, 97% were coherent in nature. The coherent $\Sigma 3$ boundaries are marked by thick dark lines in Fig. 4.7. Higher order $\Sigma 3$ boundaries and low angle boundaries, each constituted about 4% (by length) of the total boundary distribution. Neglecting the minor fraction of other CSL boundaries, the remaining grain boundaries were non-CSL high angle boundaries.

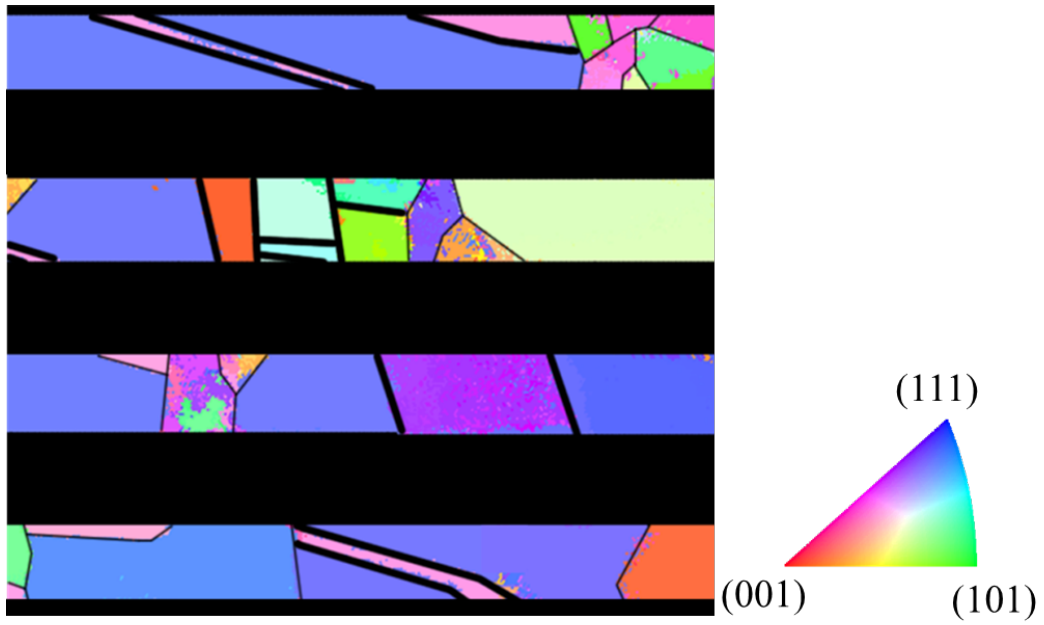


Figure 4.7: Color coded inverse pole figure map from 180 nm wide Cu lines. Color codes for orientations are represented by the standard stereographic triangle

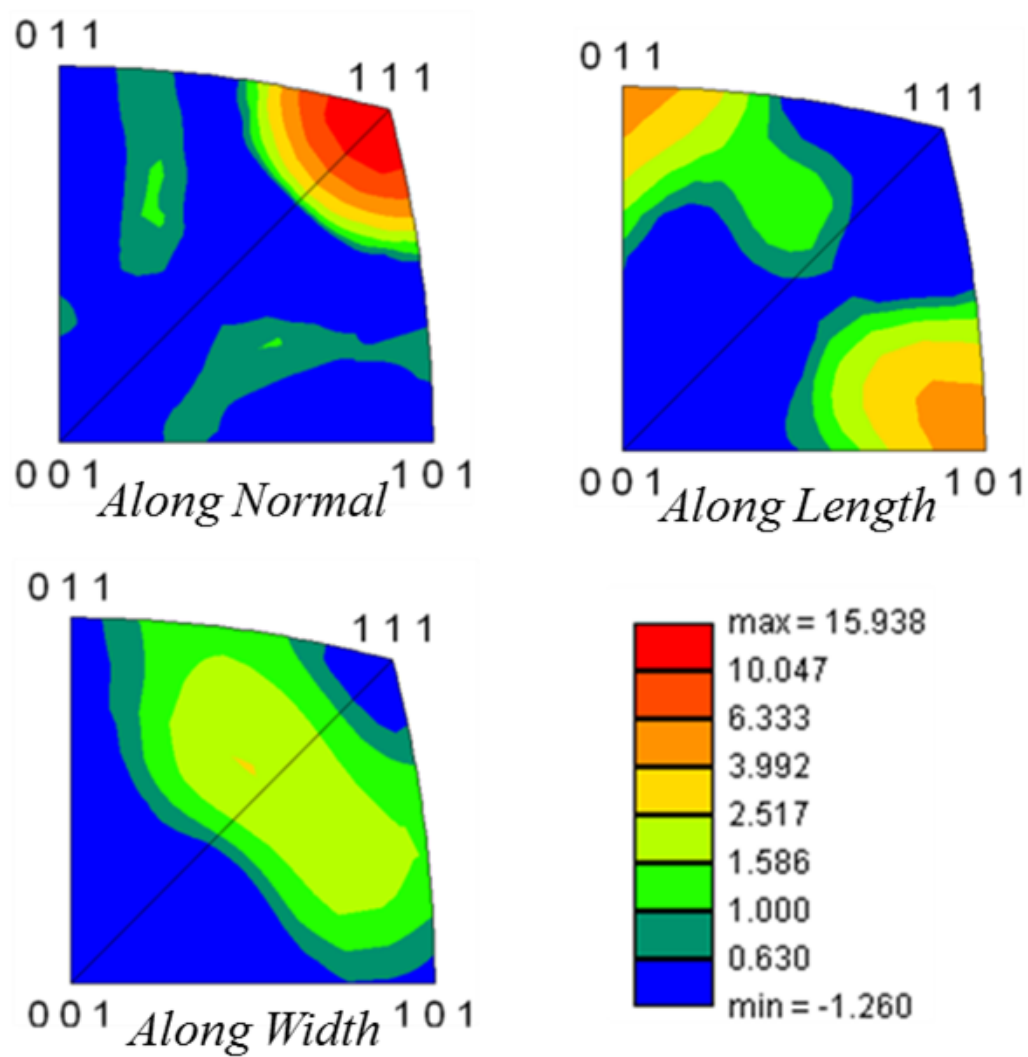


Figure 4.8: Inverse pole plots along the Cu trench normal (ND), length (RD) and width (TD)

4.3.3 Texture and Grain Boundary Analysis: 120 nm wide Cu lines

Similar microstructure analysis as mentioned in the previous two sections was carried out for periodically spaced 120 nm wide Cu interconnects. A representative color coded orientation map overlaid with a reconstructed grain boundary map is shown in Fig. 4.9 along with the standard color coded stereographic triangle. The thick dark boundaries in the orientation map are the coherent $\Sigma 3$ boundaries. The grain orientations in these lines were found to be significantly different from that of the previously analyzed wider line structures. The 120 nm wide lines exhibited no normal texture and instead, revealed a slight $\langle 111 \rangle$ texture // RD as shown in Fig. 4.10. This can be attributed to sidewall growth of the $\{111\}$ grains in narrow Cu lines, as also observed by Besser et al. [26] Grain boundary characterization also revealed that the length fraction of $\Sigma 3$ boundaries decreased further to 18%, measured from a data set of 10000 boundaries. The coherent twin boundaries comprised more than 95% (by length) of all the $\Sigma 3$ boundaries present. The higher order $\Sigma 3$ boundaries and low angle boundaries each accounted for less than 5% of the grain total boundary length.

A closer examination of the microstructure (magnified region in Fig. 4.9) revealed a bamboo or near-bamboo grain structure in few regions. However, clusters of small grains were also observed in the vicinity of large bamboo grains. Such a change in the microstructure of Cu lines with a reduction in line width is similar to earlier observations on Al interconnects [118]. Grain boundary misorientation and trace analysis performed near such cluster/bamboo

segments revealed that almost all of the small grains were separated by non-CSL high angle boundaries. The implications of such a microstructure will be discussed in the later sections of the thesis.

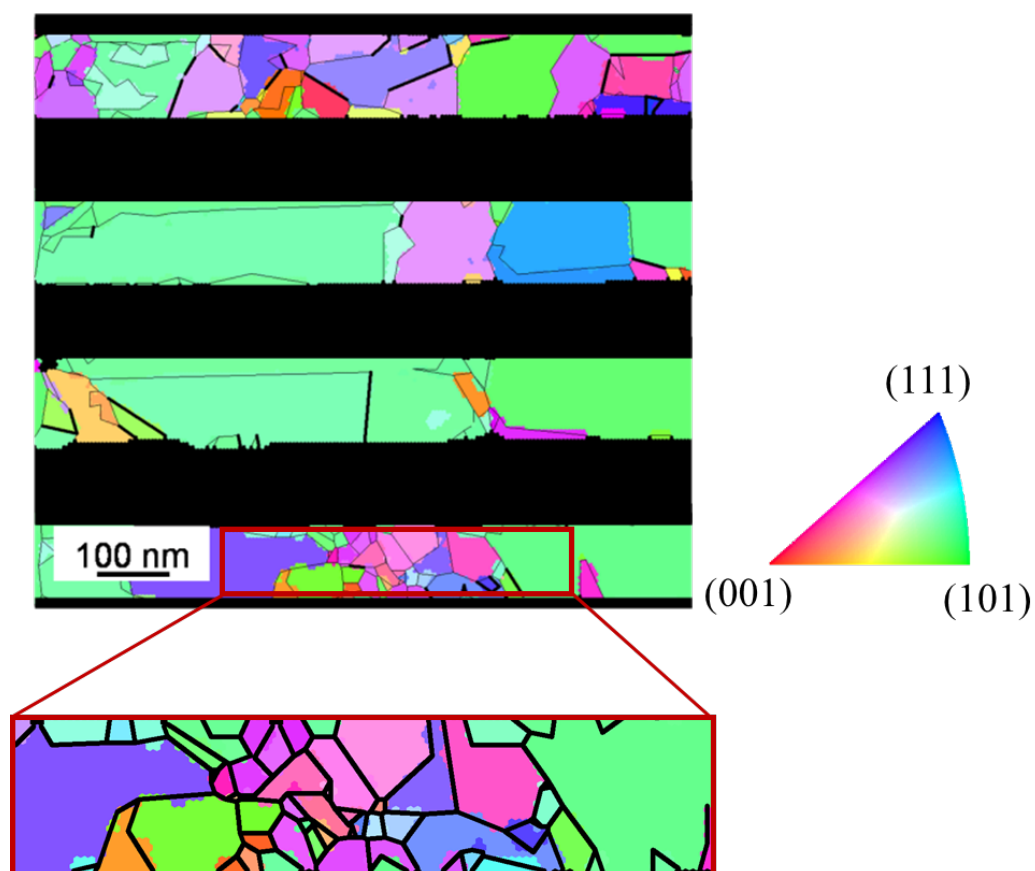


Figure 4.9: Color coded inverse pole figure map from 120 nm wide Cu lines. Color codes for orientations are represented by the standard stereographic triangle

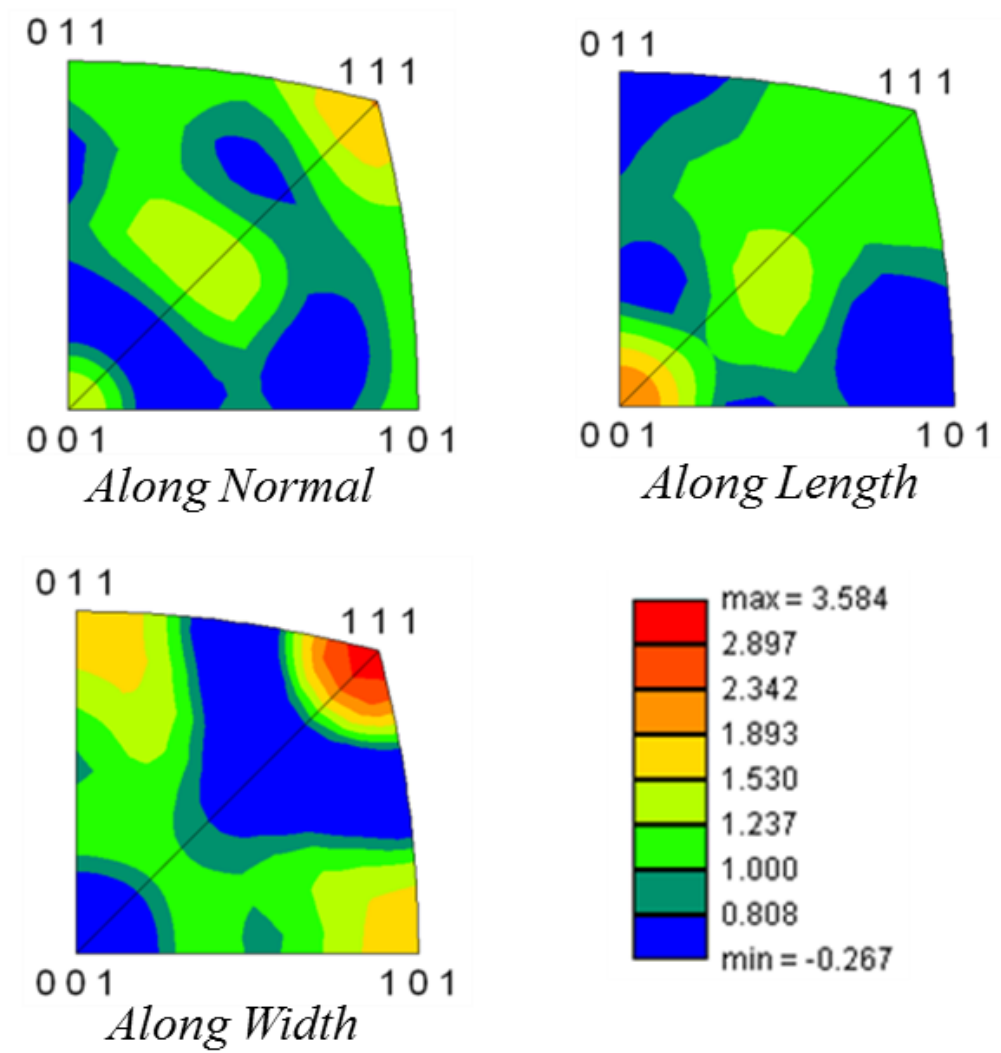


Figure 4.10: Inverse pole plots along the Cu trench normal (ND), length (RD) and width (TD)

4.3.4 Texture and Grain Boundary Analysis: 70 nm wide Cu lines

To further investigate the effect of interconnect downscaling on the microstructure, 70 nm wide Cu lines (45 nm node technology) were analyzed. In contrast to the 180 nm and 120 nm lines, the microstructure of the 70 nm Cu interconnects was polygranular, as revealed in Fig. 4.11. By definition, a polygranular microstructure is one in which there are continuous grain boundary paths along the length of the interconnect [119]. The crystallographic texture of these lines analyzed by consolidating orientation data from multiple samples was also found to be drastically different from the wider Cu lines. A dominant sidewall $\langle 111 \rangle$ texture with a strong brass component $\{110\} \langle 112 \rangle$ was observed, indicating strong preference for sidewall $\{111\}$ growth (Fig. 4.12). In texture terminology, it is assumed that the fiber is aligned along the normal direction (ND). Therefore, a brass-component refers to $\langle 110 \rangle$ texture // ND with the $\langle 112 \rangle$ // RD.

In terms of grain boundary distribution in 70 nm wide lines, the length fraction of coherent $\Sigma 3$ boundaries (revealed by thick dark lines in Fig. 4.11) further reduced in comparison with wider lines to 14%. The length fraction of other CSL boundaries was less than 2% while low angle boundaries constituted less than 5% of the total boundary length. Since Cu interconnects (< 120 nm in width) were expected to show a dominant sidewall texture, transverse cross section analysis of the structure was also performed. Orientation maps overlaid with the reconstructed grain boundary maps for the same are shown in Fig. 4.13. The results revealed the presence of large clusters of small equiaxed

grains at the bottom of the trench (highlighted by red ellipse in Fig. 4.13), while larger grains were found to be closer to the top of the trench. Analysis of the grain boundaries in the small grain regions revealed that almost all the small grains were separated by high angle boundaries.

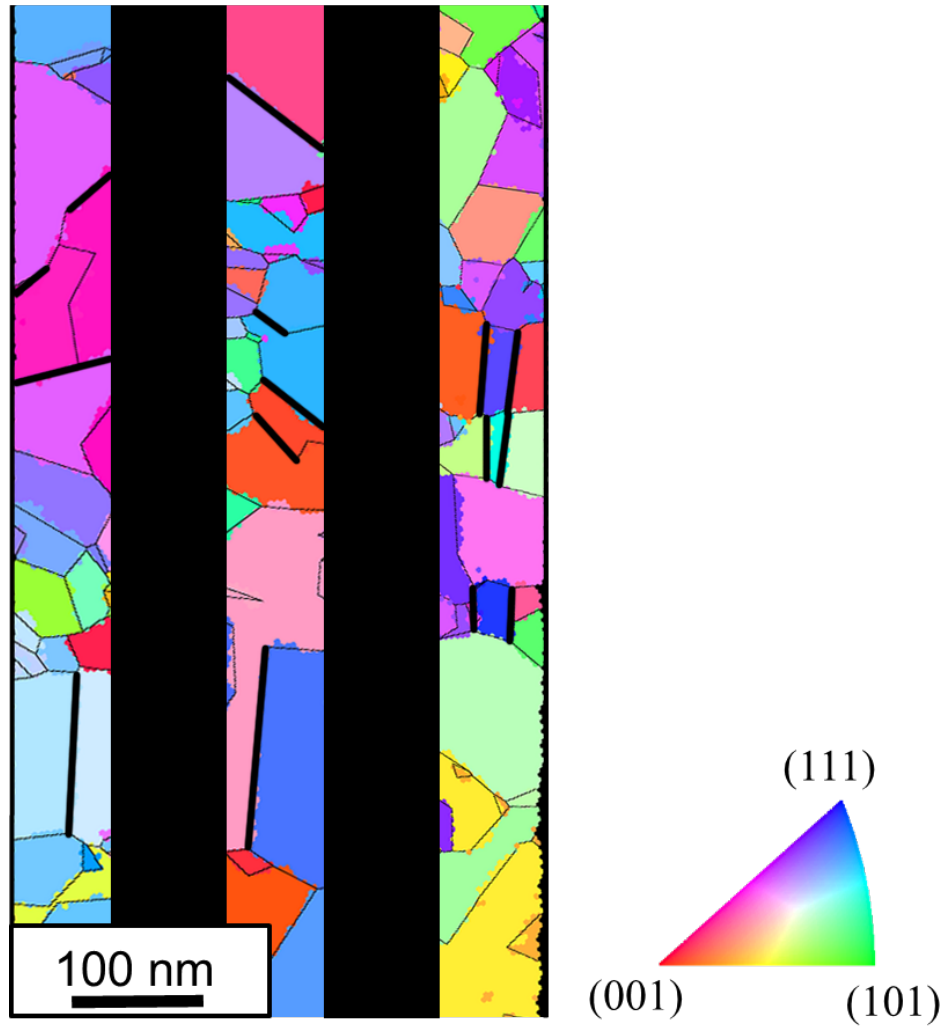


Figure 4.11: Color coded inverse pole figure map from 120 nm wide Cu lines. Color codes for orientations are represented by the standard stereographic triangle

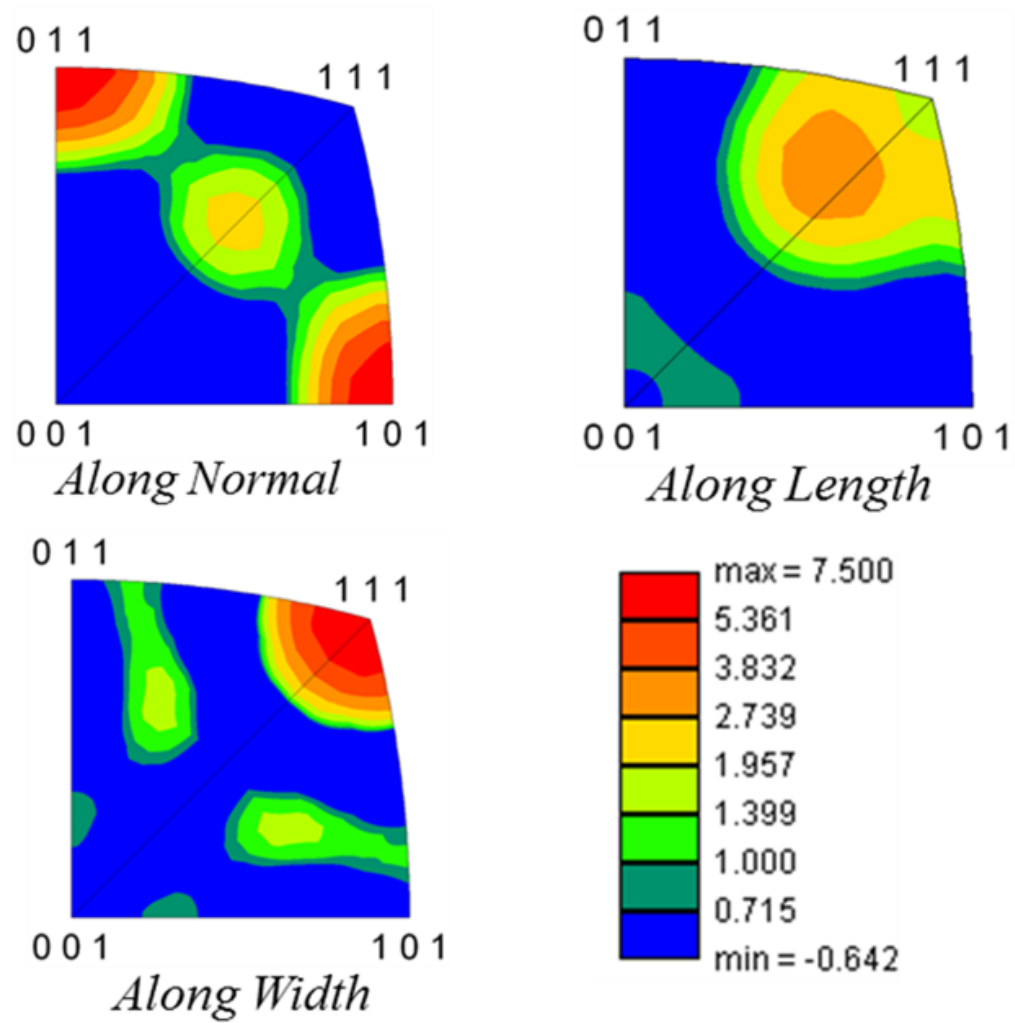


Figure 4.12: Inverse pole plots along the Cu trench normal (ND), length (RD) and width (TD)

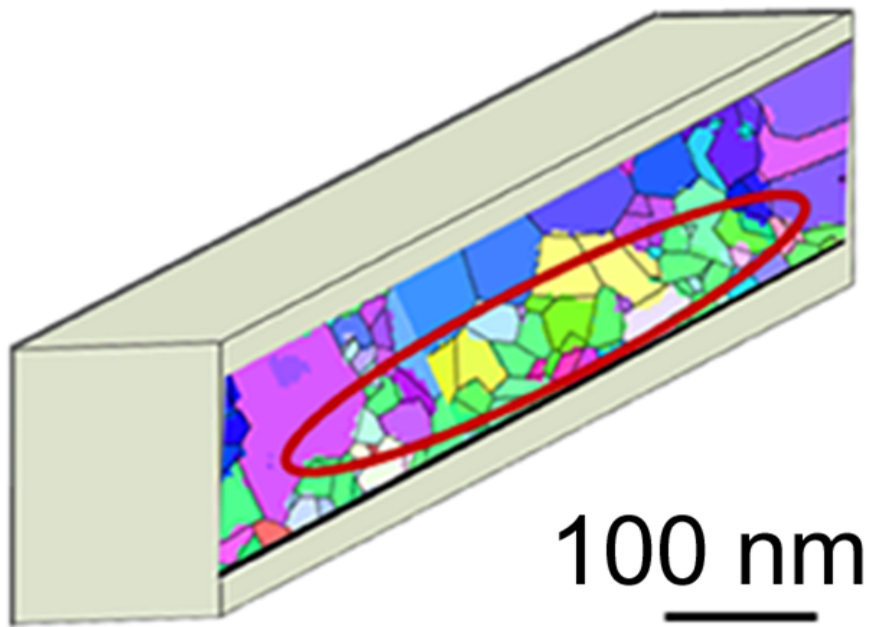


Figure 4.13: Orientation map in cross section showing clusters of small grains at the trench bottom (highlighted by the red ellipse)

4.4 Effect of Downscaling on the Microstructure of Cu Interconnects

Based on the aforementioned results, as the interconnect width is reduced from 1.8 μm to 120 nm, the $\langle 111 \rangle$ //ND fiber texture becomes weaker. In fact, 120 nm CI lines exhibit no normal texture, but show a slight preference for orientations where the $\{111\}$ planes are parallel to the sidewalls, as first noted by Besser et al [26]. Such a texture becomes more severe in 70 nm wide lines, which can be attributed to dominant sidewall grain growth [26]. In addition to this effect, the 70 nm wide Cu lines have a strong preference for orientations where the $\langle 112 \rangle$ directions are along the line length, as also observed by Budiman et al. [120].

In addition to variations in texture, the downscaling of Cu interconnects also results in changes to grain boundary characteristics and the overall grains structure. The length fraction of coherent $\Sigma 3$ boundaries has been found to decrease with reducing line widths from 42% in case of 1.8 μm wide lines to 14% in case of 70 nm wide lines. Correspondingly, there seems to be an increase in the percentage of high angle boundaries in the interconnect structure with reducing line width. There is also a drastic change in the overall microstructure in the lines. Wider lines seem to comprise a near-bamboo type grain structure whereas narrower lines tend to have a grain structure composed of clusters of small equiaxed grains near large grains. Most of the small grains have been found to be separated by high angle boundaries.

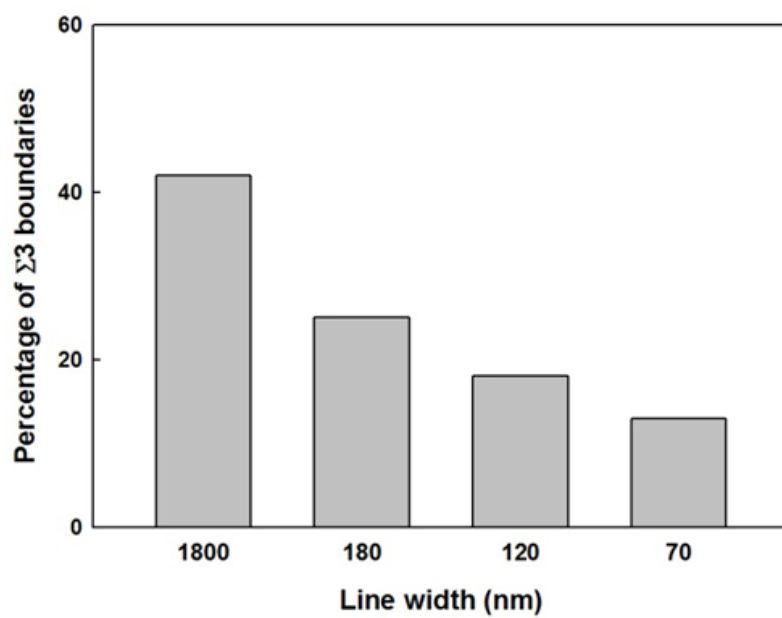


Figure 4.14: Variation of the percentage of $\Sigma 3$ boundaries with Cu interconnect line width

4.5 Factors Affecting Microstructure Evolution in Cu Interconnects

4.5.1 Overall Energy Minimization during Grain Growth

To understand such microstructure variations upon downscaling, it is important to recognize that the Cu interconnect structure is a dimensionally constrained system with multiple interfaces fabricated using complex processing conditions. Therefore, during the Cu annealing process, grain growth is governed by multiple factors, which may be mutually competitive. The classical model assumes that during grain growth, all boundaries move with velocities proportional to the average energy per unit area of the boundary and its average curvature [121]. However, in Cu interconnect structures, the grain growth process is more complex involving the surface energy, interfacial energy and strain energy contributions as well. Mathematically, the effective velocity of the grain boundary during grain growth can be written as

$$v = \mu \left(\kappa + \frac{\Delta\gamma_{s/i}}{h\gamma_{gb}} + \frac{\Delta M \epsilon^2}{\gamma_{gb}} \right) \quad (4.1)$$

where μ is the boundary mobility, κ is the grain boundary curvature, $\Delta\gamma_{s/i}$ is the difference in the sum of the surface and interface energies for grains on either side of the boundary, γ_{gb} is the energy of the grain boundary, ΔM is the difference in biaxial moduli of grains meeting at a boundary and ϵ is the strain. Therefore, the overall driving force for grain growth is dependent on the minimization of the grain boundary energy, surface energy, interfacial energy and the strain energy [121].

4.5.2 Sidewall Interfacial Energy and Surface Energy Contributions

As the interconnects are downscaled, the surface and interface area to volume ratio increases. Thus, the surface and interfacial energy contributions become increasingly important during grain growth. Furthermore, with increasing aspect ratio (Table 1), the area of the trench sidewall interface increases with respect to the trench bottom, which raises the influence exerted by the sidewall on the Cu grain structure. This leads to preferential growth of a sub-population of grains with crystallographically favorable orientations to minimize the sidewall interfacial energy. It also explains the abnormal growth of grains leading to regions of large and small grains in the microstructure. Such an effect had been earlier proposed by Thompson et al. [121] and Harper et al. [122].

To explore the favorable Cu orientations that minimize the total interfacial energy, it is important to recognize that the Ta diffusion barrier in contact with Cu is deposited by the PVD process and is the metastable phase β -Ta with a Tetragonal crystal structure. This has been experimentally confirmed through XRD by Wong et al. [123]. With the β -Ta phase, Cu shares a hetro-epitaxial relationship such that Cu [2-20] on the (111) is parallel to the Ta [330] on the (002) plane [123]. Therefore the growth of {111} Cu minimizes the energy of the Cu/Ta interface. In wider lines with lower aspect ratios, fiber textured grain growth with $\langle 111 \rangle$ along the trench normal minimizes the interfacial energy at the trench bottom. In narrower lines though, the

growth of the $\{111\}$ grains growing perpendicular to the trench sidewall is favors minimization of sidewall interfacial energy.

From a surface energy standpoint, for typical *fcc* metals such as Cu, the $\{111\}$ surface energy (γ_{111}) is the lowest, with the ordering generally being $\gamma_{\{111\}} < \gamma_{\{100\}} < \gamma_{110}$ for low miller index planes [124]. This has been shown by a simple unsatisfied surface bond analysis as well [125]. Considering the case for the Cu interconnect trenches that have the bottom surface and sidewalls (with a Ta barrier) at 90° to each other, multiple scenarios can be derived for the combined minimization of surface energy and interfacial energy. From an energetics perspective, the ideal scenario for the same would be a $\{111\}/\{111\}$ type. However, crystallographically it is impossible to have two $\{111\}$ planes perpendicular to each other. With the crystallographic limitations, the best grain orientation would be a $\{111\}/\{110\}$ type. Therefore, the grains growing with $\langle 111 \rangle$ oriented along the trench normal would tend to align $\langle 110 \rangle$ along the trench sidewall to minimize both the surface and interfacial energy. This is consistent with our observations in wider lines. Similarly, the $\{111\}$ grains growing normal to the trench sidewalls would have the $\{110\}$ planes perpendicular to the trench normal. This is also consistent with the observed texture in narrow lines.

4.5.3 Effect of the Overburden Layer

In wide lines (250 nm in width and above), it has been observed previously that during annealing, the grain growth process initiates in the over-

burden layer and propagates into the damascene trenches [126]. Therefore, the texture of the Cu grains in the trench is shown to be strongly dependent on the overburden. In some cases, almost complete invasion of the trench by the overburden has been observed, while in the other cases, twin boundaries have been shown to form where the invading grains from the overburden intersect the $\{111\}$ grains growing bottom-up along the trench normal [30, 6]. However, in narrow lines, the invasion of the overburden layer into the trench is restricted by the growth of sidewall $\{111\}$ grains. The resulting microstructure is thus composed of clusters of small grains in the vicinity of some large grains. This phenomenon becomes more severe with reducing line width, thereby resulting in a polygranular structure as observed in 70 nm wide lines. In addition to these factors, in narrow lines, due to mutually perpendicular growth directions, the $\{111\}$ grains growing bottom-up are restricted by the sidewall $\{111\}$ grains. With increasing interface area to volume ratio, preserving both the configurations is important to minimize the overall interfacial energy. However, due to the increasing dominance of the trench sidewall at higher aspect ratios, and under the constraint that no two $\langle 111 \rangle$ directions in Cu can be perpendicular, clusters of small nearly equiaxed grains growing bottom-up remain trapped at the trench bottom.

Thus, in narrow Cu interconnects, the thermodynamically driven grain growth phenomenon is constrained by kinetics involving growth of sidewall, bottom-up and overburden grains. Subject to the aforementioned constraints, although the system tries to attain a grain structure with the minimum total

energy, it is composed of local energy minima and metastable states as well. To develop a more comprehensive understanding of the microstructure evolution in narrow Cu lines, grain growth models based on the experimental results obtained need to be developed and studied.

4.5.4 Topological Effects

The observation that small grains present in the interconnect microstructure seem to have nearly equiaxed structures separated by high angle boundaries instead of low energy coherent twin boundaries may be explained by topological effects restricting grain rotations [127]. For the nearly equiaxed grains sharing boundaries with many other grains, specific rotational changes to form specific low energy boundaries cannot occur in isolation since it may raise the total energy of the other system by increasing the energy associated with the other shared grain boundaries. Such reduction in the fraction of $\Sigma 3$ boundaries with more equiaxed grain structure has also been observed and predicted in the past by Gleiter et al. [128], Randle [127] and Pande et al. [129]. Therefore, such small equiaxed grains are mainly found to share high angle boundaries

4.5.5 Effect of Stresses

From 4.1, it is clear that reducing strain energy is important towards minimizing the overall energy of the system. The Cu interconnects fabricated by the inlaid damascene process are also under mechanical stresses arising be-

cause of the difference in thermal expansion between the metallic interconnect and the substrate/dielectric that rigidly confine it, with the magnitude of these stresses being highest along the line length [26, 73]. Therefore, to minimize the elastic strain energy, the Cu grains orient themselves in such a way that the lowest elastic modulus direction is aligned along the maximum stress direction. As Cu has high elastic anisotropy (Eq. 2.12), the elastic modulus is different along different crystallographic directions. From Fig. 2.8, it is clear that the elastic modulus is highest along the $\langle 111 \rangle$ direction ($E_{111} = 192$ GPa) and lowest along the $\langle 100 \rangle$ direction ($E_{100} = 67$ GPa). The elastic modulus along any arbitrary direction $\langle hkl \rangle$ can be computed as

$$\frac{1}{E_{hkl}} = \frac{1}{E_{100}} - 3\left(\frac{1}{E_{\langle 100 \rangle}} - \frac{1}{E_{\langle 111 \rangle}}\right)(\alpha^2\beta^2 + \beta^2\gamma^2 + \gamma^2\alpha^2) \quad (4.2)$$

where α, β, γ are the direction cosines of $\langle hkl \rangle$.

However, crystallographically, $\langle 100 \rangle$ directions cannot not lie on $\{111\}$ planes. Therefore, the $\{111\}$ grains align the two lowest elastic moduli directions present on the $\{111\}$ planes, which are $\langle 112 \rangle$ and $\langle 110 \rangle$ along the directions of maximum principal stresses, namely the length and width of the CI line, to minimize the strain energy. The resulting textures in copper interconnects obtained by minimizing the total energy is consistent with our results. In the specific case of sidewall growth of $\{111\}$ grains, the alignment of the $\langle 112 \rangle$ along the length of the line minimizes the strain energy. At the same time, this configuration results in a $\langle 110 \rangle$ normal texture that minimizes the

surface energy as well.

4.6 Impact of Observed Microstructure on Electromigration and Stress Induced Voiding

4.6.1 Electromigration

It has been well investigated that in Cu interconnects with a bamboo-type microstructure, the mass transport during EM is dominated by diffusion at the Cu/SiCN interface. However, with downscaling lines, as the microstructure becomes more polygranular, the combination of grain boundary diffusion and interfacial diffusion needs to be considered while evaluating EM mass transport [130]. It has been discussed in the previous sections that as the interconnect lines are downscaled, clusters of small grains separated by high angle grain boundaries are observed in the vicinity of large grains (Figs. 4.9 and 4.11). The presence of such small grain clusters increases the number of triple junctions and potential flux divergence sites. The presence of high angle boundaries would also provide fast diffusion paths for mass transport thereby affecting EM reliability. In addition to this, the normal orientation of the Cu grains intersecting the surface would also influence the interfacial diffusivity at the Cu/SiCN interface.

Microstructure Around EM Induced Void

To investigate the effect of the microstructure on EM flux divergence in further detail, the high resolution orientation mapping technique was used to

obtain grain orientations and grain boundary around a voided region in EM test structures. (*This work has been carried out in collaboration with Prof. Ho at the University of Texas at Austin*). The single link EM test structures were capped with low- k , SiCN consisted of a three level interconnect structure with the second level (M2, 72 nm in width, 144 nm in thickness and 200 μm in length) being the test line. Details pertaining to the EM test performed in Prof. Ho's lab are mentioned elsewhere [131]. Cross section TEM observation was employed to investigate the microstructure of the interconnect line after the EM test

An EM induced void was observed at the Cu/SiCN interface. The TEM image of the interconnect line with the void is shown in Fig. 4.15(a). From the TEM image, the grain structure around the void is unclear. However, using the high resolution orientation mapping technique in the TEM, the microstructure around the void was resolved. The color coded inverse pole figure map overlaid with the reconstructed boundary map around the voided region is shown in Fig. 4.15(b). The colors signify the orientations normal to Cu trench. The misorientation parameters of the grains close to the void were individually identified. Among those grains, the misorientation angle between the $\langle 211 \rangle$ and $\langle 301 \rangle$ (Fig. 4.15(b)) oriented grains adjacent to the cathode end of the void was calculated to be 58° about the $\langle 122 \rangle$ misorientation axis. Such high angle boundary can serve as the a diffusion path for EM mass transport. Preliminary analysis was also performed to calculate the flux divergence at each of the triple points labeled A, B and C in Fig 4.15(b), assuming that

before the void nucleated, the grains close to the void extended all the way up to the interface. The inclination of the grain boundaries to the direction of current flow was also accounted for. Details of the calculation are mentioned elsewhere [131]. The calculations revealed that indeed, the maximum flux divergence occurred at the triple point A, where the maximum misorientation was observed.

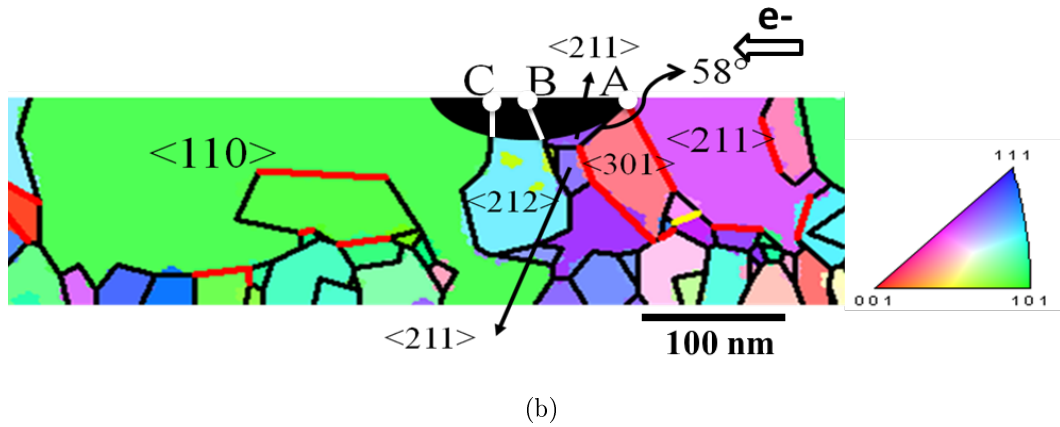
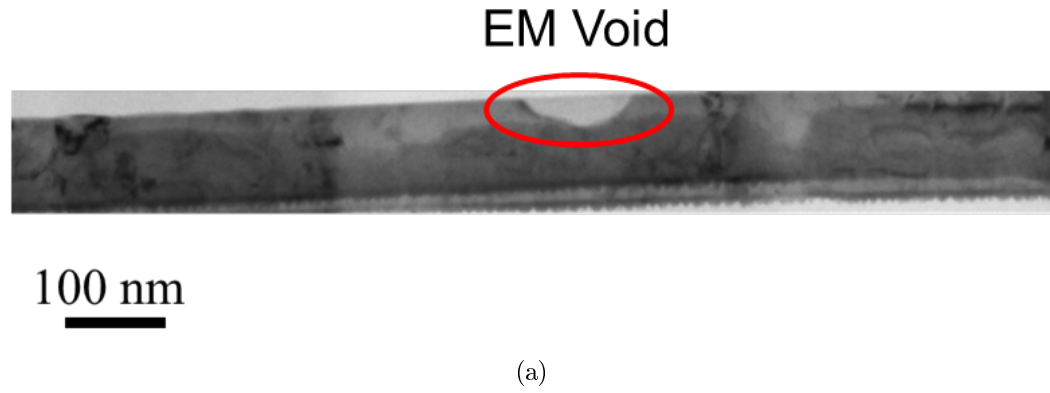


Figure 4.15: (a) Bright field TEM image of the EM test line (b) Color coded inverse pole figure map (orientations along trench normal) of voided region with reconstructed boundaries. Points A, B, C have been assumed to be potential flux divergence sites before the void formation.

Microstructure Under the Via Region

The microstructure of the via (V2) connecting the second and third metal levels (M2 and M3 respectively) in the EM structure was also analyzed using the precessed D-STEM technique. Fig 4.16 shows the color coded inverse pole figure map of the structure in cross section, with the colors representing the orientation of the grains normal to the Cu trench. The grain boundaries marked in red are coherent $\Sigma 3$ boundaries while those marked in yellow are $\Sigma 9$ boundaries. The remaining boundaries in black are non-CSL high angle boundaries. The microstructure of the via seems to be composed of several small grains aggregated near a few large grains. These small grains were found to be separated by high angle boundaries. Some of the large grains in the line M2 and M3 seem to share coherent $\Sigma 3$ boundaries as well. The presence of such small grains separated by high angle boundaries adjacent to a large grain sharing a coherent $\Sigma 3$ boundary can enhance flux divergence to potentially form slit voids at the interface eventually resulting in early EM failure [132].

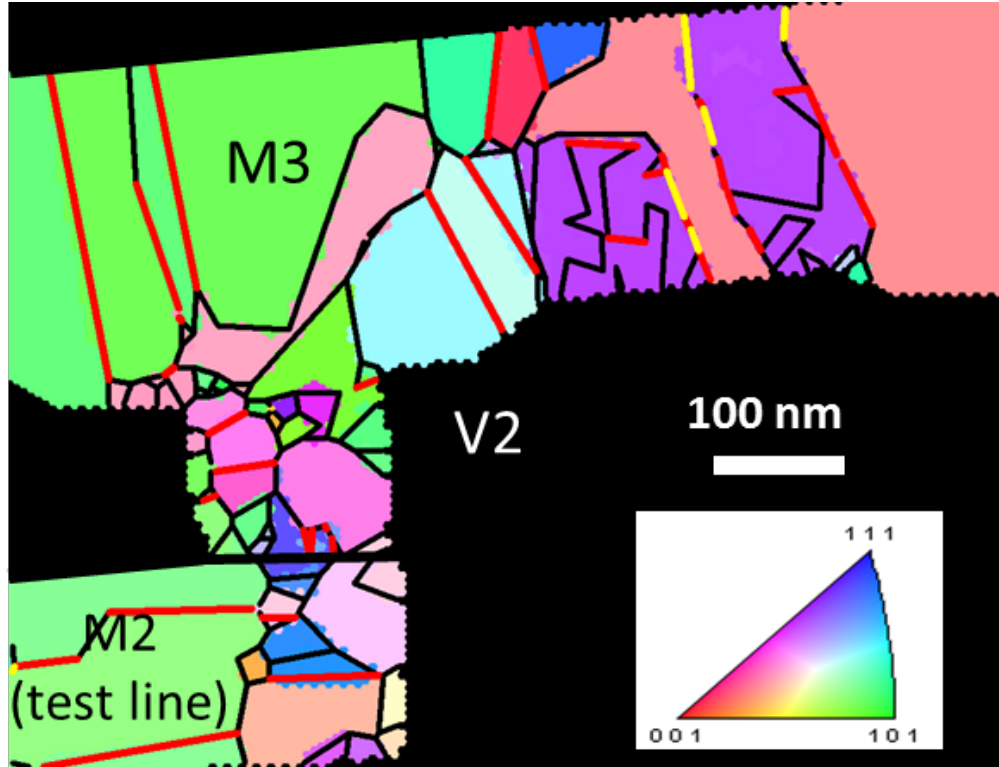


Figure 4.16: Color coded orientation map of the via (V2) connecting M2 and M3. The colors represent grain orientations along the trench normal. Grain boundaries in red are coherent $\Sigma 3$ boundaries while those in yellow are $\Sigma 9$ boundaries.

The aforementioned examples clearly show that the high resolution pre-processed D-STEM technique can be used to obtain quantitative microstructure information that can be employed for flux divergence analysis to correlate the interconnect microstructure with EM reliability. The technique can be used to resolve the microstructure near the via region of narrow dual damascene structures. Thus, the flux divergence calculations performed can also be extended to the via-line region. For more statistical data on the flux divergence sites in via/line structures, the quantitative microstructure information obtained can also be used in conjunction with FEM to generate flux divergence contours.

4.6.2 Stress Induced Voiding OOF2 Simulations for Local Hydrostatic Stresses

The orientation information obtained from the Cu interconnect lines was used to simulate local hydrostatic stresses. Fig. 4.17(a-d) shows the sequence of steps in the simulation along with the results of the 2D stress simulation. The stress simulations clearly show that the hydrostatic stresses are redistributed within the polycrystalline Cu interconnect microstructure according to local misorientation between grains, thereby creating regions of high and low stresses (Fig. 4.17(d)). The highest hydrostatic stress observed at room temperature was 675 MPa. Most of the high stress regions were observed close to the triple junctions where the Cu grain boundaries intersect the barrier interface. Misorientation parameters were also analyzed close to regions of high stresses. Fig. 4.18 shows the misorientation angle/axis pairs

in some of the high stress regions. The results show that high stresses exist between grains separated by a large misorientation. Some of these regions would also include grains separated by a $\Sigma 3$ misorientation. Although such grains are indeed highly misoriented, their special properties arise due to the low diffusivity boundaries separating them, that do not aid vacancy motion.

It is essential to note that the driving force for SIV is the stress gradient ($\nabla\sigma$), but the formation of a stress induced void (assuming there is a vacancy source), would be an interplay between the driving force and available diffusion paths. The corresponding flux divergence for mass transport in SIV can be mathematically represented by

$$Q = \nabla \cdot (-D \nabla \sigma) \quad (4.3)$$

where D is the diffusivity. Thus, in order to completely correlate the microstructure with flux divergence for SIV mass transport, the stress contours obtained by the FEM analysis need to be mapped into stress gradient contours and the corresponding diffusivity values for the interfaces and grain boundaries need to be included. Such simulations would be able account for the special properties of coherent twin boundaries, thereby providing a more realistic understanding of the impact of microstructure on SIV. However, these features are currently not available in the OOF2TM package. Therefore, efforts are underway to build such a model in the very recently launched COMSOL MultiphysicsTM v4.2a FEM program that provides the necessary options to define and include various diffusivity parameters for the microstructure.

For via/line structures as well, where SIV is most probable [22], such analysis for local stress gradients and microstructure dependent flux divergence can be performed. In the case of a via/line microstructure as shown in Fig. 4.16, a microstructure comprising small grains separated by high angle boundaries would provide fast diffusion paths for vacancy motion. Such diffusion paths in the presence of a sufficient vacancy concentration and driving force can be expected to lower the stress migration reliability.

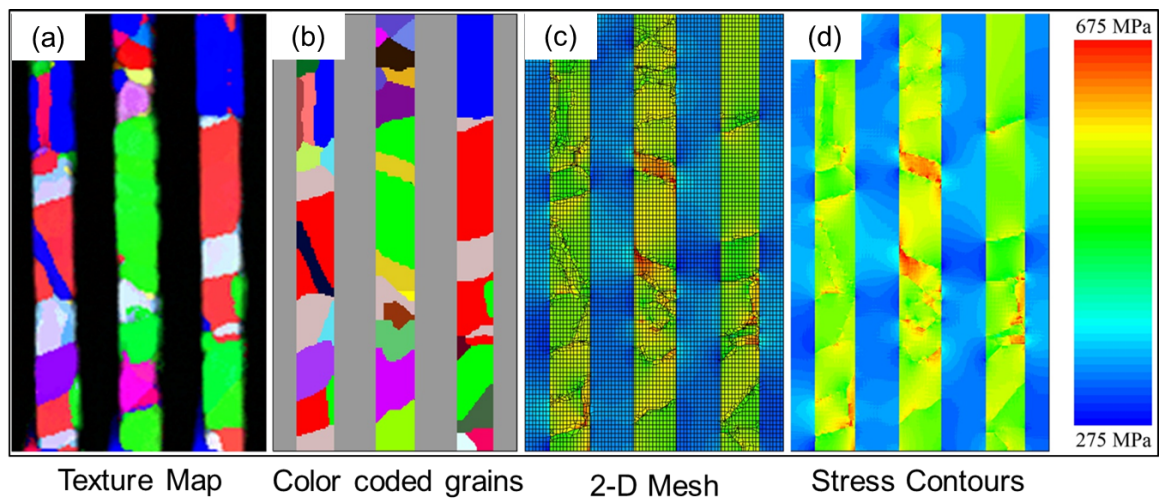
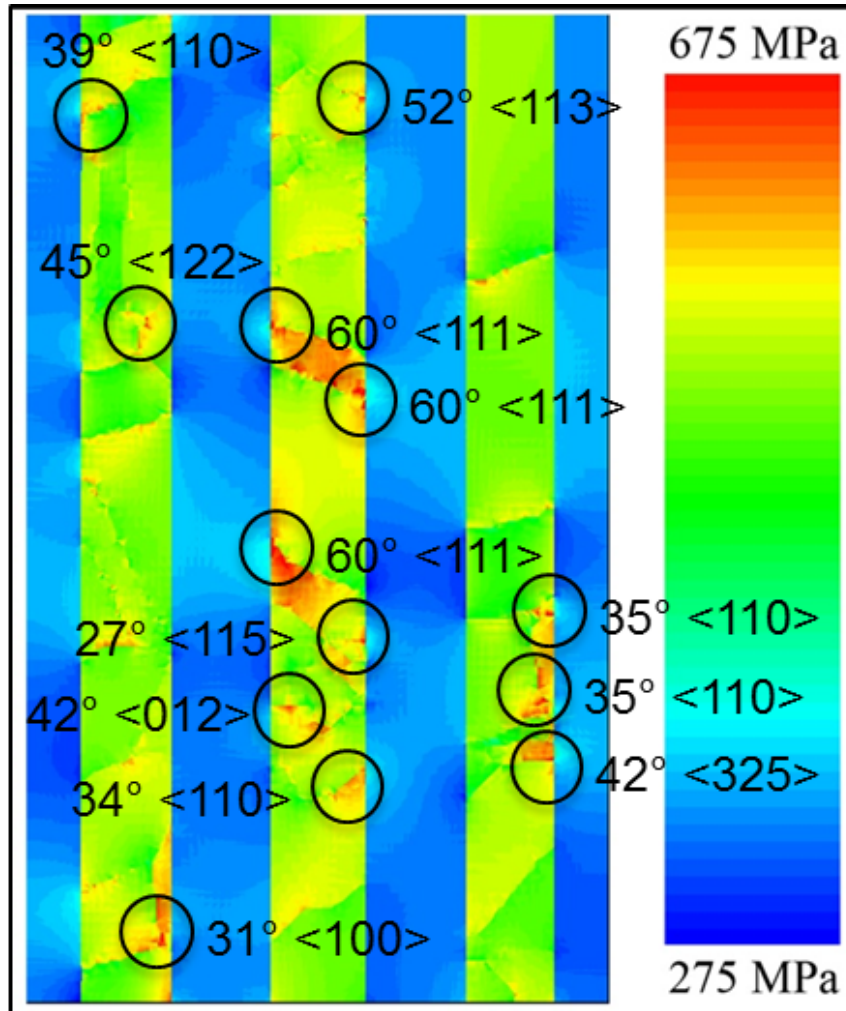


Figure 4.17: (a) Orientation map (b) FEM model with color coded grains (c) 2D mesh (d) Hydrostatic stress contours



Stress Contours

Figure 4.18: Local misorientations in regions of high hydrostatic stresses

4.7 High Resolution Orientation and Phase Mapping Nanoparticles

To explore the power of the precession technique in terms of spatial resolution, orientation mapping was carried out Pt nanoparticles. Pt was chosen because of its role in emerging green energy technologies such as hydrogen or ethanol fuel cells. In this technology, it is of particular interest to tailor and assess particle surface geometry of the particles. This is because the selectivity and efficiency of Pt nanoparticles toward many reactions is very site-specific. However, until now, there are limitations in terms of techniques available for determining orientations from a large number of nanoparticles in an automated manner.

To address this issue we have used the precession technique with a 1-2 nm near parallel probe to analyze orientations from ~ 100 nanoparticles of Pt, about 6 nm in size. Fig. 4.19 shows the reconstructed virtual dark field image of the Pt particles distributed on the grid. Fig. 4.20 shows the color coded orientation map obtained. The colors signify the normal orientation of the particles. The total time of acquisition and pattern indexing was approximately 15 minutes, which is a significant improvement over existing TEM diffraction techniques that would have taken days to accomplish the same. These results also demonstrate that it is possible to acquire rapid, high quality orientation maps by precession from samples sensitive to beam damage by optimizing the acquisition conditions.

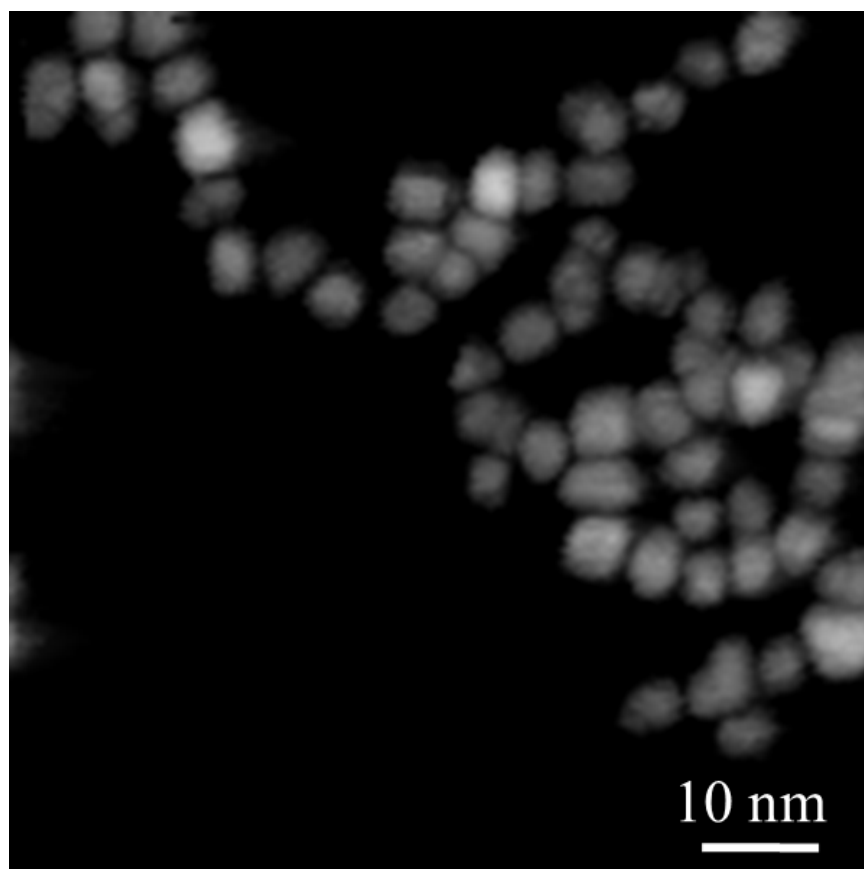


Figure 4.19: Virtual dark field image obtained during precession

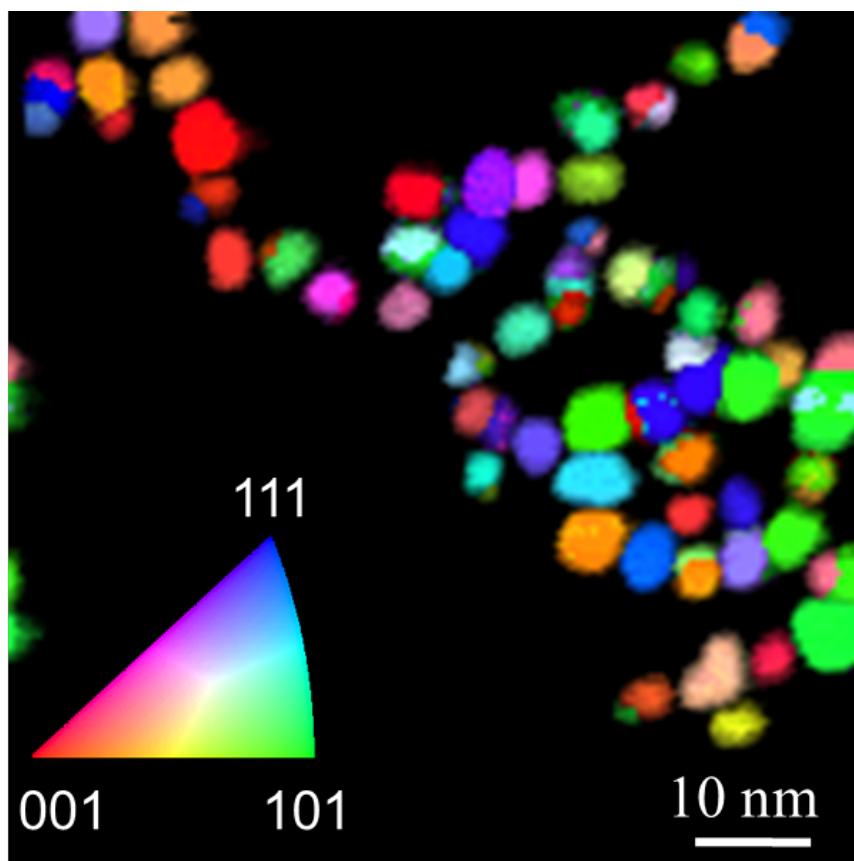


Figure 4.20: Color coded orientation from Pt nanoparticles

Nanocrystalline Ni Films

Research in nanocrystalline Ni films has been of interest recently since they have been shown to exhibit abnormal grain growth. In particular, in-situ TEM heating experiments on Ni film structures deposited by the pulsed laser deposition (PLD) process have demonstrated the presence and growth of large *hcp* phase Ni grains (> 100 nm) within a matrix of nanocrystalline *fcc* Ni [133, 134]. However, it is currently unknown whether nanoscale *hcp* Ni grains are present in as-deposited films due to the limited spatial resolution of conventional characterization techniques for phase mapping. To address this issue, a Diffraction-Scanning Transmission Electron Microscopy (D-STEM) type lens configuration combined with precession electron diffraction has been used to determine the distribution of *fcc* and *hcp* nickel phases, as well as the grain size distribution of nanocrystalline nickel films.

The bright-field TEM image of a representative region from the 50 nm PLD Ni film is shown in Figure 4.21. Although several nanoscale grains are visible in this image, the presence of defects severely limits the overall interpretation of the nanostructure. In contrast, after performing precession electron diffraction analysis, the obtained reliability map distinctly revealed the grain structure and boundaries (Fig. 4.22(a)). When overlaid with the phase maps, the morphology of the *hcp*-Ni and *fcc*-Ni phase grains in the film was also clearly visible (Fig. 4.22(b)). The *fcc* phase grains were colored in red while the *hcp* ones were assigned a cyan color. The diffraction data used to obtain a phase map can also be used to obtain texture and grain boundary

information from the each of the phases present. This example clearly shows that the high resolution orientation mapping technique in the TEM using precession is a versatile technique to characterize texture, grain boundaries, phases and grain size distributions in nanocrystalline materials.

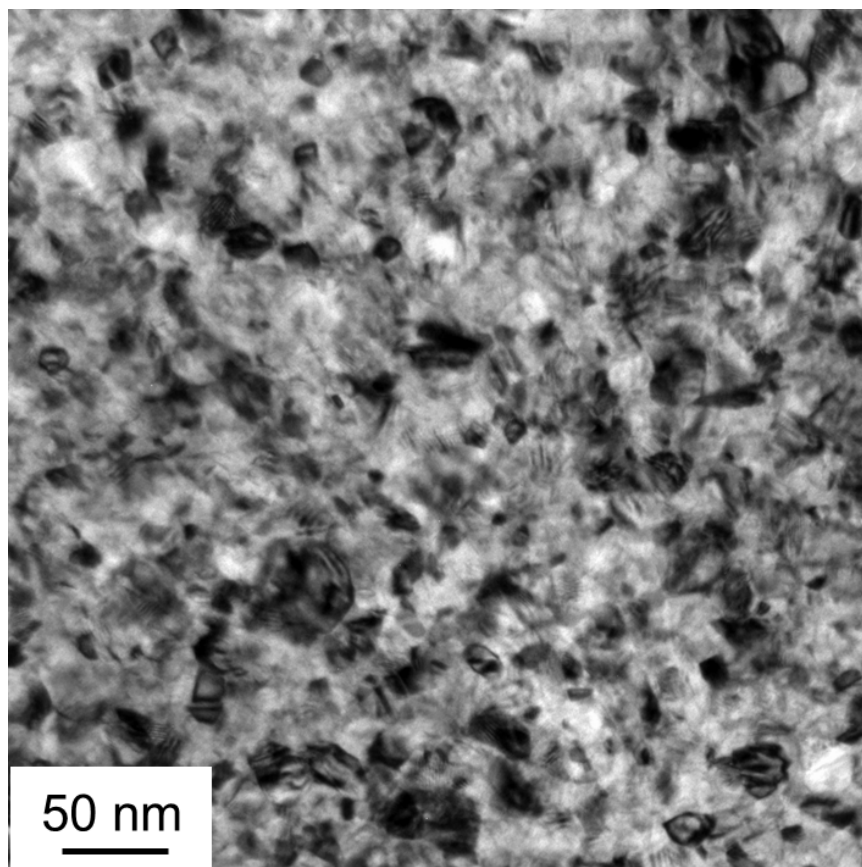
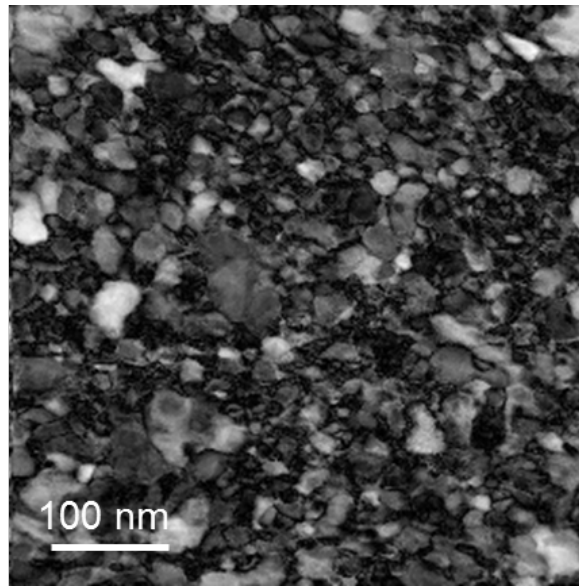
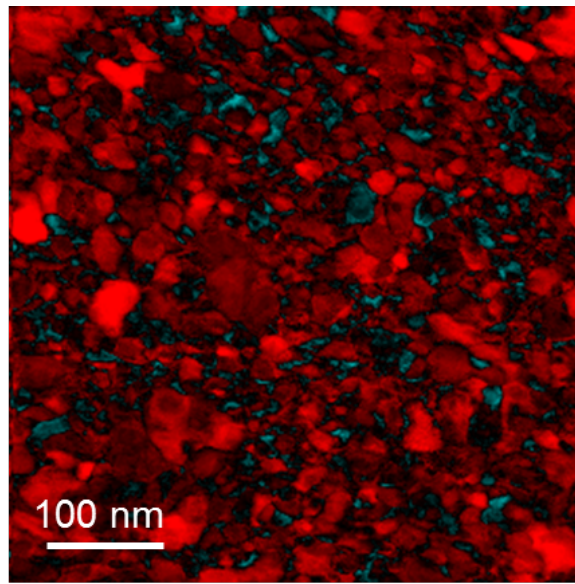


Figure 4.21: Bright field TEM image of PLD Ni film



(a)



■ *fcc* phase
 ■ *hcp* phase

(b)

Figure 4.22: (a) Reliability map obtained after precession analysis (b) Colored phase map overlaid with the reliability map.

4.8 Ambiguities in TEM Orientation Mapping

The reliability of orientation solutions by indexing spot diffraction patterns was discussed by Ryder and Pitsch in 1967 [135]. The issue of the reliability of indexing diffraction patterns using automated procedures especially important due to the fact that a solution is always generated while the solution can be correct or completely incorrect. Particularly, the most important issue regarding the indexing of spot diffraction patterns is the so called 180° ambiguity. For diffraction patterns with a symmetry that is not crystal symmetry, there is no unique indexing solution and therefore, the solution is ambiguous. The reliability index as defined in subsection 3.2.3.2, for such patterns is zero [136]. This issue can be shown for Cu using the following example (Fig. 4.23). The zeroth order Laue zone for [112] pattern is given by the condition $h + k + 2l = 0$ and has two fold symmetry about the microscope axis (180° about the [112]). This can be represented using the rotation matrix M as

$$M = \frac{1}{3} \begin{bmatrix} 2 & 1 & 2 \\ 1 & -2 & 2 \\ 2 & 2 & 1 \end{bmatrix} \quad (4.4)$$

The first order Laue zone for this orientation is represented by $h + k + 2l = 1$. However, the set of reflections satisfying this condition contain both odd and even numbers. Since these reflections are missing due to systematic extinctions for *fcc* structures, spots from the first order Laue zones are missing in the diffraction pattern shown in Fig. 4.23. Therefore, the pattern contains

only the spots from the zero order Laue zone and has the two fold symmetry represented by M . Thus, if O is an orientation solution to the diffraction pattern in Fig. 4.23, then MO is also a solution. However, M is not a crystal symmetry operator and hence, O and MO are physically distinct orientations. The situation just discussed is not unique to $[112]$ patterns in fcc structures. For example, similar situation is also encountered in fcc $[013]$ patterns and $[111]$ patterns in bcc structures. For a quantitative understanding on the reliability of indexing spot patterns, the reliability index for Cu is plotted as function of beam direction in the crystal frame of reference (Fig. 4.24). $[112]$, $[110]$ and $[103]$ orientations are low reliability regions in Fig. 4.24.

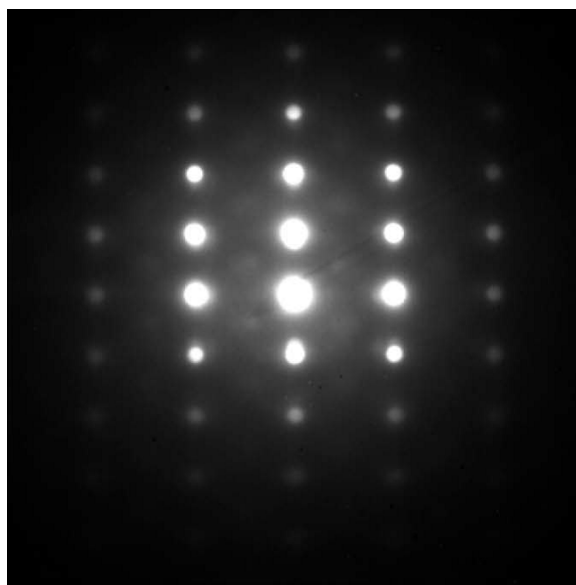
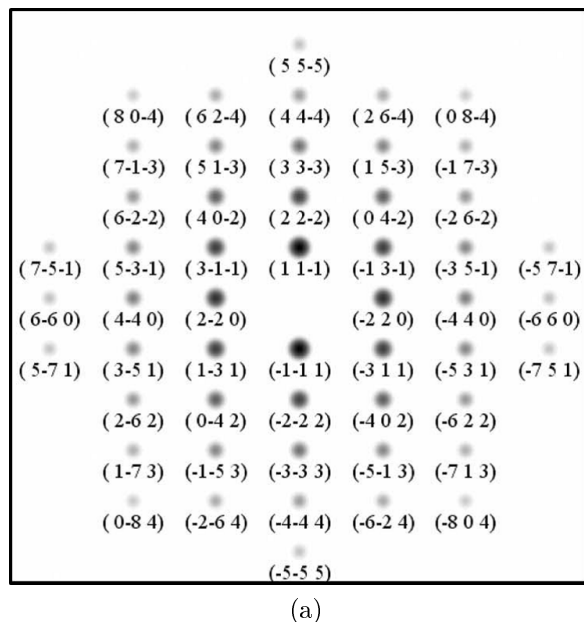


Figure 4.23: (a) Simulated [112] diffraction pattern from Cu and (b) experimental pattern from Cu close to [112] zone axis [136].

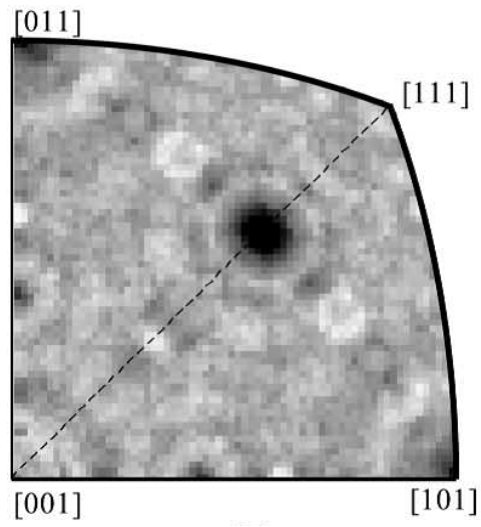


Figure 4.24: Reliability index for Cu as a function of the beam direction in the crystal frame of reference. Dark regions show regions of low reliability [136].

It should be noted that such ambiguities in such situations just mentioned cannot be eliminated by reducing the accelerating voltage or incident beam precession as spots from higher order zones are missing due to systematic extinctions. To illustrate this point more clearly, example of a diffraction patterns from Cu acquired using the ASTARTM system with precession of 0.4° is shown in Fig. 4.25(a). The two orientation solutions were obtained using the cross-correlation algorithm with identical correlation index. In terms of Euler angles the two solutions are $(26^\circ, 17^\circ, 180^\circ)$ (Fig. 4.25(b)) and $(6^\circ, 160^\circ, 260^\circ)$ (Fig. 4.25(c)), respectively. The misorientation between the two solutions is approximately $[1\ 0\ 3]\ 180^\circ$.

One of the solutions to tackle the issue of reliability due to the 180° ambiguity is to use the average information from a neighborhood of points. Small orientation changes are possible within a grain due to the bending or deformation of the thin specimens. Because of small orientation changes within a grain, there are patterns in the neighborhood of high symmetric patterns which are off axis. The reliability index for the solution to the off axis pattern is higher. An example of such a situation is given in Fig. 4.26. The reliability index for the pattern in Fig. 4.26(a) is zero while it is 0.17 for the pattern shown in Fig. 4.26(b). The indexing solution from the pattern Fig. 4.26(b) is shown in Fig. 4.26(c). It is possible to use this information to obtain reliable orientation information. One way to remove boundaries resulting from ambiguities is to exclude boundaries with specimen misorientations characteristic of the ambiguity and assign the orientation of the point with higher reliability

index in the neighborhood [107].

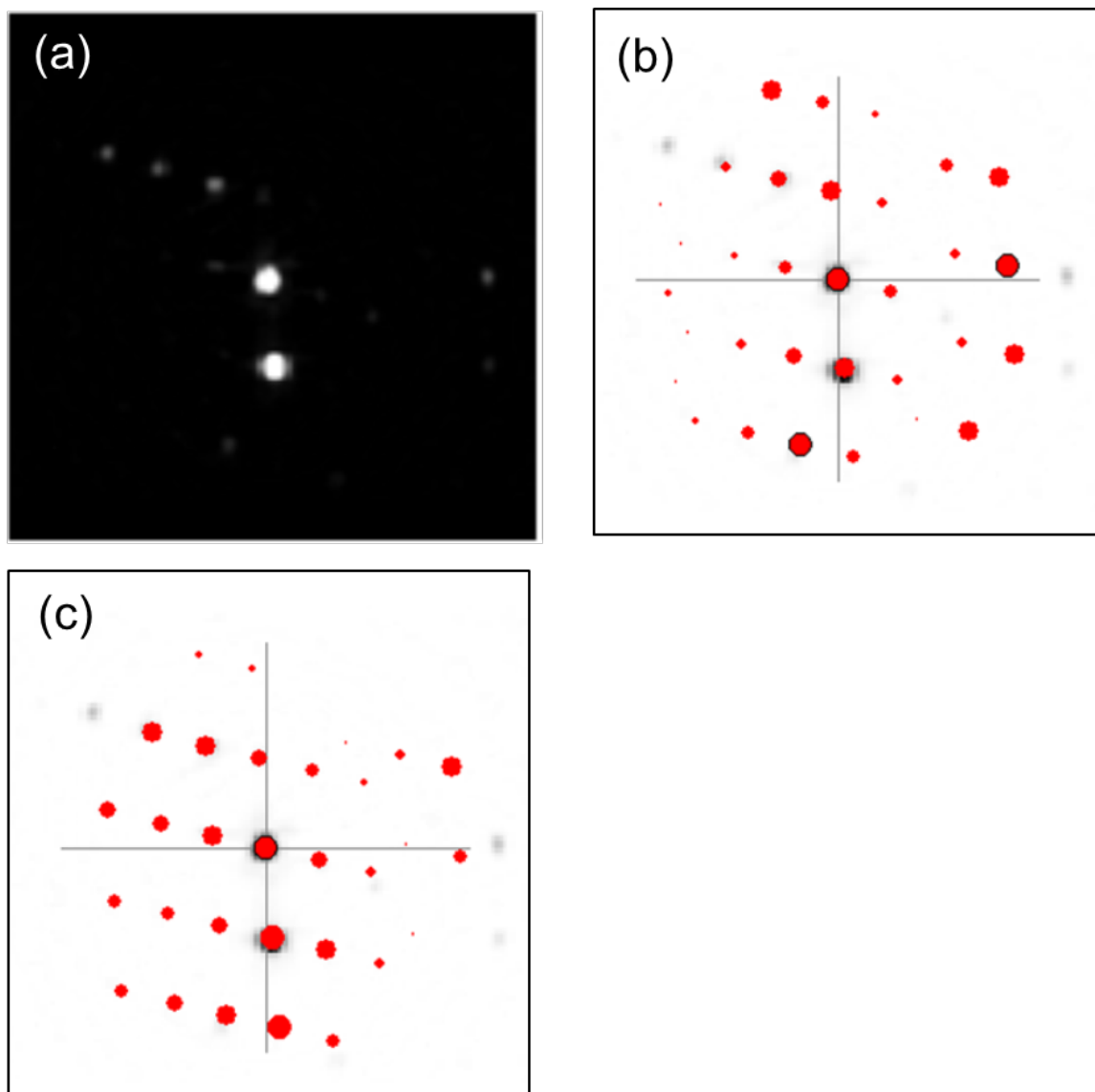


Figure 4.25

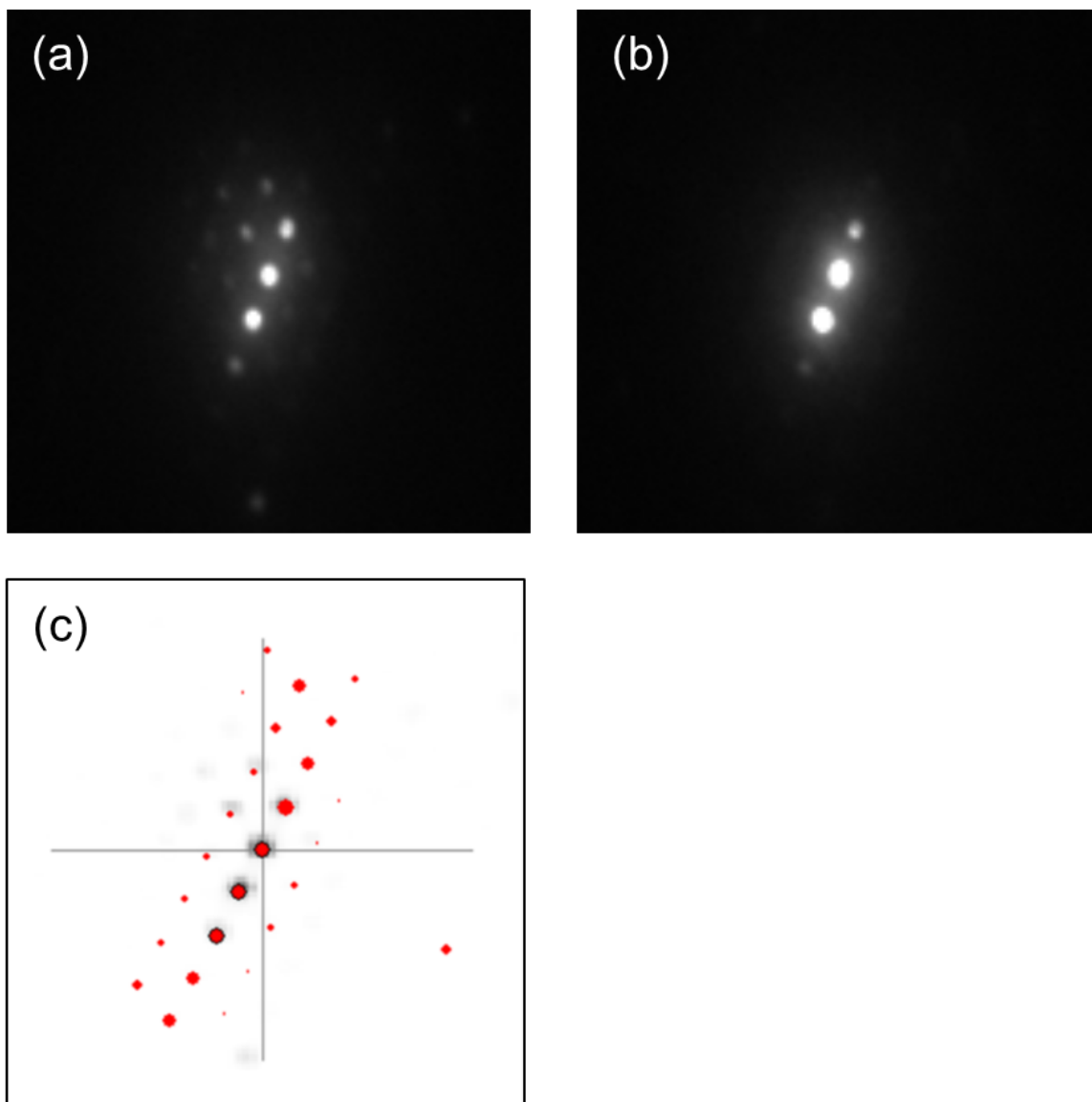


Figure 4.26: (a-b) Diffraction pattern from neighboring points (c) Indexing solution

Chapter 5

Conclusions and Future Work

5.1 Conclusions

The accomplishments of this thesis can be broadly classified into (a) Technique development for high resolution orientation mapping in a TEM and (b) Implementation of the novel technique to investigate the effects of downscaling on the microstructure of nano Cu interconnect lines with the intent to establish correlation with interconnect reliability. Specifically, the following major conclusions can be derived:

1. The D-STEM technique coupled with precession electron diffraction using the ASTARTM system from NanoMEGAS can be used to perform automated orientation mapping of nanostructures in a TEM with a spatial resolution of < 5 nm. In case of multi-phase materials, the technique can also be used to resolve individual phases and orientations of the individual phases in the microstructure. In the thesis, the high spatial resolution of the technique has been demonstrated by obtaining orientation maps from Pt nanoparticles ~ 6 nm in size. The high resolution phase mapping feature has been demonstrated by identifying metastable *hcp* phase grains (< 10 nm in size) in a polycrystalline PLD Ni film sample.

2. Quantitative microstructure information can be derived from the obtained orientation data after following the π - inversion and frame of reference calibration routines outlined in the thesis.
3. Implementation of the orientation mapping technique to Cu interconnect structures with widths ranging from 1.8 μm - 70 nm showed that interconnect downscaling brings about drastic changes in the microstructure of the Cu lines. 1.8 μm and 180 nm wide lines showed a dominant $\langle 111 \rangle$ fiber texture consistent with the growth of $\{111\}$ grains along the trench normal. However, the narrower lines, 120 nm in width did not show a dominant normal texture. Instead, a slight $\langle 111 \rangle$ texture normal to the trench sidewall was observed. Similar analysis on narrower lines, 70 nm in width, revealed a strong $\langle 111 \rangle$ texture normal to the trench sidewall and a strong $\langle 110 \rangle$ texture normal to the trench bottom. The dominant $\langle 111 \rangle$ texture along the sidewall normal in narrow lines has been attributed to the dominant growth of sidewall $\{111\}$ grains.
4. Quantitative analysis of grain boundary character in the aforementioned lines showed a decrease in the fraction of coherent twin boundaries in Cu lines upon downscaling. The results also showed a corresponding increase in the population of non-CSL high angle boundaries. Analysis of the grain structure of the interconnect lines based on the obtained orientation and reconstructed boundary maps showed a variation with decreasing line width. While the microstructure of the 1.8 μm and 180

nm wide lines comprised large micron sized and near-bamboo type grains respectively, the microstructure of 120 nm wide lines comprised clusters of small grains separated by large bamboo or near-bamboo type grains while the 70 nm wide lines showed a polygranular grain structure. It was also analyzed that the small grains in the cluster were equiaxed in morphology and the grain boundaries separating them were non-CSL high angle boundaries. Cross section analysis performed on the 70 nm wide lines also showed the presence of small grain clusters at the trench bottom. Almost all the small grains at the trench bottom were also found to be separated by high angle boundaries.

5. The microstructure evolution in narrow Cu lines is driven by thermodynamics, but is constrained by the kinetics involving growth of sidewall, bottom-up and overburden grains. Subject to the aforementioned constraints, although the system tries to attain a grain structure with the minimum total energy, it is composed of metastable states with local energy minima. The total energy of the system includes surface energy, grain boundary energy, interfacial energy and strain energy. With reduction in line width, the surface/interface area to volume ratio increases. Thus, the surface and interface energy minimization begins to dominate the volumetric energy minimization. In narrow lines, the invasion of the overburden layer into the trench is restricted by the growth of sidewall $\{111\}$ grains. The resulting microstructure is thus composed of clusters of small grains in the vicinity of some large grains. This phenomenon

becomes more severe with reducing line width, thereby resulting in a polygranular structure, as observed in 70 nm wide lines. The preferential growth of $\{111\}$ grains occurs along the normal to the trench sidewall with specific $\langle 110 \rangle$ orientations along the trench normal to minimize the interfacial and surface energies. The subsequent orientation of the $\langle 112 \rangle$ along the line length also minimizes the strain energy. The competing sidewall and bottom-up growth in narrower lines results in small grain clusters at the trench bottom.

6. Analysis on narrow via/line structures fabricated for EM tests, also revealed the presence of small grain clusters in the via in proximity to large grains. The small grains were found to be separated by high angle boundaries. The presence of such small grains separated by high angle boundaries near large grains sharing twin boundaries can increase flux divergence and increase susceptibility to EM. Misorientation and flux divergence analysis around an EM void also showed that maximum flux divergence existed at the triple junction where two Cu grains separated by a high misorientation intersected the SiCN capping layer.
7. 2D microstructural FEM analysis performed to investigate local stresses revealed the presence of high and low stress regions in the Cu microstructure. Unlike conventional FEM simulations performed on Cu lines, the microstructural FEM analysis accounts for the polycrystalline nature of the Cu lines, and also the elastic anisotropy of Cu. The results revealed

that high hydrostatic stress regions seem to be close to Cu grains separated by high misorientations. The stress contours obtained showed evidence of sharp stress gradients in the microstructure. Since hydrostatic stress gradient is the driving force for SIV, such analysis could provide key insight into the potential flux divergence sites for SIV. However, to establish such a correlation, the FEM analysis needs to be modified to couple stress gradient contours with mass transport parameters such as diffusivity of the surfaces, bulk and grain boundaries. A recently developed FEM package with this novel feature is currently being pursued for performing such studies.

5.2 Future Work

For future research, my suggestions are as follows:

1. From the perspective of electron microscopy technique development: to improve the speed of acquisition of precession electron diffraction patterns by an order of magnitude by optimizing exposure and using improved phosphor and direct camera in the TEM.
2. To investigate texture, grain structure and grain boundary distributions in as-deposited interconnect structures and subsequently study the effects of various annealing conditions on the grain growth characteristics and subsequent microstructure evolution in Cu interconnects.
3. To investigate microstructure changes in Cu lines deposited with different

barrier/seed layers.

4. Performing 2D and 3D FEM simulations on Cu lines by coupling stress gradients and mass transport parameters (diffusivity of bulk, interfaces and grain boundaries) to generate a microstructure dependent spatial distribution of flux divergence for SIV.
5. Performing similar FEM analysis to obtain a microstructure dependent spatial distribution of EM induced flux divergence

Bibliography

- [1] KPMG report, “Semiconductor industry strength in an unpredictable global economic recovery” (2010) http://www.kpmg.com/Global/en/Issues_AndInsights/ArticlesPublications/Documents/semiconductor-global-survey-q4v2.pdf
- [2] G. Moore, “Cramming more components onto integrated circuits”, *Electronics*, 38 (1965) 114-117
- [3] ITRS, “Interconnect”, <http://www.itrs.net/links/2009ITRS> (2009)
- [4] R. Haveman, “High Performance Interconnects: An Integration Overview”, *Proceedings of the IEEE*, 89 (2001) 586-609
- [5] www.intel.com/museum/archives/history_docs/moore.htm?wapkw=moore
- [6] J. An, “Thermal Stress Induced Voids in Nanoscale Cu Interconnects by In-Situ TEM Heating” (2007)
- [7] D. Edelstein, J. Heidenreich, R. Goldblatt, W. Cote, C. Uzoh, N. Lustig, P. Roper, T. McDevitt, W. Motsifft, A. Simon, J. Dukovic, R. Wachnik, H. Rathore, R. Schulz, L. Su, S. Lucet, J. Slattery, “Full Copper Wiring in a Sub-0.25 μm CMOS ULSI Technology”, *IEEE Proceedings of the IEDM*,

(1997) 773-776

[8] International Technology Roadmap for Semiconductors (2009)

[9] B. Li, T. Sullivan, T. Lee, D. Badami, “Reliability Challenges for Copper Interconnects, Microelectronics Reliability”, Microelectronics Reliability, 44 (2004) 365-380

[10] P. Ho, T. Kwok, “Electromigration in Metals”, Reports on Progress in Physics, 52 (1989) 301-348

[11] J. Lloyd, J. Clement, “Electromigration in Copper Conductors”, Thin Solid Films, 262 (1995) 135-141

[12] J. Proost, T. Hirato, T. Furuhashi, K. Maex, J. Celis, “Microtexture and Electromigration-Induced Drift in Electroplated Damascene Cu”, Journal of Applied Physics, 87 (2000) 2792-2802

[13] Z. Zhang, Z. Suo, J. He, “Saturated Voids in Interconnect Lines due to Thermal Strains and Electromigration”, Journal of Applied Physics, 98 (2005) 074501-1 - 074501-8

[14] C. Hu, K. Rodbell, T. Sullivan, K. Lee, D. Bouldin, “Electromigration and Stress-Induced Voiding in Fine Al and Al-alloy Thin-film Lines”, IBM Journal

of Research and Development, 39 (1995) 465-497

[15] L. Arnaud, G. Tartavel, T. Berger, D. Mariolle, Y. Gobil, I. Touet, “Microstructure and Electromigration in Copper Damascene Lines”, *Microelectronics Reliability*, 40 (2000) 77-86

[16] C. S. Hau-Riege, C. V. Thompson, “Electromigration in Copper Interconnects with Very Different Grain Structures”, *Thin Solid Films*, 78 (2001), 3451-3453

[17] A. Sekiguchi, J. Koike, S. Kamiya, M. Saka, K. Maruyama, “Void Formation by Thermal Stress Concentration at Twin Interfaces in Cu Thin Films”, *Applied Physics Letters*, 79 (2001) 1264-1266

[18] R. Gleixner, B. Clemens, W. Nix, “Void Nucleation in Passivated Interconnect Lines: Effects of Site Geometries, Interfaces, and Interface Flaws”, *Journal of Materials Research*, 12 (1997) 2081-2090

[19] A. Wikstroom, P. Gudmundson, S. Suresh, “Analysis of Average Thermal Stresses in Passivated Metal Interconnects”, *Journal of Applied Physics*, 86 (1999) 6088-6095

[20] J. Koike, M. Wada, M. Sanada, K. Maruyama, “Effects of Crystallographic Texture on Stress-Migration Resistance in Copper Thin Films”, *Ap-*

plied Physics Letters 81 (2002) 1017-1019

[21] H. Park, S. Hwang, Y. Joo, “Stress-Induced Surface Damage and Grain Boundary Characteristics of Sputtered and Electroplated Copper Thin Films”, *Acta Materialia*, 52 (2004) 2435-2440

[22] E. Ogawa, J. McPherson, J. Rosal, K. Dickerson, T. Chiu, L. Tsung, M. Jain, T. Bonifield, J. Ondrusek, W. McKee, “Stress-Induced Voiding under Vias Connected to Wide Cu Metal Leads”, *Reliability Physics Symposium Proceedings*, (2002) 312-321

[23] H. Okabayashi, “Stress-Induced Void Formation in Metallization for Integrated Circuits”, *Materials Science and Engineering*, 11 (1993) 191-241

[24] D. Kim, J. Paik, Y. Joo, K. Oh, H. Lee, K. Dicks, “Microstructure Measurement of Copper Damascene Line with EBSD”, *Mater. Sci. Forum*, 408 (2002) 529-534

[25] H. Lee, H. Han, D. Lee, “Annealing Textures of Copper Damascene Interconnects for Ultra-Large Scale Integration”, *Journal of Electronic Materials*, 34 (2005) 1493-1499

[26] P. Besser, E. Zschech, W. Blum, D. Winter, R. Ortega, S. Rose, M. Herrick, M. Gall, S. Thrasher, M. Tiner, B. Baker, G. Braeckelmann, L. Zhao, C. Simpson, C. Capasso, H. Kawasaki, E. Weitzman, “Microstructural Character-

ization of Inlaid Copper Interconnect Lines”, *Journal of Electronic Materials*, 30 (2001) 320-330

[27] D. Lee, H. Lee, “Effect of Stresses on the Evolution of Annealing Structures in Cu and Al interconnects”, *Journal of Electronic Materials*, 32 (2003) 1012-1022

[28] D. Field, D. Dornisch, H. Tong, “Investigating the Microstructure-Reliability Relationship in Cu Damascene Lines”, *Scripta Materialia*, 45 (2001) 1069-1075

[29] S. Brandstetter, V. Carreau, S. Maitrejean, M. Verdier, M. Legros, “Grain Morphology of Cu Damascene Lines”, *Microelectronic Engineering*, 87 (2010a) 383-386

[30] S. Brandstetter, V. Carreau, S. Maitrejean, M. Verdier, M. Legros, “Pattern Size Dependence of Grain Growth in Cu Interconnects”, *Scripta Materialia*, 63 (2010b) 965-968

[31] W. Steinhogel, G. Schindler, G. Steinlesberger, M. Traving, M. Engelhardt, “Comprehensive Study of the Resistivity of Copper Wires with Lateral Dimensions of 100 nm and Smaller” *Journal of Applied Physics*, 97 (2005) 023706-1 - 023706-7

[32] V. Carreau, S. Maîtrejean, M. Verdier, Y. Bréchet, A. Roule, A. Toffoli,

V. Delaye, G. Passemard, “Evolution of Cu Microstructure and Resistivity during Thermal Treatment of Damascene Line: Influence of Line Width and Temperature”, *Microelectronic Engineering*, 84 (2011) 2733-2739

[33] D. Knorr, K. Rodbell, “The Role of Texture in the Electromigration Behavior of Pure Aluminum Lines”, *Journal of Applied Physics*, 79 (1996) 2409-2417

[34] A. Campbell, R. Mikawa, D. Knorr, “Relationship between Texture and Electromigration Lifetime in Sputtered Al-1% Si Thin Films”, *Journal of Electronic Materials*, 22 (1993) 589-596

[35] D. Knorr, D. Tracy, K. Rodbell, “Correlation of Texture with Electromigration Behavior in Al Metallization”, *Applied Physics Letters*, 59 (1993) 3241-3243

[36] J. Nucci, Y. Shacham-Diamand, J. Sanchez, Jr., “Effects of Linewidth, Microstructure, and Grain Growth on Voiding in Passivated Copper Lines” *Applied Physics Letters*, 66 (1995) 3585-3587

[37] J. Nucci, R. Keller, J. Sanchez, Y. Shacham-Diamand, Jr., “Local Crystallographic Texture and Voiding in Passivated Copper Interconnects”, *Applied Physics Letters*, 69 (1996) 4017-4019

[38] S-H. Rhee, Y. Du, P. Ho, “Thermal Stress Characteristics of Cu/Oxide and

Cu/Low-k Submicron Interconnect Structures”, Journal of Applied Physics, 93 (2003) 3926-3933

[39] T. Gupta, “Aluminum Alloy as an Interconnecting Material in the Fabrication of Integrated Circuits”, Microelectronics Reliability, 19 (1979) 337-343

[40] K. Saraswat, Lecture notes, Stanford, 2009

[41] S. Crowder, S. Greco, H. Ng, E. Barth, K. Beyer, G. Biery, J. Connolly, C. DeWan, R. Ferguson, X. Chen, M. Hargrove, E. Nowak, P. McLaughlin, R. Purtell, R. Logan, J. Oberschmidt, A. Ray, D. Ryan, K. Tallman, T. Wagner, V. McGahay, E. Crabbe, P. Agnello, R. Goldblatt, L. Su, and B. Davari, “A 0.18 Micron High-Performance Logic Technology”, in Symp. VLSI Tech. Dig. Tech. Papers, (1999) 105-106

[42] Howard B. J. & Steinbruchel C., “Reactive Ion Etching of Copper in SiCl₄-Based Plasmas”, Applied Physics Letters, 59 (1991) 914-916

[43] Lijuan Zhang, “Effects of Scaling and Grain Structure on Electromigration Reliability of Cu Interconnects”, (2010)

[44] S. Wolf, Silicon processing for VLSI Era, Lattice Press, Sunset Beach, CA, 4 (1986)

[45] H. Huntington, A. Grone, “Current-induced marker motion in gold wires”,

20 (1961) 76-87

[46] P. Ho, T. Kwok, "Electromigration in Metals", Reports on Progress in Physics, 52 (1989) 301-348

[47] I. Blech, H. Sello, "The Failure of Thin Aluminum Current-Carrying Strips on Oxidized Silicon", Fifth Annual Symposium on the Physics of Failure in Electronics, November (1966) 496-505

[48] C. Hau-Riege, "An Introduction to Cu Electromigration", Microelectronics Reliability, 44 (2004) 195-205

[49] C. Hu, S. Reynolds, "Chemical Vapor Deposition of Cu Interconnections and Electromigration", Electrochemical Soc. Proc., 1514 (1997) 97-25

[50] P. Ho, E. Zschech, D. Schmeisser, M. Meyer, R. Huebner, M. Hauschildt, L. Zhang, M. Gall, M. Kraatz, "Scaling Effects on Microstructure and Reliability for Cu Interconnects", International Journal of Materials Research, 101 (2010) 216-227

[51] C. Hu, L. Gignac, R. Rosenberg, E. Liniger, J. Rubino, C. Sambucetti, A. Domenicucci, X. Chen, A. Stamper, "Reduced Electromigration of Cu Wires by Surface Coating" Applied Physics Letters, 81 (2002) 1782-1784

[52] A. Fischer, A. von Glasow, S. Penka, & F. Ungar, "Electromigration

Failure Mechanism Studies on Copper Interconnects”, IEEE International Interconnect Technology Conference Proceedings, (2002) 139-141

[53] S. Tokogawa, H. Takizawa, “Electromigration Induced Incubation, Drift and Threshold in Single-Damascene Copper Interconnects”, IEEE International Interconnect Technology Conference Proceedings, (2002) 127-129

[54] T. Surholt, C. Herzig, “Grain Boundary Self-Diffusion in Cu Polycrystals of Different Purity”, *Acta Materialia*, 45 (1997) 3817-3823

[55] T. Surholt, Y. Mishin, C. Herzig, “Grain-Boundary Diffusion and Segregation of Gold in Copper: Investigation in the Type-B and Type-C Kinetic Regimes”, *Physical Review B*, 50 (1994) 3577-3587

[56] J. Lin, S. Park, K. Pfeifer, R. Augur, V. Blaschke, S. Shue, H. Yu, M. Liang, “Electromigration Reliability Study of Self-Ionized Plasma Barriers for Dual Damascene Cu Metallization”, *Materials Research Society Proceedings*, (2003) 233-237

[57] C. Hu, D. Canaperi, S. Chen, L. Cignac, B. Herbst, S. Kaldor, M. Krishnan, E. Liniger, D. Rath, D. Restaino, R. Rosenberg, J. Rubino, S.-C. Seo, A. Simon, S. Smith, W. Tseng, “Effects of Overlayers on Electromigration Reliability Improvement for Cu/Low K Interconnects”, IEEE International

Reliability Physics Symposium Proceedings, (2004) 222-228

[58] C. Hu, L. Gignac, E. Liniger, B. Herbst, D. Rath, S. Chen, S. Kaldor, A. Simon, W. Tseng, “Comparison of Cu Electromigration Lifetime in Cu Interconnects Coated with Various Caps”, Applied Physics Letters, 83 (2003) 869-871

[59] S. Demuyne, Z. Tokei, C. Bruynseraede, J. Michelon, K. Maex, “Alpha-Ta Formation and its Impact on Electromigration”, Advanced Metallization Conference, (2004) 355-359

[60] S. Rothman, N. Peterson, “Isotope Effect and Divacancies for Self-Diffusion in Copper”, Physica Status Solidi, 35 (1969) 305-312

[61] M. Gall, “Investigation of Electromigration Reliability in Al(Cu) Interconnects”, PhD Dissertation (1999)

[62] C. Hu, L. Gignac, R. Rosenberg, “Electromigration of Cu/low dielectric constant interconnects”, Microelectronics Reliability, 46 (2006) 213-231

[63] A. Wikstrom, P. Gudmundson, S. Suresh, “Analysis of Average Thermal Stresses in Passivated Metal Interconnects”, Journal of Applied Physics, 86

(1999) 6088-6095

[64] J. Koike, M. Wada, M. Sanada, K. Maruyama, "Effects of Crystallographic Texture on Stress-Migration Resistance in Copper Thin Films", *Applied Physics Letters*, 81 (2002) 1017-1019

[65] P. Borgesen, J. Lee, R. Gleixner, C. Li, "Thermal Stress-Induced Voiding in Narrow, Passivated Cu Lines", *Applied Physics Letters*, 60 (1992) 1706-1708

[66] R. Keller, S. Baker, E. Arzt, "Stress Temperature Behavior of Unpassivated Thin Copper Films", *Acta Materialia*, 47 (1999) 415-426

[67] D. Gan, S. Yoon, P. Ho, "Effects of Passivation Layer on Stress Relaxation in Cu Line Structures", *IEEE International Interconnect Technology Conference*, (2002a) 180-182

[68] G. Dehm, D. Weiss, E. Arzt, "In situ TEM Study of Thermal-Stress-Induced Dislocation in a Thin Cu Film Constrained by a Si Substrate", *Materials Science and Engineering: A*, 309-310 (2001) 468-472

[69] R. Vinci, E. Zielinski, J. Bravman, "Thermal Strain and Stress in Copper Thin Films", *Thin Solid Films*, 262 (1995) 142-153

[70] M. Thouless, J. Gupta, J. Harper, "Stress Development and Relaxation

in Copper Films During Thermal Cycling”, *Journal of Materials Research*, 8 (1993) 1845-1852

[71] P. Flinn, “Measurement and Interpretation of Stress in Copper Films as a Function of Thermal History”, *Journal of Materials Research*, 6 (1991) 1498-1501

[72] O. Kraft, L. Freund, R. Phillips, E. Arzt, “Dislocation Plasticity in Thin Metal Films”, *MRS Bulletin* January (2002) 30-37

[73] D. Gan, G. Wang, P. Ho, “Effects of Dielectric Material and Linewidth on Thermal Stresses of Cu Line Structures”, *IEEE International Interconnect Technology Conference Proceedings*, (2002b) 271-273

[74] E. Ege, Y. Shen, “Thermomechanical Response and Stress Analysis of Copper Interconnects”, *Journal of Electronic Materials*, 32 (2003) 1000-1011

[75] I. Dutta, M. Chen, K. Peterson, T. Shultz, “Plastic Deformation and Interfacial Sliding in Al and Cu Thin Film: Si Substrate Systems due to Thermal Cycling”, *Journal of Electronic Materials*, 30 (2001) 1537-1548

[76] B. Inkson, G. Dehm, T. Wagner, “In situ TEM Observations of Dislocation Motion in Thermally Strained Al Nanowires”, *Acta Materialia*, 50 (2002) 5033-

- [77] T. Balk, G. Dehm, E. Arzt, “Parallel Glide : Unexpected Dislocation Motion Parallel to the Substrate in Ultrathin Copper Films”, *Acta Materialia*, 51 (2003) 4471-4485
- [78] G. Dehm, E. Arzt, “In Situ TEM Study of Dislocations in a Polycrystalline Cu Thin Film Constrained by a Substrate”, *Applied Physics Letters*, 77 (2000) 1126-1128
- [79] M.A. Korhonen, P. Borgesen, Che-Yu Li, “Mechanisms of Stress-induced and Electromigration-induced Damage in Passivated Narrow Metallizations on Rigid Substrates”, *MRS Bulletin*, July (1992) 61-68
- [80] A. Morawiec, *Orientations and Rotations: Computations in Crystallographic Textures*, Springer (2004)
- [81] U. Kocks, C. Tomé, H-R. Wenk, *Texture and Anisotropy: Preferred Orientations in Polycrystals and their Effect on Materials Properties*, Cambridge University Press (2000)
- [82] M. Shuster, “A Survey of Attitude Representations”, *Journal of the Astronautical Sciences*, 41 (1993) 439-517

- [83] R. Courant and D. Hilbert, *Methods of mathematical physics: Volume 1*, Wiley (1953)
- [84] A. Sutton and R. Balluffi, *Interfaces in Crystalline Materials*, Clarendon Press, Oxford (1995)
- [85] D. McLean, *Grain Boundaries in Metals*, Oxford University Press (1957)
- [86] G. Rohrer, D. Saylor, B. Dasher, B. Adams, A. Rollett, P. Wynblatt, “The distribution of Internal Interfaces in Polycrystals”, *Zeitschrift für Metallkunde*, 95 (2004) 197-214
- [87] V. Randle, *The Role of Coincident Site Lattice in Grain Boundary Engineering*, Cambridge University Press (1996)
- [88] K. Lu, L. Lu, S. Suresh, “Strengthening Materials by Engineering Coherent Internal Boundaries at the Nanoscale”, *Science*, 324 (2009) 349-352
- [89] S. Ranganathan, “On the Geometry of Coincidence-Site Lattices”, *Acta Crystallographica*, 21 (1966) 197-199
- [90] C. Goux, “Structure of Joined Grains - Crystallographic Consideration and Methods of Structure Estimation”, *Canadian Metallurgical Quarterly*, 13

(1974) 9-31

[91] B. Fultz, J. Howe, Transmission Electron Microscopy and Diffractometry of Materials, Springer (2001)

[92] C. Kittel, Introduction to Solid State Physics, Wiley (2004)

[93] W. Bragg, "X-Rays and Crystal Structure", Philosophical Transactions of the Royal Society of London. Series A, 215 (1915) 253-274

[94] B. Cullity, S. Stock, Elements of X-ray diffraction, Prentice Hall (2001)

[95] A. Schwartz, M. Kumar, Electron Backscatter in Materials Science, Springer (2001)

[96] P. Hough, "Machine Analysis of Bubble Chamber Pictures", International Conference on High Energy Accelerators and Instrumentation, (1959)

[97] D. Dingley, D. Field, Materials Science and Technology, 13 (1997) 69-78

[98] D. Williams, C. Carter, Transmission Electron Microscopy, Springer (2008)

[13] J. Cowley, "Electron Nanodiffraction", Microscopy Research Technique, 46 (1999), 75-97

[99] J. Cowley, D. Janney, R. Gerkin, P. Buseck, "The Structure of Ferritin Cores determined by Electron Nanodiffraction", Journal of Structural Biology,

131 (2000) 210-216

[100] U. Kolb, T. Gorelik, C. Kubel, M. Otten, D. Hubert, “Towards Automated Diffraction Tomography: Part I - Data Acquisition”, *Ultramicroscopy*, 107 (2007) 507-513

[101] H. He, C. Nelson, “A Method of Combining STEM image with Parallel Beam Diffraction and Electron-Optical Conditions for Diffractive Imaging”, *Ultramicroscopy*, 107 (2007) 340-344

[102] H. Lee, H. Han, D. Lee, “Annealing Textures of Copper Damascene Interconnects for Ultra-Large Scale Integration”, *Journal of Electronic Materials*, 34 (2005) 1493-1499

[103] J. Cho, H. Lee, H. Kim, J. Szpunar, “Textural and Microstructural Transformation of Cu Damascene Interconnects After Annealing”, *Journal of Electronic Materials*, 34 (2005) 506-514

[104] K. Ganesh, M. Kawasaki, J. P. Zhou, P. J. Ferreira, “D-STEM: A Parallel Electron Diffraction Technique Applied to Nanomaterials”, *Microscopy and Microanalysis*, 16 (2010a) 614-621

[105] R. Vincent, P. Midgley, “Double Conical Beam-Rocking System for Measurement of Integrated Electron Diffraction Intensities”, *Ultramicroscopy*, 53

(1994) 271-282

[106] J. Gjønnes, V. Hansen, B. Berg, P. Runde, Y. Cheng, K. Gjønnes, D. Dorset, C. Gilmore, Structure Model for the Phase Al₂Fe Derived from Three-Dimensional Electron Diffraction Intensity Data Collected by a Precession Technique. Comparison with Convergent-Beam Diffraction”, *Acta Crystallographica Section A*, 54 (1998) 306-319

[107] E. Rauch, L. Dupuy, “Comments on ‘On the Reliability of Fully Automatic Indexing of Electron Diffraction Patterns Obtained in a Transmission Electron Microscope’ by Morawiec and Bouzy”, *Journal of Applied Crystallography*, 39 (2006) 104-105

[108] J. Portillo, E. Rauch, S. Nicolopoulos, M. Gemmi, D. Bultreys, “Precession Electron Diffraction Assisted Orientation Mapping in the Transmission Electron Microscope”, *Materials Science Forum*, 644 (2010) 1-7

[109] P. Oleynikov, S. Hovmöller, X. Zou (2007), “Precession Electron Diffraction: Observed and Calculated intensities”, *Ultramicroscopy*, 107 (2007) 523-533

[110] E. Rauch, A. Duft, “Orientation Maps Derived from TEM Diffraction Patterns Collected with an External CCD Camera”, *Materials Science Forum*,

495-497 (2005) 197-202

[111] E. Rauch, M. Veron, “Coupled Microstructural Observations and Local Texture Measurements with an Automated Crystallographic Orientation Mapping Tool Attached to a TEM”, *Materialwissenschaft und Werkstofftechnik*, 36, (2005) 552-556

[112] T. Courtney, *Mechanical Behavior of Materials*, Mcgraw-Hill (2000)

[113] K. Ganesh, S. Rajasekhara, J. Zhou, P. Ferreira, “Texture and Stress Analysis of 120 nm Copper Interconnects”, *Scripta Materialia*, 62 (2010b) 843-846

[114] S. Wright, R. Larsen, “Extracting twins from orientation imaging microscopy scan data”, *Journal of Microscopy*, 205 (2002) 245-252

[115] D. Brandon, “The Structure of High Angle Grain Boundaries”, *Acta Metallurgica*, 14 (1966) 1479-1484

[116] J. Cho, K. Mirpuri, D. Lee, J. An, J. Szpunar, “Texture Investigation of Copper Interconnects with a Different Line Width”, *Journal of Electronic Materials*, 34 (2005) 53-61

[117] D. Walton, H. Frost, C. Thompson, “Development of Near Bamboo and Bamboo Microstructures in Thin Film Strips”, *Applied Physics Letters*, 61

(1992) 40-42

[118] B. Knowlton, J. Clement, C. Thompson, "Simulation of the Effects of Grain Structure and Grain Growth on Electromigration and the Reliability of Interconnects", *Journal of Applied Physics*, 81 (1997) 6073-6080

[119] W. Fayad, V. Andleigh, C. Thompson, "Modeling of the Effects of Crystallographic Orientation on Electromigration-Limited Reliability of Interconnects with Bamboo Grain Structures", *Journal of Materials Research*, 16 (2001) 413-416

[120] A. Budiman, P. Besser, C. Hau-Riege, A. Marathe, Y. Joo, N. Tamura, J. Patel, W. Nix, "Electromigration-Induced Plasticity: Texture Correlation and Implications for Reliability Assessment", *Journal of Electronic Materials*, 38 (2009) 379-391

[121] C. V. Thompson, in *Solid State Physics*, Academic Press, Burlington, United States, 55 (2001), Ch. VII

[122] J. Harper, K. Rodbell, "Microstructure Control in Semiconductor Metallization", *Journal of Vacuum Science and Technology B*, 15 (1997) 763-779

[123] S. Wong, C. Ryu, H. Lee, K. Kwon, "Barriers for Copper Interconnec-

tions”, Materials Research Society Proceedings, 514 (1998) 75-81

[124] J. E. Sanchez, P. R. Besser, D. P. Field, Microstructure of Damascene Processed Al-Cu Interconnects for Integrated Circuit Applications, AIP Conf. Proc., 418 (1998) 230-235

[125] R. A. Swalin, Thermodynamics in Solids, John Wiley and Sons, NY, 2nd edition (1976) 233

[126] Q. Jiang, M. Nowell, B. Foran, A. Frank, R. Havemann, V. Parihar, R. Augur, J. Luttmmer “Analysis of Copper Grains in Damascene Trenches after Rapid Thermal Processing or Furnace Anneals”, Journal of Electronic Materials, 31 (2002) 10-15

[127] V. Randle, in The Role of Coincident Site Lattice in Grain Boundary Engineering, The University Press, Cambridge, United Kingdom (1996) Ch. 3

[128] H. Gleiter, “The formation of Annealing Twins”, Acta Metallurgica, 17 (1969) 1421-1428

[129] C. Pande, M. Imam, B. Rath, “Study of Annealing Twins in FCC Metals and Alloys”, Metallurgical and Materials Transactions A, 21 (1990) 2891-2896

[130] C.-K. Hu, L. Gignac, B. Baker, E. Liniger, R. Yu, P. Flaitz, “Impact of Cu microstructure on electromigration reliability”, IEEE International Inter-

connect Technology Conference (2007) 93-95

[131] L. Cao, K. Ganesh, P. Ferreira, P. Ho, “Grain Structure Analysis in Copper Interconnects and its Implication on Electromigration Reliability for the 45 nm Technology Node” (submitted to IRPS 2012)

[132] A. Oates, M. Lin, “Electromigration Failure Distributions of Cu/Low-k Dual-Damascene Vias: Impact of the Critical Current Density and a New Reliability Extrapolation and Methodology”, IEEE TDMR, 9 (2009) 244-254

[133] K. Hattar, D. Follstaedt, J. Knapp, I. Robertson. “Defect Structures Created during Abnormal Grain Growth in Pulsed-Laser Deposited Nickel” *Acta Materialia*, 56 (2008) 794-801

[134] L. Brewer, D. M. Follstaedt, K. Hattar, J. Knapp, M. Rodriguez, I. Robertson, Competitive Abnormal Grain Growth between Allotropic Phases in Nanocrystalline Nickel”, *Advanced. Materials*, 22 (2010) 1161-1164

[135] P. Ryder, W. Pitsch, “The Uniqueness of Orientation Determination by Selected Area Diffraction”, *Philosophical Magazine* 15 (1967) 437-446

[136] Morawiec and Bouzy, “On the Reliability of Fully Automatic Indexing of Electron Diffraction Patterns Obtained in a Transmission Electron Microscope”, *Journal of Applied Crystallography*, 39 (2006) 101-103

Vita

Jai Ganesh Kameswaran entered the Materials Science and Engineering Program at The University of Texas at Austin in August of 2007. He received his Master of Science degree in Aug. 2009 and subsequently enrolled into the department's doctoral program. During the course of his PhD, he received the 2010 Microanalysis Society (MAS) Student Scholar Award for his research accomplishments. He was also the recipient of the MAS Distinguished Scholar Award, and the MSA Award sponsored by the Microscopy Society of America (MSA).

After graduation, Jai Ganesh Kameswaran will join Intel Corporation in Hillsboro, Oregon as a PTD Module and Integration Yield Engineer.

Permanent address: G-3 Rajiv Nagar Extension
Raipur, Chhattisgarh 492007, India

This dissertation was typeset with L^AT_EX[†] by the author.

[†]L^AT_EX is a document preparation system developed by Leslie Lamport as a special version of Donald Knuth's T_EX Program.